

Utah State University

DigitalCommons@USU

All Graduate Theses and Dissertations

Graduate Studies

5-2009

Rayleigh-Lidar Observations of Mesospheric Gravity Wave Activity above Logan, Utah

Durga N. Kafle
Utah State University

Follow this and additional works at: <https://digitalcommons.usu.edu/etd>



Part of the [Astrophysics and Astronomy Commons](#), and the [Atmospheric Sciences Commons](#)

Recommended Citation

Kafle, Durga N., "Rayleigh-Lidar Observations of Mesospheric Gravity Wave Activity above Logan, Utah" (2009). *All Graduate Theses and Dissertations*. 466.
<https://digitalcommons.usu.edu/etd/466>

This Dissertation is brought to you for free and open access by the Graduate Studies at DigitalCommons@USU. It has been accepted for inclusion in All Graduate Theses and Dissertations by an authorized administrator of DigitalCommons@USU. For more information, please contact digitalcommons@usu.edu.



RAYLEIGH-LIDAR OBSERVATIONS OF MESOSPHERIC GRAVITY WAVE
ACTIVITY ABOVE LOGAN, UTAH

by

Durga N. Kafle

A dissertation submitted in partial fulfillment
of the requirements for the degree
of

DOCTOR OF PHILOSOPHY

in

Physics

Approved:

Dr. Vincent B. Wickwar
Major Professor

Dr. Michael J. Taylor
Committee Member

Dr. Bela G. Fejer
Committee Member

Dr. Eric D. Held
Committee Member

Dr. Stephen E. Bialkowski
Committee Member

Dr. Byron R. Burnham
Dean of Graduate Studies

UTAH STATE UNIVERSITY
Logan, Utah

2009

Copyright © Durga N. Kafle 2009

All Rights Reserved

ABSTRACT

Rayleigh-Lidar Observations of Mesospheric Gravity Wave Activity Above Logan, Utah

by

Durga N. Kafle, Doctor of Philosophy

Utah State University, 2009

Major Professor: Dr. Vincent B. Wickwar
Department: Physics

A Rayleigh-scatter lidar operated from Utah State University (41.7°N, 111.8°W) for a period spanning 11 years — 1993 through 2004. Of the 900 nights observed, data on 150 extended to 90 km or above. They were the ones used in these studies related to atmospheric gravity waves (AGWs) between 45 and 90 km. This is the first study of AGWs with an extensive data set that spans the whole mesosphere. Using the temperature and temperature gradient profiles, we produced a climatology of the Brunt-Väisälä (buoyancy) angular frequency squared, N^2 (rad/s)². The minimum and maximum values of N^2 vary between 2.2×10^{-4} (rad/s)² and 9.0×10^{-4} (rad/s)². The corresponding buoyancy periods vary between 7.0 and 3.5 minutes. While for long averages the atmosphere above Logan, Utah, is convectively stable, all-night and hourly profiles showed periods of convective instability (i.e., $N^2 < 0$). The N^2 values were often significantly different from values derived from the NRL-MSISe00 model atmosphere because of the effects of inversion layers and semiannual variability in the lidar data.

Relative density fluctuation profiles with 3-km altitude resolution and 1-hour temporal resolution showed the presence of monochromatic gravity waves on almost every night throughout the mesosphere. The prevalent values of vertical wavelength and vertical phase velocity were 12–16 km and 0.5–0.6 m/s, respectively. However, the latter has the significant seasonal variation. Using these two observed parameters, buoyancy periods, and the AGW dispersion relation, we derived the ranges of horizontal wavelength, phase velocity, and source distance. The prevalent values were 550–950 km, 32–35 m/s, and 2500–3500 km, respectively.

The potential energy per unit mass E_p showed great night-to-night variability, up to a factor of 20, at all heights. E_p grew at approximately the adiabatic rate below 55–65 km and above 75–80 km. Step function decreases in E_p imply that the AGWs in between gave up considerable energy to the background atmosphere. In addition, E_p varies seasonally. Below 70 km, it has a semiannual variation with a maximum in winter and minima in the equinoxes. At the highest altitudes it has an annual variation with a maximum in winter and a minimum in summer.

ACKNOWLEDGMENTS

I would like to express my deepest gratitude to my major professor, Dr. Vincent B. Wickwar, for his guidance, enthusiastic support, motivation, and valued suggestions in completion of this dissertation. I would also like to thank the other members of my committee, Dr. Michael J. Taylor, Dr. Bela G. Fejer, Dr. Eric D. Held, and Dr. Stephen E. Bialkowski, for their encouragement and comments. Special thanks are due to Dr. Joshua P. Herron for providing the reduced temperature data. I am also thankful to all the faculty and staff of the Physics Department and the Center for Atmospheric and Space Sciences at Utah State University for their support. I am deeply grateful to my parents for beginning my education early and for supporting it endlessly throughout my life. Special thanks are deserved by my wife, Anju, for all she has done to help me and also by my daughters, Smreeti and Dipti, for taking me to a different arena than the scientific one and, hence, refreshing my mind. I would also like to give my special thanks to all my friends in the department.

This research was supported in part by Utah State University and a Howard L. Blood Fellowship in Physics.

Durga N. Kafle

CONTENTS

	Page
ABSTRACT	iii
ACKNOWLEDGMENTS	v
LIST OF TABLES	ix
LIST OF FIGURES	x
CHAPTER	
1. INTRODUCTION.....	1
2. RAYLEIGH-SCATTER LIDAR SYSTEM.....	7
1. Relative Density Calculation	10
2. Error Calculation for the Relative Density Measurements	13
3. Absolute Temperatures Calculation.....	14
4. Error Calculation for the Temperature Measurements	15
3. ATMOSPHERIC GRAVITY WAVES.....	17
1. Gravity Wave Sources	17
2. Observations	19
3. Gravity Wave Background Theory	20
3.1. Atmospheric Stability	20
3.2. Linear Gravity Wave Equations.....	21
4. Gravity Wave Propagation and Filtering	25
5. Gravity Wave Variability.....	27
6. Gravity Wave Potential Energy	28
7. Summary	30
4. CLIMATOLOGY OF MESOSPHERIC BRUNT-VÄISÄLÄ FREQUENCIES DERIVED FROM RAYLEIGH-SCATTER LIDAR OBSERVATIONS ABOVE LOGAN, UTAH	32
Abstract	32
1. Introduction.....	33
2. Measurements and Analysis Method	34
3. Results and Discussion	43
3.1. Climatology of the Brunt-Väisälä Frequency-Squared.....	43
3.2. Seasonal Variation of N^2	46

3.3.	Annual and Semiannual Variation of N^2	50
3.4.	Geophysical Variability	54
3.5.	N^2 Comparisons	56
4.	Summary and Conclusions	60
5.	CHARACTERISTICS OF MONOCHROMATIC GRAVITY WAVES IN THE MESOSPHERE OBSERVED BY RAYLEIGH LIDAR ABOVE LOGAN, UTAH	63
	Abstract	63
1.	Introduction	64
2.	Observations and the Derivation of Gravity Wave Parameters	66
2.1.	Observations	66
2.2.	Observed Gravity Wave Parameters	70
2.3.	Derived Gravity Wave Parameters	75
2.4.	Uncertainties in Wave Parameters	76
3.	Results of the Analysis	80
3.1.	Seasonal Variation of Gravity Wave Parameters	81
3.2.	Distribution of Gravity Wave Parameters	83
4.	Discussion	89
5.	Summary and Conclusions	95
6.	SEASONAL VARIATION OF MESOSPHERIC GRAVITY WAVE POTENTIAL ENERGY OBSERVED BY RAYLEIGH LIDAR ABOVE LOGAN, UT	99
	Abstract	99
1.	Introduction	100
2.	Measurements and Analysis Method	102
3.	Results of the Analysis	109
3.1.	Examples of the Parameters Derived	109
3.2.	Seasonal Variation in Wave Activity	116
4.	Discussion	120
5.	Summary and Conclusions	122
7.	DECREASES IN GRAVITY WAVE POTENTIAL ENERGY WITH ALTITUDE ABOVE LOGAN, UTAH	124
	Abstract	124
1.	Introduction	125
2.	Measurements and Method of Analysis	127
3.	Examples of the Observations	132
4.	Discussion	144
5.	Conclusions	146

8.	SUMMARY AND FUTURE WORK	149
1.	Summary and Conclusions	149
2.	Future Work	156
REFERENCES		160
APPENDICES		167
	APPENDIX A	168
	APPENDIX B	180
	APPENDIX C	194
CURRICULUM VITAE		196

LIST OF TABLES

Table		Page
1	Annual Mean Rayleigh Lidar N^2 Values for the Mesosphere Above Logan, UT	48
2	Examples of Uncertainties Calculated for N^2 at Various Altitudes	49
3	Examples of Uncertainties Calculated for Different Gravity Wave Parameters	80
4	Examples of Uncertainties Calculated for E_p at Various Altitudes	120

LIST OF FIGURES

Figure	Page
1 Temperature structure of the Earth's atmosphere	2
2 Schematic diagram of the ALO Rayleigh lidar	9
3 Relative density plotted as a function of altitude	12
4 Temperature profile averaged over the night for February 28, 1995	16
5 Examples of gravity waves	18
6 Examples of the growth of gravity waves with altitude	24
7 Gravity wave filtering by zonal winds	26
8 Gravity wave potential energy per unit mass versus altitude for July 23, 1996	29
9 Profiles related to finding N^2 for February 21, 1995	39
10 Profiles related to finding N^2 for July 23, 1996	40
11 Temperature gradient climatology above USU from 1993-2004 Rayleigh lidar observations	43
12 Monthly averaged N^2 values above USU from the 1993-2004 observations	44
13 N^2 climatology above USU from 1993-2004 Rayleigh lidar observations	46
14 Profiles showing seasonal variation of temperature, temperature gradient, and N^2	47
15 Variations of N^2 throughout the year at several altitudes	51
16 Profiles of mean N^2 , annual, and semi-annual amplitudes and phases	53
17 Growth of the geophysical variability of N^2 and T with altitude	55
18 Comparison of winter and summer N^2 profiles from several sources	58

19	N^2 climatology derived from NRL-MSISe00 model temperatures.....	59
20	Histogram of the observations made each month over the 11-year period from the 150 nights that reached 90 km.....	67
21	Profiles of relative density perturbations for (a) January 4, 1995 (b) August 17, 1995	71
22	Profiles of relative density perturbations for February 22, 1995	72
23	All-night average vertical wavenumber spectrum for: (a) January 04, 1995, (b) August 17, 1995	78
24	All-night average vertical wavenumber spectrum for: February 22, 1995	79
25	Seasonal variations in gravity wave parameters	82
26	Seasonal variation of buoyancy period	83
27	Histogram of gravity wave vertical wavelengths.....	84
28	Histograms of gravity wave vertical phase velocities for (a) winter and (b) summer.....	85
29	Histograms of deduced gravity wave periods for (a) winter and (b) summer.....	86
30	Histograms of deduced gravity wave parameters.	87
31	Histogram of gravity wave deduced horizontal distance to the source region for 45 km altitude above ALO.....	88
32	The two measured parameters: downward vertical phase velocity versus vertical wavelength.....	91
33	The portion of the AGW spectrum observed with the ALO Rayleigh lidar	92
34	Temperatures, relative densities, and derived parameters for 22 February 1995	110
35	Temperatures, relative densities, and derived parameters for 17 August 1995	111
36	Profiles of root-mean-square (rms) density perturbation and available potential energy per unit mass for a winter and summer day	115

37	Profiles of mean $E_p(z)$ for different seasons	117
38	Day-to-day and seasonal variation in E_p values at several altitudes	119
39	Behavior of several parameters on the night of February 19, 1995	134
40	Behavior of several parameters on the night of July 23, 1996.....	135
41	Behavior of several parameters on the night of July 24, 1996.....	137
42	Behavior of several parameters on the night of July 16, 1995.....	139
43	Behavior of several parameters on the night of June 22, 2000	140
44	Behavior of several parameters on the night of July 08, 1995.....	141
45	Behavior of several parameters on the night of April 07, 1995.....	143

CHAPTER 1

INTRODUCTION

The Earth's atmosphere surrounds and protects us by blocking out dangerous rays from the sun. At the surface, the atmosphere consists of 78% molecular nitrogen (N_2), 21% molecular oxygen (O_2), about 1% argon (Ar), and various other trace gases including water vapor (H_2O), ozone (O_3), and carbon dioxide (CO_2). The Earth's atmosphere is indispensable for all oxygen-breathing lifeforms, including humans. Because of turbulent mixing, the major constituents change little as one moves up through the atmosphere. Above about 100 km altitude, the mixing ratio of the heavy molecules decreases relative to light molecules and atoms due to molecular diffusion. In addition, very energetic short-wavelength solar radiation (UV and EUV) further changes the composition by dissociating molecules, particularly O_2 .

The temperature varies considerably from the ground up to about 100 km altitude, with a strong seasonal variation. Figure 1 gives representative temperature profiles for the atmosphere above Logan, Utah (41.74°N , 111.81°W) for summer (July 23, 1996) and winter (February 28, 1995) conditions. The profiles are from the NRL-MSISE00 empirical model of *Picone et al.* [2002]. Initially the atmosphere cools with altitude from the surface of the Earth to about 15 km at mid latitudes. This lowest region is called the troposphere. Then at altitudes above 15 km the atmosphere warms with altitude to about 50 km. This is the stratosphere. The atmosphere then cools with altitude up to about 90 km or 100 km. This is the mesosphere. Finally above the mesosphere the atmosphere warms with altitude. This is the thermosphere. The transitions between those regions where the temperatures reach local extremes are the tropopause, stratopause, and

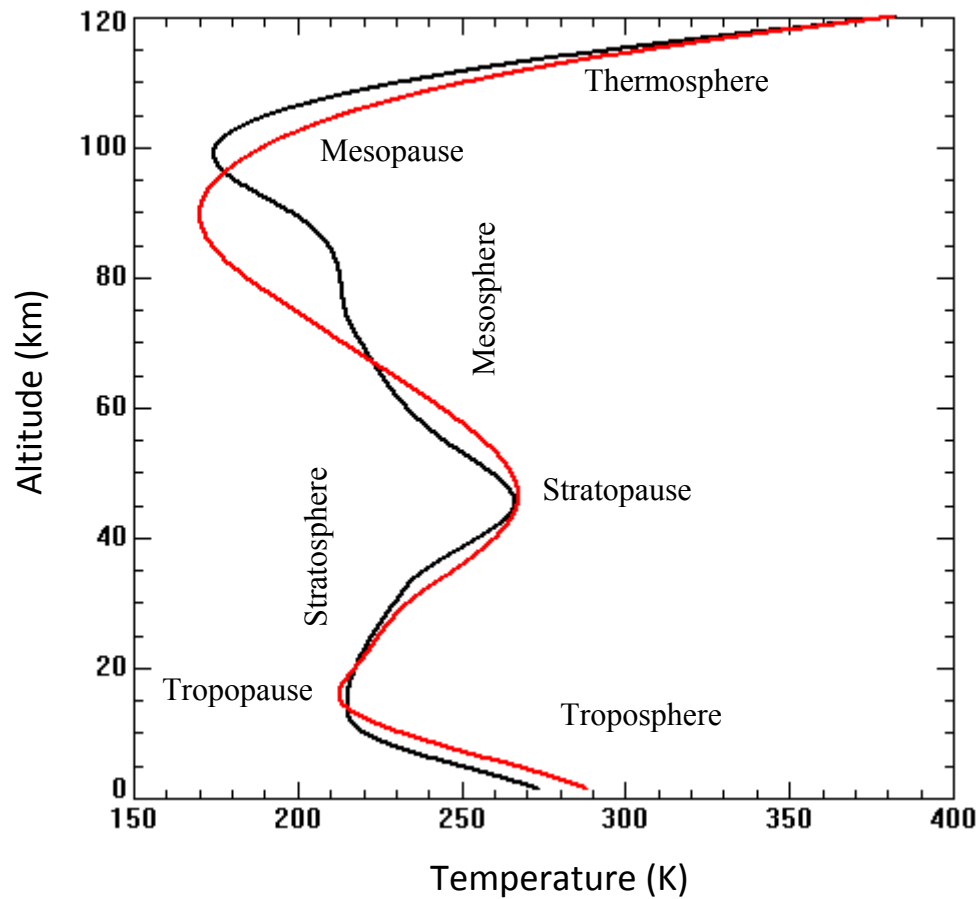


Figure 1. Temperature structure of the Earth's atmosphere. The red curve is for July 23, 1996, and the black curve is for February 28, 1995 [Picone *et al.*, 2002]. These profiles are representative of the summer and winter seasons over Logan, UT.

mesopause. The term lower atmosphere typically refers to the troposphere and the lower half of the stratosphere. Routine measurements of this portion of the atmosphere are carried out twice daily via weather balloons, radiosondes, that typically reach altitudes of 20 to 30 km. The stratosphere, mesosphere and lower thermosphere are collectively termed the middle atmosphere. Because of observational limitations, the middle atmosphere as a whole (especially the mesosphere) has been much less extensively studied than the regions immediately above and below.

The warming in the stratosphere is due to absorption of ultraviolet solar radiation (~250-300 nm) by ozone. The warming in the thermosphere is due to absorption of UV at low altitudes and EUV at higher altitudes [e.g., *Brasseur and Solomon*, 1984]. As we would expect the temperature at the surface of the Earth in the northern hemisphere is warmer in July than February (Figure 1). In fact, the summertime temperature profile is warmer than the wintertime profile up to about 65 km. The general temperature structure is well understood in terms of radiative equilibrium [e.g., *Brasseur and Solomon*, 1984; *Andrews et al.*, 1987]. However, in the mesosphere above that altitude, the atmosphere is not in radiative equilibrium, as clearly seen by its being significantly warmer in winter than in summer and vice versa.

The explanation of this departure from radiative equilibrium depends on dynamics, on winds, and waves. Turning to waves, because of different excitation mechanisms, atmospheric waves occur with different wavelengths and periods. They can be classified as planetary or Rossby waves, atmospheric tides with periods of 12 and 24 hours, gravity waves with periods from about 5 minutes up to several hours, and acoustic waves with periods of seconds and below. Concentrating on gravity waves, they result from a balance between inertia and restoring forces acting on fluid parcels displaced from their equilibrium positions. These wavelike motions appear as periodic oscillations in the wind field, temperature, pressure, and density of the air, and they propagate both vertically and horizontally. A detailed review of the role of waves in the middle atmosphere is given by *Holton and Alexander* [2000].

Today it is recognized that AGWs are an essential part of the dynamics of the atmosphere and play an important role in the mean circulation and temperature structure

of the middle atmosphere. They are also responsible, in part, for coupling between different atmospheric regions. The upward propagation of AGWs is mainly controlled by the environment through which they propagate. Gravity wave theory predicts that when a gravity wave propagates vertically into a region with a vertical gradient in the background wind field, three possible results may occur. First, if the vertical wavelength approaches zero, the wave has reached a critical level, where the horizontal phase velocity of the wave equals the mean background wind speed. The wave energy and momentum are then deposited into the background wind flow. This is called filtering. Second, if the vertical wavelength approaches infinity, the wave encounters a turning level (or reflecting level), which alters the propagation direction of the momentum fluxes. In passing through the reflecting level the wave is evanescent. If a second reflecting level is encountered, the wave can become trapped between these levels and is said to be ducted. Third, if the gravity wave is neither absorbed nor reflected, e.g., its horizontal phase speed is greater than the background wind speed, it can penetrate the wind gradient and propagate to higher altitudes. In so doing, it will grow in amplitude due to the decrease of the atmospheric density. It may obtain amplitudes large enough to exceed an instability threshold and become unstable. The possible instabilities include convective and dynamic instability. They cause the unstable waves to overturn or break [*Hodges, 1967; Lindzen, 1968*], producing turbulence and smaller scale gravity waves. More details about the filtering process, instabilities, and wave breaking are given in Chapter 3.

In this way, gravity waves deposit their energy and momentum into the background atmosphere [*Lindzen, 1981; Holton, 1982, 1983; McLandress, 1998; Fritts and Alexander, 2003; Huang et al., 2008*]. This also means that gravity waves observed

in the mesosphere and lower thermosphere (MLT) region contain information about both their sources and the wind fields between the source and region observed. The energy and momentum transfer from the gravity waves into the circulation of the MLT region is closely connected to gravity wave breaking and creation of turbulence. A comprehensive review about gravity wave breaking and creation of turbulence can be found in *Fritts* [1984] and *Fritts and Alexander* [2003]. All the processes mentioned above have profound impacts on the background atmosphere.

The main aim of this dissertation is to gain more understanding of mesospheric gravity waves by investigating their characteristics such as growth, propagation, and dissipation. The approach is to use extensive observations acquired with the Rayleigh-scatter lidar at the Atmospheric Lidar Observatory (ALO) in the Center for Atmospheric and Space Sciences (CASS) at Utah State University. This lidar technique is the only ground-based technique that can probe the whole mesosphere from 45 to 90 km. Observations occurred on 900 nights from 1993 through 2004. Of these profiles, the 150 that extend to 90 km or above are the ones used in this work.

This dissertation is organized with a discussion of the Rayleigh-scatter lidar in Chapter 2. A more extensive background into atmospheric gravity waves is presented in Chapter 3. The next four chapters are research papers that are to be submitted for publication. Chapter 4 details the determination of the Brunt-Väisälä frequency squared $N^2(z)$ properties and climatology using the absolute temperatures measured with the ALO Rayleigh-scatter lidar between 1993 and 2004. The results are useful for both a quantitative description of the atmosphere, an indication of where convective instabilities occur, and for applying the AGW dispersion relation to derive horizontal AGWs

parameters from the vertical observations. Chapter 5 identifies the presence of monochromatic AGWs in the entire mesosphere (45-90 km) and characterizes them. This includes determining the background density profiles and deriving the relative density perturbation profiles with respect to the background profiles. These latter profiles are examined to determine AGW parameters. The vertical wavelengths and vertical phase velocities are the observed parameters. The periods are determined from them and, in conjunction with the gravity wave dispersion relations, horizontal AGW parameters are derived. By combining the vertical and horizontal parameters, the approximate distance and the extent of possible gravity wave source regions are derived. Chapter 6 examines the variation of gravity wave potential energy per unit mass $E_p(z)$ as a function of altitude and time. This is done using relative density fluctuations. One aspect of examining these density fluctuations and E_p is to see how they grow with altitude and shift in magnitude under various situations. These situations include adjacent nights, seasons, altitude regions below and above mesospheric inversion layers, and the regions where values of N^2 reach local extremes. Chapter 7 examines the altitude variations of temperature, N^2 , density fluctuations, and E_p simultaneously to determine the conditions under which N^2 has minima and E_p has significant decreases. Chapter 8 provides an overall summary of results and conclusions. It also gives an indication of possible future work to extend what has been accomplished here. Appendix A provides the mathematical derivation of the AGW dispersion relation. Appendix B gives the IDL code used for this analysis. Appendix C lists the 150 nights used in this analysis.

CHAPTER 2

RAYLEIGH-SCATTER LIDAR SYSTEM

As we mentioned earlier, studies of the middle atmosphere (particularly the mesosphere) have been limited because of difficulties in making observations. Weather balloons, radiosondes, reach altitudes of between 20 and 30 km before they pop, thereby preventing measurements at higher altitudes. Radar systems can only make measurements up to at most 30 km or above 60 km and, more typically, 80 km. Airglow measurements are confined to several layers above 80 km. Resonance lidar observations are between 83 and 102 km. Rockets provide intermittent measurements during campaign periods, but are expensive to build and launch. Although satellite remote sensing measurements provide global coverage of variability associated with atmospheric gravity waves, they are not good for time evolution over a given location and they orbit at too high an altitude to make *in situ* measurements. Thus, there is a region from about 30 km to 80 km where relatively few observations have been made. However, Rayleigh-scatter lidar is capable of making observations of relative density and absolute temperature with good temporal and spatial resolution over the entire mesosphere.

A lidar type approach, involving a searchlight, was first proposed in 1930 by Synge [Synge, 1930]. Johnson *et al.* [1939] carried out the first Rayleigh-type observations that reached the stratosphere by using a searchlight beam. They proposed that the method could be extended to enable measurements up to heights of 70 to 90 km. In 1951, Rayleigh-type observations were carried out using a searchlight to measure the stratospheric density distribution [Elterman, 1951]. The first Rayleigh lidar observations to determine mesospheric temperatures were carried out using a ruby laser in 1970 [Kent

and Wright, 1970]. Systematic Rayleigh observations using a Nd:YAG laser at 532 nm were started by Chanin and co-workers in 1978 [*Hauchecorne and Chanin, 1980*]. ALO adopted the approach pioneered by the French, starting regular observations in 1993 [*Wickwar et al., 2001*].

Today, Rayleigh-scatter lidars are becoming widely used in studies of the middle atmosphere, particularly in the altitude range of 30 to 90 km. With the capability of resolving temporal and spatial atmospheric fluctuations continuously within this altitude range, Rayleigh lidar has become increasingly useful in the study of atmospheric dynamics, allowing observation of geophysical phenomena such as atmospheric gravity waves [*Gardner et al., 1989; Mitchell et al., 1991; Wilson et al., 1991b; Meriwether et al., 1994; Whiteway et al., 1995*], tidal variations [*Gille et al., 1991*], stratospheric warmings and planetary waves [*Hauchecorne and Chanin, 1982, 1983*], mesospheric inversions [*Hauchecorne et al., 1987; Whiteway et al., 1995*]. Rayleigh-scatter lidar systems typically employ powerful Nd:YAG lasers that are technologically mature and can be maintained and operated in a routine fashion [e.g., *Hecht, 1992*]. The receiver does not require wavelength tuning. While daytime measurements require one or two Fabry-Perot interferometers to filter out scattered sunlight, nighttime measurements are relatively straightforward, depending on a good interference filter. The only physical assumption concerning the data reduction is that the atmosphere is in hydrostatic equilibrium. These days, Rayleigh-scatter lidar measurements remain the only viable ground-based technique for routinely measuring stratospheric and mesospheric density and temperature profiles.

The Rayleigh-scatter lidar at the Atmospheric Lidar Observatory (ALO) on the Utah State University (USU) campus (41.7°N, 111.8°W, 1.47 km altitude) has been in operation since 1993. Figure 2 presents a schematic diagram of this lidar. It primarily consists of a pulsed Nd:YAG laser generating 18 or 24 watts at 532 nm, a 44-cm diameter Newtonian telescope, a mechanical chopper, a gated photomultiplier tube, and a multi-channel scaler to accumulate the data. For more information about the system, see *Beissner [1997]; Wickwar et al. [2001]; Herron [2004, 2007]; Herron and Wickwar [2009a]*.

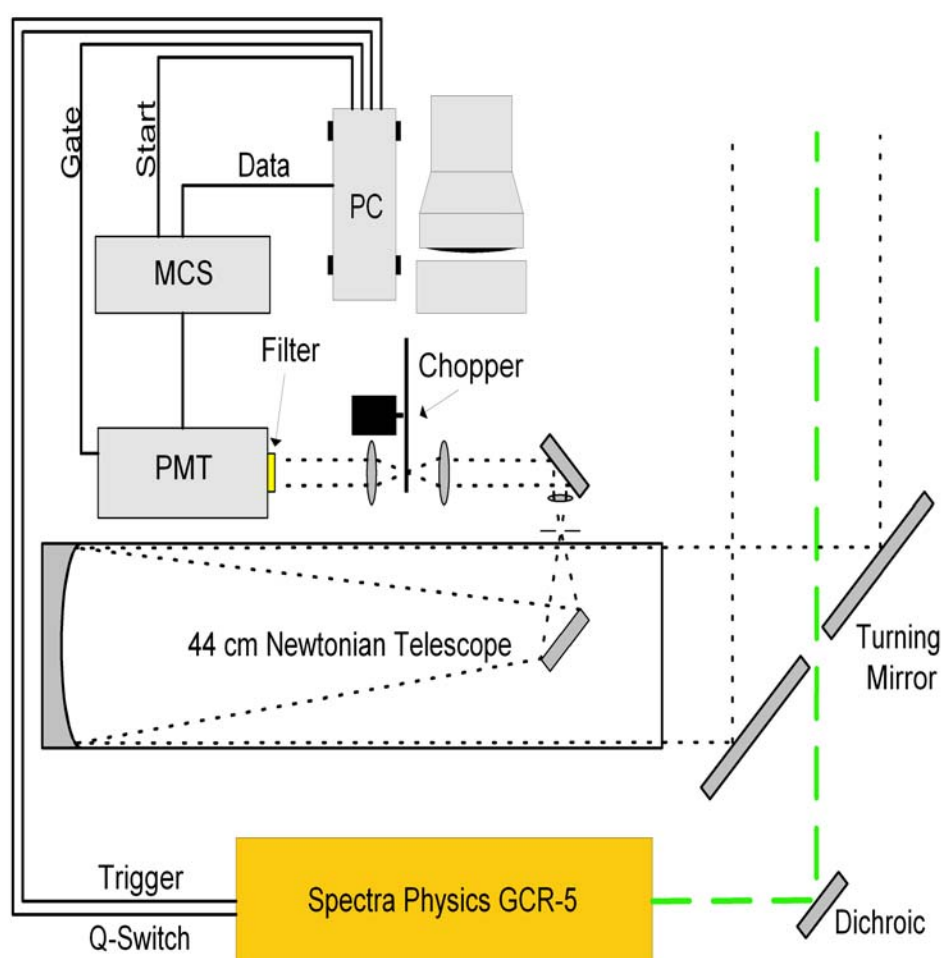


Figure 2. Schematic diagram of the ALO Rayleigh lidar [Adapted from *Herron, 2004*].

1. Relative Density Calculation

The basis for Rayleigh lidar is Rayleigh scatter from atmospheric molecules. In this elastic scattering, the incident radiation induces an electric dipole in the molecule. It oscillates at the same wavelength as the incident radiation and produces a photon at the same wavelength. The Rayleigh scattering cross section is strongly dependent on the wavelength of the light that is scattered. For the standard atmospheric constituents up to an altitude of 110 km, the Rayleigh backscatter cross section is given as [Measures, 1992]

$$\sigma_{\pi}^R(\lambda) = 5.45 \left[\frac{550}{\lambda(nm)} \right]^4 \times 10^{-32} \text{ m}^2 \text{ sr}^{-1}. \quad (2.1.1)$$

Because the backscatter cross section varies as λ^{-4} , a significant gain in the return signal results if the wavelength of the laser is shortened. In our case, the fundamental at 1064 nm is frequency doubled to produce 532 nm. This process is ~50% efficient, giving a net gain of a factor of 8. The lidar data consists of photon counts from backscattered laser light. They are acquired, in our case, in 37.5-m height intervals and over 2-minute time intervals from the ground to well above 100 km. The data of interest start at 40 km. According to the lidar equation the number of backscattered photons $N(z)$ scattered from a laser pulse of N_0 photons will be proportional to the product of the square of the atmospheric transmission $T(z)$ from the lidar to the scattering range, the molecule cross section for Rayleigh backscatter σ_{π}^R , the efficiency of the receiver system Q , and the range-squared correction as follows:

$$N(z) = \frac{N_0 A Q T^2(z)}{h^2} \left[n(z) \sigma_{\pi}^R \right], \quad (2.1.2)$$

where h is the range from the lidar, $n(z)$ is atmospheric number density at z , and A is telescope area. Range from the lidar, $h = (z - 1.47)$ km and z is the altitude from sea level.

At each altitude z the observed photon counts $N(z)$ are the sum of the background signal $N_B(z)$ from the detector, moon and star light, and scattered city lights, and the signal of interest $N_S(z)$ from the backscattered laser pulse, i.e., $N(z) = N_S(z) + N_B(z)$. The background signal, which is assumed to be constant with altitude, has to be determined at an altitude above the signal region, i.e., above 120 km, and subtracted from the total. From the lidar equation (2.1.2), this backscattered signal $N_S(z)$, multiplied by the square of the range h^2 from the laser, is proportional to the number density $n(z)$ of N_2 and O_2 molecules in the range gate. Because the mean-molecular mass can be assumed constant in the mesosphere, the backscattered signal is also proportional to the mass density of the atmosphere $\rho(z)$. If we assume that the atmospheric transmission at 532 nm is unity in the mesosphere (i.e., the laser pulse energy remains constant above a certain altitude), then the ratio of the photon count signal $N_S(z)$ at two altitudes (z_1 and z_2) is proportional to the ratio of the density $\rho(z)$ at these altitudes scaled by the range squared,

$$\frac{N_S(z_2)}{N_S(z_1)} = \frac{\rho(z_2)}{h_2^2} \bigg/ \frac{\rho(z_1)}{h_1^2} . \quad (2.1.3)$$

Thus we can derive a relative density profile $\rho(z, z_0)$ from the backscattered lidar signal,

$$\rho(z, z_0) = \frac{\rho(z)}{\rho(z_0)} = \frac{N_s(z)}{N_s(z_0)} \frac{h^2}{h_0^2}, \quad (2.1.4)$$

$$\rho(z, z_0) = \frac{(N(z) - N_B)}{(N(z_0) - N_B)} \frac{h^2}{h_0^2}. \quad (2.1.5)$$

We normalize the density to 1 at $z_0 = 45$ km, i.e. $\rho(z_0, z_0) = 1$. Unfortunately, this removes effects from gravity waves, tides, and planetary waves at 45 km, but it compensates for variations in atmospheric transmission and laser power.

The relative density profile for the night of February 28, 1995 is shown in Figure 3. The relative density profile from the NRL-MSISE00 model is also plotted in Figure 3 for comparison for the same night. While not identical, the two curves are nearly straight lines and are nearly the same. Both show the density decreasing by $\sim 10^3$ from 45 to 90

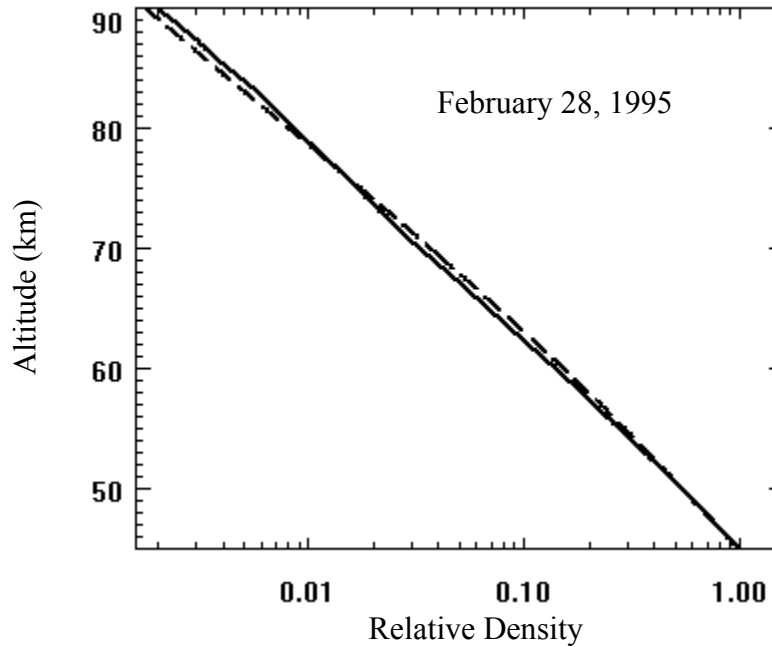


Figure 3. Relative density plotted as a function of altitude. The relative density profiles are normalized to 1 at 45 km. The solid curve is the relative density derived from the ALO-Rayleigh lidar measurement for the night of February 28, 1995. The dashed curve is from the NRLMSISE-00 model for the same night.

km. This corresponds to an e-folding distance or density scale height of approximately 7 km.

2. Error Calculation for the Relative Density Measurements

To simplify the presentation in this section, we can rewrite equation (2.1.5) for the relative density in the form

$$X = \frac{(S - B)}{(L - B)} \times C, \quad (2.1.6)$$

where $X = \rho(z, z_0)$, $S = N(z)$, $L = N(z_0)$, and $B = N_B$ are variables and $C = h^2/h_0^2$ is a constant. The quantities S , L and B are independent, and following *Bevington and Robinson* [1969] the variance of X is related to the other variables as follows,

$$\sigma_X^2 = \left(\frac{\partial X}{\partial S} \right)^2 \sigma_S^2 + \left(\frac{\partial X}{\partial B} \right)^2 \sigma_B^2 + \left(\frac{\partial X}{\partial L} \right)^2 \sigma_L^2. \quad (2.1.7)$$

Differentiating equation (2.1.6),

$$\frac{\partial X}{\partial S} = \frac{C}{L - B} = \frac{(S - B)}{S - B} \frac{C}{L - B} = \frac{X}{S - B}, \quad (2.1.8)$$

$$\begin{aligned} \frac{\partial X}{\partial B} &= -\frac{C}{L - B} + (S - B) \frac{1}{(L - B)^2} \\ &= -\frac{C}{L - B} + \frac{C(S - B)}{(L - B)^2} = -\frac{X}{S - B} + \frac{X}{(L - B)}, \end{aligned} \quad (2.1.9)$$

$$\frac{\partial X}{\partial L} = C(S - B) \left(-\frac{1}{(L - B)^2} \right) = -\frac{C(S - B)}{(L - B)^2} = -\frac{X}{L - B}. \quad (2.1.10)$$

Hence the variance σ_X^2 in X is given by

$$\sigma_X^2 = \left(\frac{X}{S-B}\right)^2 \sigma_S^2 + \left(\frac{X}{L-B}\right)^2 \sigma_L^2 + \left\{ \left(\frac{X}{S-B}\right)^2 + \left(\frac{X}{L-B}\right)^2 - \frac{2X^2}{(S-B)(L-B)} \right\} \sigma_B^2. \quad (2.1.11)$$

Because the return signal follows a Poisson distribution, the return signal can be substituted in place of the variance: $\sigma_S^2 = S = N(z)$, $\sigma_L^2 = L = N(z_0)$ and $\sigma_B^2 = B = N_B/K$, where K = the number of range bins over which the average N_B is calculated. Combining these, the variance of the relative density σ_ρ^2 is given by

$$\sigma_\rho^2(z) = \left(\frac{N(z)}{N_S^2(z)} + \frac{N(z_0)}{N_S^2(z_0)} + \left\{ \frac{1}{N_S^2(z)} + \frac{1}{N_S^2(z_0)} - \frac{2}{N_S(z)N_S(z_0)} \right\} \frac{N_B}{K} \right) \rho^2(z, z_0). \quad (2.1.12)$$

3. Absolute Temperatures Calculation

Under the assumption that the atmosphere is comprised of an ideal gas in hydrostatic equilibrium, it is possible to derive the temperature from the relative density [Hauchecorne and Chanin, 1980; Chanin, 1984; Chanin and Hauchecorne, 1984]. Hourly averages or all-night averages of the relative densities are used in calculating the temperature profiles. Given the long integration times, the assumption that the atmosphere is in hydrostatic equilibrium is valid. The details, as applied to this lidar, are reviewed by Beissner [1997], Wickwar *et al.* [2001], and Herron [2004, 2007]. The temperatures $T(z)$ are the sum of two terms:

$$T(z) = T(z_{\max}) \frac{n(z_{\max})}{n(z)} + \frac{1}{kn(z)} \int_z^{z_{\max}} m(z')g(z')n(z')dz'. \quad (2.3.1)$$

The integration runs from the altitude of interest z to the maximum altitude z_{\max} at which $T(z_{\max})$ is the supplied initial value. Where k is Boltzman's constant, $g(z)$ is the gravitational acceleration, and $m(z)$ is the mean molecular mass, which we are assuming

to be constant. The temperature algorithm is based on an initial temperature at the chosen z_{\max} . We choose z_{\max} to be the altitude at which the signal is 16 standard deviations. The initial temperature for this altitude must be provided from some source outside of the Rayleigh lidar. This temperature may be from a model or other observations. Currently if the altitude is above 83 km, the starting temperatures are taken from the temperature climatology from the sodium lidar at Colorado State University (CSU) [She *et al.*, 2000] and interpolated for the correct date and altitude. However, if the starting altitude is below 83 km the starting temperature is based both on the MSIS90 [Hedin, 1991] model and the sodium climatology. The offset between the climatology and the model at 83 km is used to offset the starting temperatures at lower altitudes from the model.

4. Error Calculation for the Temperature Measurements

The temperature uncertainty arising from the measurement uncertainty is calculated using the same propagation of error technique used to determine the error in the relative density profile. The final result for the temperature uncertainty [Gardner, 1989; Herron, 2004, 2007]

$$\sigma_{T_z}^2 = T_z^2 \left(\frac{\sigma_{n_z}}{n_z} \right)^2 + \left[\sigma_{T_{\max}}^2 + T_{\max}^2 \left(\frac{\sigma_{n_{\max}}}{n_{\max}} \right)^2 \right] e^{\frac{-2(z_{\max} - z)}{H}}, \quad (2.4.1)$$

where T_z and n_z are the temperature and number density at z , T_{\max} and n_{\max} are the temperature and relative number density at the top altitude z_{\max} , and H is the atmospheric scale height, which is assumed to be constant at 7 km. The first term in the equation is derived from the ideal gas law. The second term is based on the uncertainty of the initial

temperature, and decreases dramatically with height. Typically, the uncertainty of the initial temperature is unknown and is assumed to be zero as it has a limited range of influence because the exponential term causes it to decrease rapidly with decreasing altitude. Likewise, the uncertainty from the third term also decreases rapidly with decreasing altitude. Figure 4 is an example of the all-night averaged temperature profile and the temperature uncertainties for the night of February 28, 1995. The observations were carried out over 12 hours; the maximum altitude was set to 95 km.

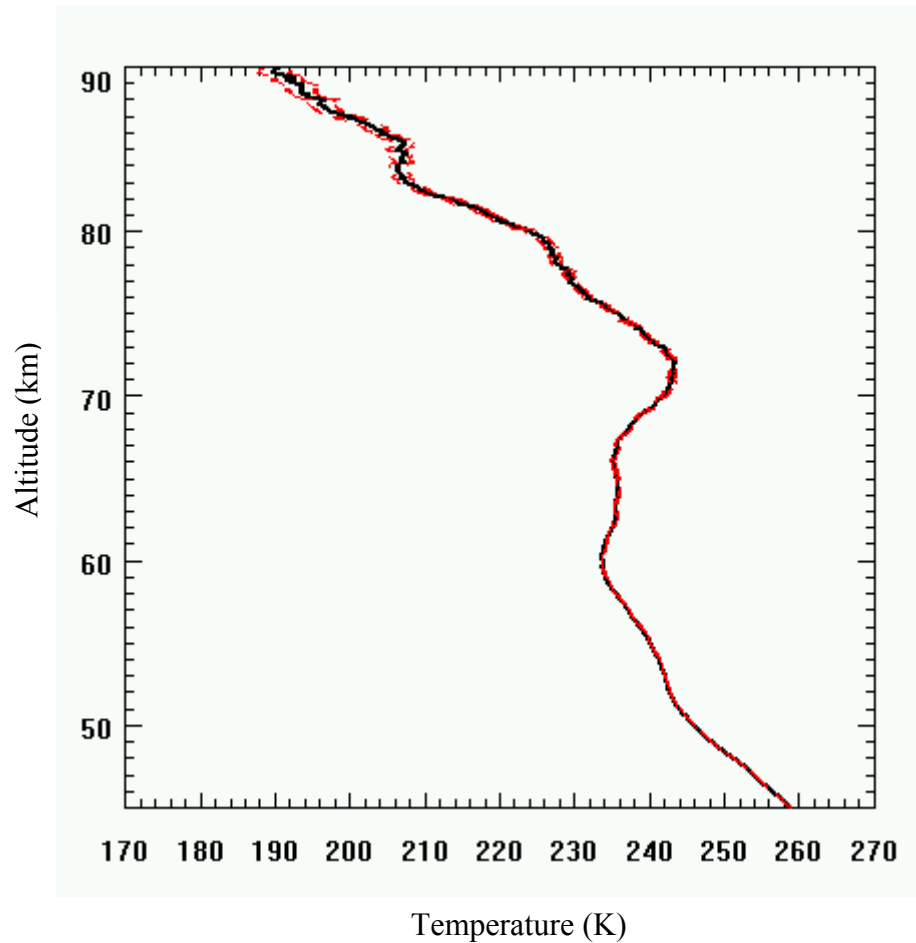


Figure 4. Temperature profile averaged over the night for February 28, 1995. The red dashed curves give the measurement uncertainties based on the Poisson distribution for the observations.

CHAPTER 3

ATMOSPHERIC GRAVITY WAVES

Based on gravity-wave theory [*Hines*, 1960], relative density and temperature perturbations in the middle atmosphere have been extensively examined. A gravity wave (GW) is an oscillation caused by the displacement of an air parcel which is restored to its initial position by gravity. The lifting force is buoyancy, while the restoring force is gravity, so these waves are sometimes known synonymously as buoyancy waves. Although gravity does play an important role in the existence of these waves, it is not the source of their creation. However, the convention of referring to these waves as gravity waves is firmly established, and we will adhere to it. There is a high-frequency limit above which the atmosphere cannot sustain these gravity waves, the Brunt-Väsälä or buoyancy frequency. These waves are found everywhere in the atmosphere. They can have vertical wavelengths that range from less than 1 km to more than 20 km and horizontal wavelengths that range from less than 10 km to more than 2000 km. They can have periods that range from ~5 minutes to almost 18 hours at our latitude. Clear air turbulence and lee waves are well-known examples of atmospheric gravity waves. Pictorial views of gravity waves seen in noctilucent clouds and in tropospheric clouds are shown in Figures 5a and 5b, respectively.

1. Gravity Wave Sources

There are several different gravity wave sources. Most of them occur in the lower levels of the atmosphere (troposphere and stratosphere). Two of the most important sources (due to both their frequent occurrence and the strength of the resulting waves) are

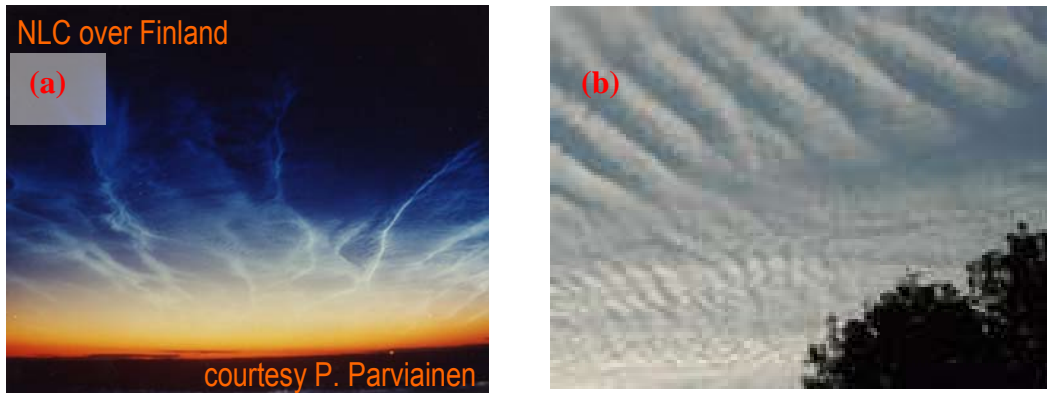


Figure 5. Examples of gravity waves. (a) Noctilucent clouds in the mesosphere [Courtesy, P. Parviainen]. (b) Clouds in the troposphere [Courtesy R.B. Thompson].

orography (wind over mountains) and storm convection. Some other sources are jet streams, interactions between other waves (such as atmospheric tides), collisions of pressure fronts, spontaneous adjustment resulting from geostrophic imbalance, volcanic eruptions, and earthquakes. In the upper atmosphere, gravity waves can also be generated by variations in the joule and particle heating in the auroral region, and by the breaking of upward propagating tides and gravity waves. Different sources tend to dominate at different latitudes. Low-latitude gravity waves often come from storm convection because of the large amount of storm activity in the tropics. Mid-latitude gravity waves are mostly from tropospheric jets mainly in summer, and orographic sources, particularly in the northern hemisphere, which has more landmass and therefore more mountains than the Southern hemisphere. The major exception for orography in the Southern hemisphere arises from the Andes mountains.

2. Observations

A wide variety of techniques have been used to study atmospheric gravity waves. They can be split into three major categories: ground-based remote sensing, satellite-based remote sensing and *in situ* measurements. The ground-based remote sensing include radars, lidars, and airglow measurements. The *in situ* measurements include balloons, aircraft and rockets. A significant amount of information about atmosphere gravity waves already has been obtained using these techniques. Radars can provide a detailed description of the wind field as a function of height and time, albeit with a hole between 30 and 80 km. They can also produce spectral descriptions of the wind field fluctuations as a function of frequency. Rayleigh lidars provide information on temperature and density fluctuations throughout the middle atmosphere and resonance lidars provide information on temperature and velocity fluctuations from 83-102 km. Rocket data provide almost instantaneous profiles of density, temperature and wind from which gravity wave properties can be inferred. Balloons (radiosondes) provide these same parameters as the balloon rises. In another distinction ground-based remote sensing techniques give measurements at only one location but with excellent altitude and time resolution. In contrast, satellite-based remote sensing gives valuable global information on atmospheric gravity waves but typically they have rather a narrow range of observable vertical and horizontal wavelengths and cannot observe the time evolution above one location.

3. Gravity Wave Background Theory

3.1. Atmospheric Stability

A qualitative notion of the nature of gravity waves can be obtained by considering the dynamics of a fluid parcel under the assumption that the motion of the parcel does not effect the environment, i.e., that it does not give or receive energy from its surroundings. The atmosphere is almost always stably stratified (i.e., atmospheric density increases with depth) and it is reasonable to assume that it always contains gravity waves. Stability of the fluid parcel determines the layer's ability to support and propagate these waves. The simplest approach to the concept of atmospheric stability is the parcel method. The environmental lapse rate, Γ , determined from an observed atmospheric temperature profile, is given by $\Gamma = -dT/dz$. For a parcel of dry air, the dry adiabatic lapse rate Γ_a is the largest temperature change the atmosphere can sustain and remain stable to convection. In general, $\Gamma_a = g(z)/c_p$, where c_p is the specific heat capacity of air at constant pressure. For the Earth, $\Gamma_a = 9.8$ K/km, at sea level. In terms of lapse rates, the atmosphere will be stable when $\Gamma < \Gamma_a$ while it will be unstable when $\Gamma > \Gamma_a$. If $\Gamma = \Gamma_a$, the atmosphere would be in equilibrium. Gravity waves exist only in a stable atmosphere.

A gravity wave is created when any one of the source mechanisms mentioned above (or possibly some other mechanisms) forces a parcel of air upward into a stable region (as defined above). This is where gravity comes into play and pulls the parcel back down. Before the parcel sinks back down, however, it forces more air upwards, and that air parcel bumps into even more air and so on until a vertically propagating component of this wave is formed. The wave will have a maximum frequency equal to the Brunt-Väsälä frequency (N). The square of its value is given by

$$N^2(z) = \frac{g(z)}{T(z)} \left[\frac{\partial T(z)}{\partial z} + \frac{g(z)}{c_p} \right] (\text{rad/s})^2, \quad (3.1.1)$$

where $g(z)$ is gravitational acceleration, $T(z)$ is the temperature and z is altitude.

3.2. Linear Gravity Wave Equations

The basis for all descriptions of the dynamics of the atmosphere is the Navier-Stokes equation describing the change in the flow velocity, \bar{u} , of a small volume of fluid.

The upward acceleration arising from various forces is

$$\frac{d\bar{u}}{dt} = -\frac{1}{\rho} \nabla p + \bar{g} - 2\bar{\Omega} \times \bar{u} + \bar{f} + \bar{\xi}, \quad (3.1.2)$$

[Holton, 1992], where $-\frac{1}{\rho} \cdot \nabla p$ is the pressure gradient force, p is pressure, ρ is density,

\bar{g} is the gravitational force, which acts only in the vertical direction, $-2\bar{\Omega} \times \bar{u}$ is the coriolis force which plays a role for motions with a very large horizontal scale and we neglect it here, $\bar{\Omega}$ is the Earth's angular velocity, \bar{f} and $\bar{\xi}$ are friction and drag forces, respectively, and both are neglected here because they are very small in most circumstances compared to the remaining terms. The continuity, momentum, and energy equations under these assumptions for a single-component neutral gas then become

$$\frac{d\bar{u}}{dt} = -\frac{1}{\rho} \nabla p + \bar{g}, \quad (3.1.3)$$

$$\frac{\partial \rho}{\partial t} + \nabla \cdot (\rho \bar{u}) = 0, \quad (3.1.4)$$

$$\left(\frac{\partial}{\partial t} + \bar{u} \cdot \nabla \right) p + \gamma p (\nabla \cdot \bar{u}) = 0, \quad (3.1.5)$$

where γ is the ratio of specific heats c_p/c_v and c_v is the specific heat at constant volume.

Under the assumption of horizontal stratification, the pressure and density vary in the atmosphere only in the vertical direction

$$\left. \begin{aligned} p(z) &= p(z_0) e^{\frac{z-z_0}{H_p}} = p(z_0) e^{-\Delta z/H_p} \\ \rho(z) &= \rho(z_0) e^{\frac{z-z_0}{H_\rho}} = \rho(z_0) e^{-\Delta z/H_\rho} \end{aligned} \right\} \quad (3.1.6)$$

where z_0 is the altitude of the reference level and H_p and H_ρ are the pressure and density scale heights, respectively. In the lower and middle atmosphere, these scale heights have a value of about 7 km.

Atmospheric perturbations can be taken into account by adding a small value to the background values of horizontal velocity u_0 , density ρ_0 , and pressure p_0 i.e.,

$$\left. \begin{aligned} p &= p_0 + p_1 \\ \rho &= \rho_0 + \rho_1 \\ \vec{u} &= \vec{u}_1 \text{ and } \vec{u}_1 = u_{1x}\hat{x} + u_{1z}\hat{z} \end{aligned} \right\} \quad (3.1.7)$$

where p_1 , ρ_1 , and u_1 are the perturbed amplitudes of the gravity waves. u_{1x} and u_{1z} are the horizontal and vertical components of the perturbation velocity, \vec{u}_1 . \hat{x} and \hat{z} are unit vectors along horizontal and vertical directions, respectively. An approximation is made that the perturbations are small compared to the mean parameters, which allows for linearization of the equations (3.1.3), (3.1.4), and (3.1.5) to simplify solving them. The linearized versions of these equations give four equations which are solved by assuming plane wave solutions of the form

$$\frac{p_1}{p_0} \propto \frac{\rho_1}{\rho_0} \propto \bar{u}_1 \propto e^{i(\omega t - k_x x - k_z z)}, \quad (3.1.8)$$

where k_x and k_z are the horizontal and vertical wave numbers, respectively. Thus this solution clearly includes both horizontal and vertical propagation. In addition to the vertical propagation, the gravity waves can grow in the vertical direction. Accordingly, we allow k_z to have both real (k_{zr}) and imaginary (k_{zi}) components, i.e., $k_z = k_{zr} + ik_{zi}$.

The wave equation 3.1.8 now becomes

$$\frac{p_1}{p_0} \propto \frac{\rho_1}{\rho_0} \propto \bar{u}_1 \propto e^{(k_{zi}z)} e^{i(k_x x + k_{zr} z - \omega t)}. \quad (3.1.9)$$

Introducing this wave equation 3.1.9 into the above mentioned linearized equations leads to the gravity wave dispersion equation

$$\omega^4 - \omega^2 c_0^2 (k_x^2 + k_{zr}^2 - k_{zi}^2) + \gamma g k_{zi} \omega^2 + (\gamma - 1) g^2 k_x^2 + i \omega^2 k_{zr} (\gamma g - 2 c_0^2 k_{zi}) = 0, \quad (3.1.10)$$

the derivation of which is given in Appendix A. Solving for the imaginary part gives

$$k_{zi} = \frac{\gamma g}{2 c_0^2} = \frac{1}{2 H_\rho}, \text{ where } c_0 = \sqrt{g H_\rho \gamma} \text{ is the sound speed. The complete solution for the}$$

gravity wave now becomes

$$\frac{p_1}{p_0} \propto \frac{\rho_1}{\rho_0} \propto \bar{u}_1 \propto e^{\frac{z}{2 H_\rho}} e^{i(k_x x + k_{zr} z - \omega t)}, \quad (3.1.11)$$

where \bar{u}_1 has horizontal (u_{1x}) and vertical (u_{1z}) components.

As can be seen from equation (3.1.11), the wave propagates in both vertical and horizontal directions. Its perturbation amplitudes also grows exponentially with altitude according to $e^{\frac{z}{2 H_\rho}}$. The waves that propagate in this manner are called internal gravity waves. These waves have the property that the amplitude of the vertical wave

perturbation energy, $\frac{1}{2}\rho_0|u_{1z}^2|$, is constant because $\rho_0 \propto e^{-\Delta z/H_p}$, $u_{1z} \propto e^{\Delta z/2H_p}$ and

$H_p \approx H_p$. Using equation (3.1.11) and dividing by ρ_0 , the amplitude of the wave

perturbation energy per unit mass E becomes

$$E = \frac{1}{2}|u_{1z}^2| \propto \frac{1}{2}e^{\frac{\Delta z}{H_p}}, \quad (3.1.12)$$

which grows with altitude at the rate $e^{\Delta z/H_p}$.

Figure 6a is a cartoon showing a fully developed atmospheric gravity wave [Hines, 1960], i.e., the wave is growing without exchanging the energy with surrounding atmosphere. A similar wave pattern is observed for density perturbations measured with the ALO Rayleigh lidar. An example, from August 17, 1995, is shown in Figure 6b. (A detailed explanation of how to calculate the density perturbation is given in a later

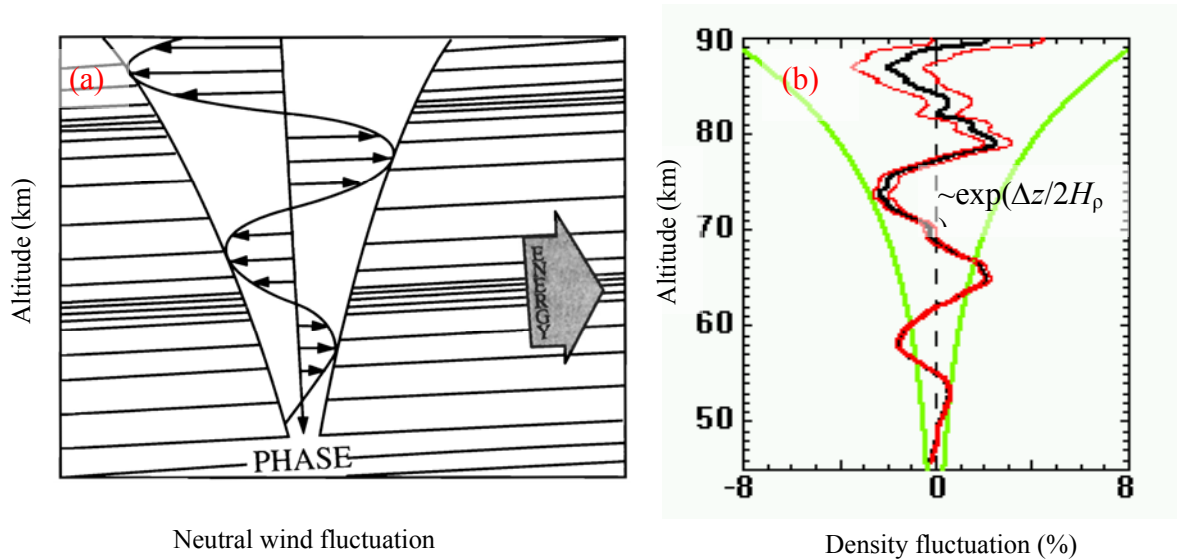


Figure 6. Examples of the growth of gravity waves with altitude. (a) A cartoon depicting fully developed atmospheric gravity wave [Hines, 1960] (b) A similar result obtained using the ALO Rayleigh lidar on August 17, 1995. The exponential curves grow according to $\exp(\Delta z/2H_p)$. In the cartoon, the neutral wind fluctuations grow at this rate. In the observations, the density fluctuations often grow at a slower rate above 70-75 km.

section.) The green curves in Figure 6b are the adiabatic growth curves given by equation (3.1.11) assuming that the waves grow with altitude without exchanging energy with the surrounding atmosphere. The red curves are the measurement uncertainties. Above 70 to 75 km, the observed values are significantly smaller than the adiabatic values. This implies that the wave is giving up energy to the surrounding atmosphere as it propagates to higher altitudes. With Rayleigh lidar, we have direct measurement of gravity wave vertical wavelengths and vertical phase velocities. Using these vertical parameters in conjunction with gravity wave dispersion relations, we derive the horizontal gravity wave parameters such as horizontal wavelength, horizontal phase velocity and horizontal distance to the source region. The derivations are given in Chapter 5 and Appendix A.

4. Gravity Wave Propagation and Filtering

When gravity waves originate in the troposphere their horizontal phase speeds will typically range from zero (orographic waves) to tropospheric flow speeds (e.g., jet stream velocities). As just derived, they also propagate upwards and grow in amplitude as they do so, thereby providing a linkage between low and higher altitudes. The mean flow speeds and directions, which vary with season, effectively determine which gravity waves will reach the mesosphere and their breaking levels. When a wave reaches an altitude where its horizontal phase velocity c is equal to the background mean flow or wind u (i.e., $c = u$), it is absorbed [Lindzen, 1981] into the mean flow and does not propagate any further. This process is called filtering. Figure 7 is a cartoon showing how the filtering effect influences mid-latitude wave propagation in summer and winter. The jet stream (located at the top of the troposphere, about 12 to 15 km above the Earth's

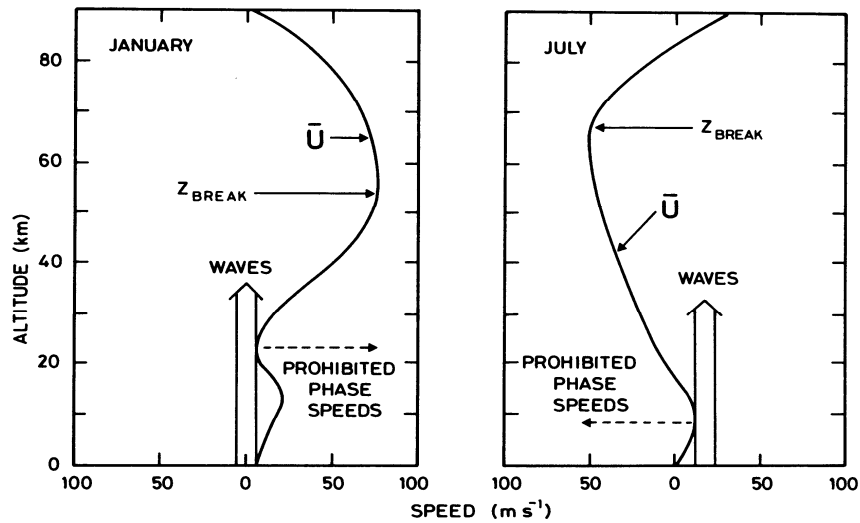


Figure 7. Gravity wave filtering by zonal winds [Lindzen, 1981]. In winter waves with zero and westward phase speeds can reach the mesosphere. In summer waves are filtered by both the eastward tropospheric jet and the westward mesospheric jet.

surface at mid latitude) and the mesospheric jet (which peaks about 55 to 60 km above the Earth's surface and spans approximately 20 km) both play a major role in filtering gravity waves. The jet stream at the lower levels has a consistently eastward flow, though it is stronger in winter than in summer. Gravity waves with eastward horizontal velocities smaller than that of the jet stream never reach the stratosphere and mesosphere; they are filtered out. The mesospheric jet on the other hand, reverses direction during the equinox seasons. In the winter its flow is eastward (in the same direction as the tropospheric jet) while in the summer its flow is westward. As a result, the mesospheric jet has a strong seasonal effect on the upward propagation of gravity waves into the mesosphere. In winter, all gravity waves with westward horizontal phase speeds avoid filtering by the jets, and propagate into the mesosphere (and higher). In summer the gravity waves with eastward horizontal phase speeds that exceed those in the tropospheric jet will propagate into the mesosphere. Because of the higher speed

westward mesospheric jet in summer, gravity waves propagating westward are more likely to be filtered. As a result, in the summer fewer gravity waves propagate into the mesosphere (and higher).

5. Gravity Wave Variability

Much of the seasonal variability of gravity waves in the mesosphere is due to filtering, which leads to more gravity wave activity in the mesosphere in winter than in summer. Some seasonal variations are also due to seasonal changes in gravity wave sources. For example, the orographic source from wind over mountains will vary as the wind activity varies with season and convective activity from storms will vary with season as the storm activity varies. Thus, vertical variability of gravity wave activity is largely due to a combination of filtering effects and source variations.

There is also spatial variability. AGWs increase in amplitude as they propagate upward into regions of lesser density because of conservation of energy. This vertical variation will still have a seasonal variation because vertical density profiles are seasonally dependent. Gravity waves have some longitudinal variation due to source differences, particularly in the case of orographically forced waves because the topography of the Earth's surface varies greatly from mountains to plains to oceans [Nastrom and Fritts, 1992]. There is also a great deal of latitudinal variability because of differences in both sources and filtering. At lower latitudes, gravity waves caused by storm convection are dominant. At mid latitudes, it has been observed that in general there is more gravity wave activity than at higher latitudes. This difference may be due to excitation of waves at mid latitudes by the tropospheric jets [Tsuda *et al.*, 1994].

6. Gravity Wave Potential Energy

One aspect of examining the altitude profiles of density fluctuations and of potential energy per unit mass is to see how these quantities grow with altitude. For non-dissipative gravity-wave propagation, the induced density perturbations will grow smoothly with altitude, in response to diminishing density, in proportion to $\exp(z/2H_\rho)$ as derived in equation (3.1.11). The density scale height, H_ρ , is approximately 7 km in the mesosphere. The perturbation energy per unit mass will ideally increase as $\exp(z/H_\rho)$ as derived in equation (3.1.12). However, the Rayleigh lidar does not yet measure wind velocities. Instead, we can examine the gravity wave potential energy per unit mass $E_p(z)$, which is calculated using either of the equations

$$E_p(z) = \frac{1}{2} \left(\frac{g(z)}{N(z)} \right)^2 \overline{\left[\frac{\rho_1(z)}{\rho_0(z)} \right]^2}, \quad (3.1.13)$$

$$E_p(z) = \frac{1}{2} \left(\frac{g(z)}{N(z)} \right)^2 \overline{\left[\frac{T_1(z)}{T_0(z)} \right]^2}, \quad (3.1.14)$$

[Wilson *et al.*, 1991a], where $T_1(z)$ is the temperature fluctuation and $T_0(z)$ is background temperature. These two equations are equivalent because from the ideal gas law $\left(\frac{\rho_1}{\rho_0} \right)^2 = \left(\frac{T_1}{T_0} \right)^2$. Most importantly, the potential energy per unit mass is almost identical to the perturbation or kinetic energy per unit mass [Tsuda *et al.*, 2000; Sica and Argall, 2007]. Accordingly, $E_p(z)$ will ideally increase as $\exp(z/H_\rho)$.

These equations indicate that we can use either density or temperature fluctuations to calculate gravity wave potential energy. We used density fluctuations observed with the ALO Rayleigh lidar because they are found on shorter time scales and to higher altitudes. It is also easier to estimate $\rho_0(z)$ than $T_0(z)$. Thus, we learn more about the gravity waves from examining density fluctuations. The detailed procedure to calculate the relative density fluctuations and their variance will be discussed in a later section. In equation (3.1.13) we use the lidar temperature data to calculate the square of the Brunt-Väsälä frequency by using equation (3.1.1).

An example of $E_p(z)$ is shown in Figure 8. It increases approximately

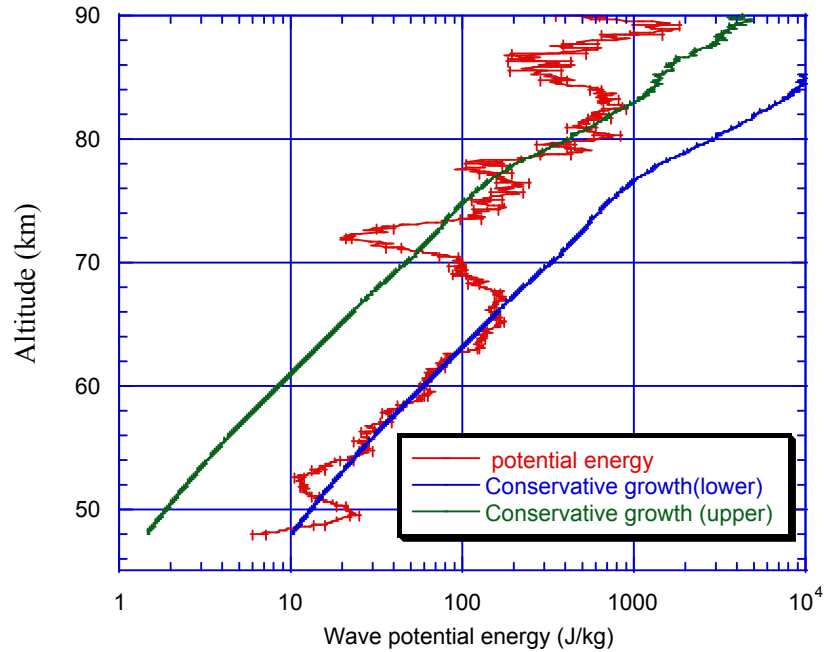


Figure 8. Gravity wave potential energy per unit mass versus altitude for July 23, 1996. The uncertainties are also shown. The blue and the green lines are the corresponding adiabatic energy curves scaled to fit through two regions of the energy profile.

exponentially between 48 and 65 km at a rate that is consistent with the wave amplitude growing adiabatically, i.e. without exchanging energy with the surrounding atmosphere, at $\exp(\Delta z/H_\rho)$. Above 65 km, $E_p(z)$ falls off sharply and then again grows at the adiabatic rate until 83 km. Starting at both 65 and 83 km, E_p falls off quickly by a factor of 5 or so. This indicates that part of the wave energy is given up to the surrounding atmosphere. These two abrupt energy losses are most likely examples of wave breaking.

7. Summary

Gravity waves are a transverse wave supported by the simple harmonic motion of air parcels in a stably stratified atmosphere. The lifting force is buoyancy while the restoring force is gravity. They propagate both vertically and horizontally. They grow in amplitude exponentially with altitude, in response to diminishing density. These waves have frequencies greater than N (Brunt-Väisälä frequency) and less than f (Coriolis parameter), corresponding to periods between 5 minutes and 18 hours at our latitude. They can have vertical wavelengths that range from less than 1 km to more than 20 km and horizontal wavelengths that range from less than 10 km to more than 2000 km. Topography, jet instability, convection, shear generation, etc. are the major sources of these waves. These waves, having their origin in the troposphere, propagate upwards and deposit energy and momentum through wave breaking and dissipation processes in the stratosphere, mesosphere, and thermosphere thereby significantly altering the thermal structure and wind pattern. The GWs thus have significant impact on the dynamical processes in the middle atmosphere. Much of the seasonal variability of GWs is due to

filtering, leading to more GW activity in the mesosphere in winter than in summer. Some seasonal variations are also due to seasonal changes in the sources of AGWs.

This chapter has tried to provide background knowledge about AGWs to better enable the reader to understand the research results presented in next four chapters, which will develop information about AGWs from lidar observations extending through the mesosphere.

CHAPTER 4

CLIMATOLOGY OF MESOSPHERIC BRUNT-VÄISÄLÄ FREQUENCIES DERIVED FROM RAYLEIGH-SCATTER LIDAR OBSERVATIONS ABOVE LOGAN, UTAH

Abstract

Approximately 900 nights of observations with a Rayleigh-scatter lidar at Utah State University (USU), spanning the 11-year period from late 1993 through 2004, have been reduced to derive nighttime temperature profiles $T(z)$ between 45 and ~ 90 km, i.e., over the entire mesosphere. Of these profiles, 150 extending to 90 km or above, were used to make a climatology of Brunt-Väisälä frequency squared, N^2 . These averaged N^2 profiles from the 11 years were combined to obtain a composite annual climatology and its variability. The minimum and maximum values of N^2 over the entire mesosphere vary between $2.2 \times 10^{-4} (\text{rad/s})^2$ and $9.0 \times 10^{-4} (\text{rad/s})^2$. The corresponding buoyancy periods vary between 7.0 and 3.5 minutes. Thus, climatologically, the atmosphere is convectively stable, i.e., $N^2 > 0$. A clear seasonal variation exists with larger values occurring in winter than in summer below 75 km and larger values occurring in summer than in winter above 75 km. This behavior fits well with a downward phase progression of the annual and semi-annual variations in temperature. Indeed, many of the main features in the N^2 climatology can be related to features in the temperature climatology. A comparison of this N^2 climatology to one derived from the NRL-MSISe00 model showed major differences because the model does not have inversion layers or much of a semiannual oscillation.

1. Introduction

The Brunt-Väisälä (buoyancy) frequency, N (rad/s), or its value squared, is an important parameter for determining several aspects of atmospheric gravity waves (AGWs), e.g., maximum frequency of AGWs, the AGW dispersion relationship, the available AGW potential energy, the condition for convective turbulence or instability, a contributing factor to dynamic instability, and by extension the general global circulation. In particular, AGWs only exist when N^2 is positive [Hines, 1991]. When it becomes negative, the atmosphere becomes convectively unstable and they cannot propagate. For positive values, as it varies, the vertical wavelength and speed of AGWs vary. The determination of this parameter involves the temperature T , its gradient $\partial T/\partial z$, and the differences between the actual lapse rate ($\Gamma = -\partial T/\partial z$) and the dry adiabatic lapse rate, $\Gamma_a = g(z)/c_p$, where $g(z)$ is the acceleration due to gravity at altitude z and c_p is the specific heat capacity at constant pressure, 1004 J/K kg. At sea level $\Gamma_a = 9.8$ K/km and at 90 km, $\Gamma_a = 9.6$ K/km.

The N^2 parameter has been studied in the upper mesopause and lower thermosphere (between 80 and 105 km) region by several groups using the resonance-scatter lidar technique at several of sites [e.g. Gardner *et al.*, 2002; Zhao *et al.*, 2003; Liu *et al.*, 2004; Sherman and She, 2006; Gardner and Liu., 2007]. Some studies have also been done in the tropospheric and lower stratospheric (between the ground and 30 km) regions of the atmosphere [e.g., Whiteway, 1998; Tsuda *et al.*, 2000; Vincent and Alexander, 2000; Gavrilov and Fukao, 2004] and the region between 30 and 80 km has been examined with rocket observations [Charney and Drazin, 1961]. However, to our

knowledge, the climatology of this parameter has not yet been examined over the entire mesosphere. This is a particularly interesting region, especially the mesosphere between 45 and 90 km, because convective instabilities associated with $N^2 < 0$ often occur. They have been reported to develop on the topside of inversion layers [*Hauchecorne et al.*, 1987; *Whiteway et al.*, 1995; *Sica and Thorsley*, 1996] and we suspect they also probably occur in conjunction with large amplitude waves.

Establishing an empirical climatology of N^2 profiles at a variety of sites is an essential element to understanding the physics of this region. We can contribute to this because of our extensive observations at Utah State University (USU).

In this paper, we present the mesospheric N^2 climatology from measurements made with the Rayleigh-scatter lidar on the USU campus at the Atmospheric Lidar Observatory (ALO), which is operated by the Center for Atmospheric and Space Sciences (CASS). We emphasize mesospheric N^2 profiles from all-night observations: how the observations were made, how the buoyancy frequencies were calculated, as well as the ALO N^2 climatology and the N^2 variability. The measurements and analysis method are presented in section 2, results and discussion are presented in section 3, and summary and conclusions are given in section 4. As part of this research, comparisons are made with N^2 values calculated from the NRL-MSIS00 [*Picone et al.*, 2002] empirical model of the neutral atmosphere.

2. Measurements and Analysis Method

The Rayleigh-scatter lidar system at ALO is located in Logan, Utah, on the USU campus (41.74°N, 111.81°W, 1.47 km above sea level). It was operated from late 1993

through 2004, giving rise to an extensive database of nighttime, mesospheric profiles of relative densities and absolute temperatures. The ALO Rayleigh lidar is a vertically pointing, coaxial system. It consists of a frequency-doubled Nd:YAG laser producing 18-24 watts at 532 nm and at 30 Hz, a 44-cm diameter Newtonian telescope. The single, gated detector is a green-sensitive, bialkali photomultiplier tube (Electron Tubes 9954B) in a Peltier-cooled housing. To protect the detector from the extremely large low-altitude backscattered light, the signal from below ~ 18 km is blocked by a mechanical chopper and below 38 km the detector gain is reduced by almost 10^3 by an electronic gate. This setup produces good data from 45 km to approximately 90 km. A narrow-band interference filter (1 nm) is used to remove most of the background light from stars, moon, airglow, and scattered city lights. A more extensive description of this system is given by *Beissner* [1997], *Wickwar et al.* [2001], *Herron* [2004, 2007], and *Herron and Wickwar* [2009a].

A total of more than 900 nights of observations were collected. Of these all-night profiles, 150 extend to 90 km or above. They were selected for this N^2 climatology. While including more nights would improve the statistics at lower altitudes, we are particularly interested in including the top 10–15 km for this and other studies. The data on these nights were collected continuously for periods of 4 to 12 hours. The recorded raw data is in the form of photon-count profiles with an altitude resolution of 37.5 m (250-ns sampling interval) from the ground to 500 km and a temporal resolution of 2 minutes (3600 laser pulses). The data of interest for this study start at 45 km. At each altitude z the observed photon-counts are the sum of a background signal (from the detector, moonlight, starlight, airglow and scattered city lights) and the signal of interest

from the backscattered laser pulse. The background signal is determined between 120 and 180 km and subtracted from the total. This remaining signal, multiplied by the square of the range from the laser (not the square of the altitude), is proportional to the atmospheric number density $n(z)$ assuming a constant mean-molecular mass m and, hence, composition in the portion of the atmosphere we are interested in. However, the constant of proportionality may vary from one 2-minute profile to the next because of variations in the atmosphere's transmittance or changes in the power of the laser. To reduce the influence of signal fluctuations caused by these effects, the profiles are normalized to unity at 45 km. Before doing so, the data are averaged over 3 km (81 samples) and over the whole night. Temperatures are determined from these relative densities by using hydrostatic equilibrium and the ideal gas law. The temperatures $T(z)$ are the sum of two terms:

$$T(z) = T(z_{\max}) \frac{n(z_{\max})}{n(z)} + \frac{1}{kn(z)} \int_z^{z_{\max}} m(z')g(z')n(z')dz'. \quad (4.1.1)$$

The integration runs from the altitude of interest z to the maximum altitude z_{\max} at which $T(z_{\max})$ is the supplied initial value, k is Boltzman's constant, and $m(z)$ is held constant for this altitude range. The details of the data reduction, as applied to this lidar, are reviewed by *Beissner* [1997], *Wickwar et al.* [2001], *Herron* [2004, 2007], and *Herron and Wickwar* [2009a].

To calculate the absolute temperature, an a priori value of the temperature at z_{\max} is needed. The initial values are taken from the 8-year climatology from the sodium lidar at Colorado State University (CSU) [*She et al.*, 2000], which is only 575 km away and

just over 1° equatorward of ALO. The CSU temperatures were from 1990 to 1999, covering much of the same time period as the ALO data. The use of this nearby climatology should be more appropriate than using an empirical model such as NRL-MSISE00 [Picone *et al.*, 2002], especially in view of the low model temperatures in the upper mesosphere discussed in Herron and Wickwar [2009b]. In any case, any systematic error from this initial temperature decreases very rapidly with the downward integration. For instance, a difference between the initial and actual temperatures decreases by a factor of ~ 4 after 10 kms of integration. The starting altitude z_{\max} for the temperature integration is usually determined as the point where the signal is 16 times its standard deviation. However, for this analysis it is set to that value or to 95 km, whichever is lower.

At the upper limit of the lidar's range, the background becomes a large portion of the total signal. Its accurate determination in the region above 120 km is most important for the data reduction, because a bad background leads to a systematic temperature error at all altitudes [Herron, 2004]. Observationally, bad backgrounds can have slopes, oscillations, or spikes. To minimize potential background problems, the background region was chosen specifically for each night and each night reduced separately. In addition, subsequent averaging of many nighttime temperatures to produce the climatology further reduces any errors from the background selection. The temperature profiles used here are included in the Herron and Wickwar [2009a] climatology, i.e., this is not a new (and different reduction) of the data.

Using these derived, absolute, nighttime, averaged, temperature profiles $T(z)$ the temperature gradient profiles $\partial T(z)/\partial z$ are calculated by applying the IDL numerical

differentiation routine, which uses 3-point, Lagrangian interpolation. The corresponding averaged $N^2(z)$ profiles are calculated according to

$$N^2(z) = \frac{g(z)}{T(z)} \left[\frac{\partial T(z)}{\partial z} + \frac{g(z)}{c_p} \right]. \quad (4.1.2)$$

The variance for the $N^2(z)$ profiles are calculated according to

$$\sigma_{N^2}^2 = \left[\frac{N^2(z)}{T(z)} \right]^2 \sigma_T^2 + \left[\frac{g(z)}{T(z)} \right]^2 \sigma_{\frac{\partial T}{\partial z}}^2, \quad (4.1.3)$$

where σ_T^2 is the temperature variance, which is derived analytically from equation (4.1.1) by propagating the uncertainty in the photon-counts [e.g., *Gardner*, 1989; *Beissner*, 1997; *Herron*, 2004, 2007]. The temperature gradient variance $\sigma_{\frac{\partial T}{\partial z}}^2$ is calculated using the IDL routine. This temperature gradient variance is closely related to σ_T^2 , which was found from the propagation of the Poisson measurement uncertainty. This means that the variance $\sigma_{N^2}^2$ is also closely related to the propagation of the Poisson uncertainty. The contribution of the covariance term to $\sigma_{N^2}^2$ was examined, but did not make a significant contribution. Consequently, we treated $T(z)$ and $\partial T(z)/\partial z$ as independent.

Examples of $T(z)$, $\partial T(z)/\partial z$, $N^2(z)$, and the corresponding Brunt-Väisälä periods $\left(\tau_b = 2\pi/\sqrt{N^2} \right)$ between 45 and 90 km are shown for individual days in Figures 9a-c and 10a-c to illustrate winter and summer behaviors. These two examples also show the effects of temperature inversions in all three parameters. On February 21, 1995, a large inversion occurs with its maximum temperature at 74 km. The temperature gradient has a zero value at this temperature maximum and at the temperature minimum at 67 km,

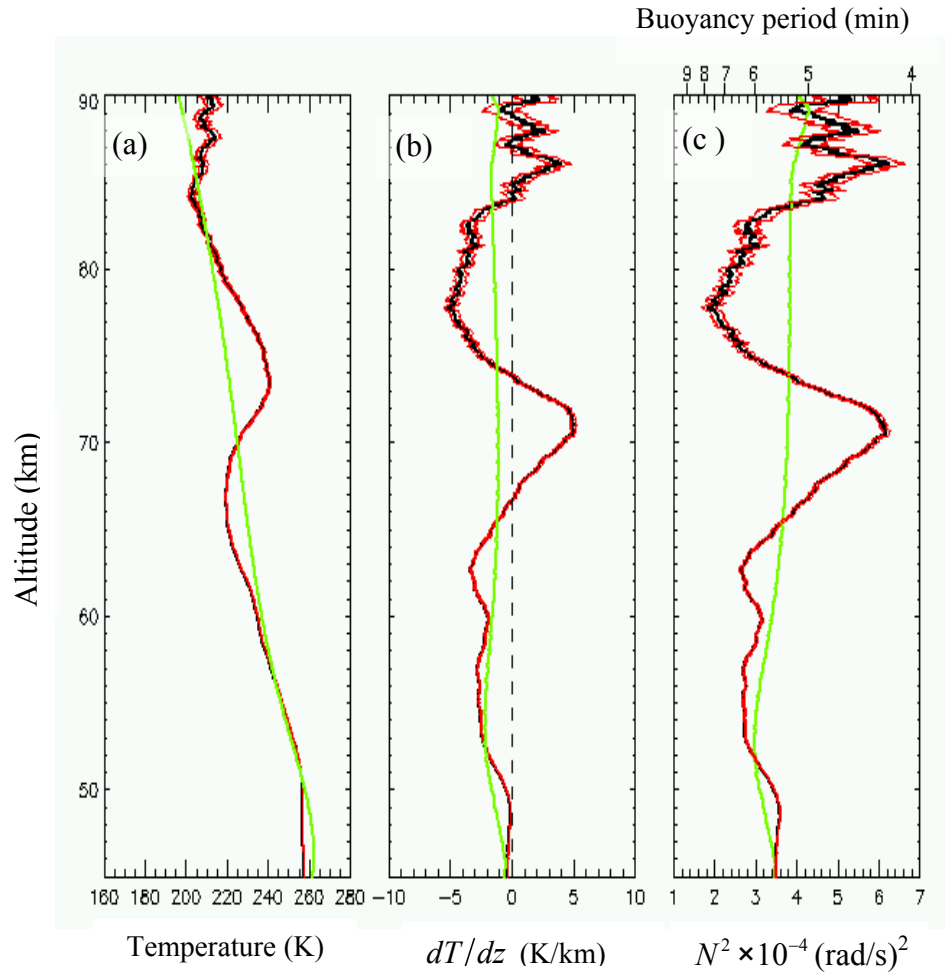


Figure 9. Profiles related to finding N^2 for February 21, 1995. These include the (a) temperature, (b) temperature gradient, and (c) buoyancy frequency squared and buoyancy period. The red curves give the $1-\sigma$ uncertainties, based on the measurement uncertainty. Corresponding parameters based on the NRL-MSIS00 model are shown in green.

which marks the beginning of the inversion and is often given as the altitude of the inversion. In between these altitudes, at 71 km, the gradient and N^2 both have maxima. On July 23, 1996, a smaller, but distinct structure or bump occurs between 72 and 75 km on the temperature profile. In that sense it is a small inversion. However, it is small enough that the zero gradients for the inflection and peak merge together between 72 and 75 km. Nonetheless the gradient and N^2 profiles have distinct relative maxima centered

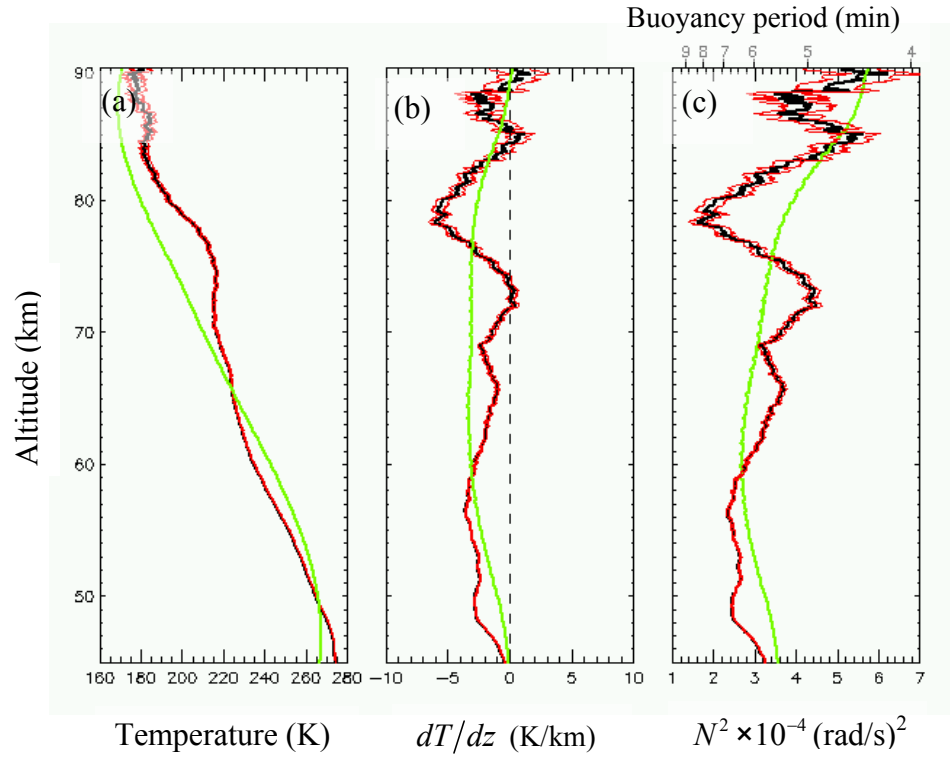


Figure 10. Profiles related to finding N^2 for July 23, 1996. These include the (a) temperature, (b) temperature gradient, and (c) buoyancy frequency squared and buoyancy period. The red curves give the 1- σ uncertainties, based on the measurement uncertainty. Corresponding parameters based on the NRL-MSIS00 model are shown in green.

on 73 km. On both days there are small changes in the gradients at lower and higher altitudes, which may reflect secondary inversions or wave activity that lead to relative maxima in the gradients and in N^2 . A point to notice is how fast N^2 increases on the bottom side of the inversion layer and how fast it decreases on the top side. Clearly, the figures show that the altitude variation in N^2 is very similar to that of $\partial T / \partial z$. That is expected from equation (4.1.2) because the adiabatic lapse rate is nearly constant and $T(z)$ varies only by about 20% near an inversion, while $\partial T / \partial z$ varies considerably. The effect of propagating the 1- σ measurement uncertainties are shown by red lines for all

three quantities. They are small enough that both the gradient and N^2 are very well determined all the way up to 90 km for these all-night integrations.

For comparison to these derived values, the corresponding values from the NRL-MSISe00 model [Picone *et al.*, 2002] are also shown in both figures. This is typically considered the best empirical model. While considerable similarity exists, some major differences are quite obvious. The three ALO profiles for each of the two days show large variations with altitude, especially near the inversions that have maximum temperatures at 74 km in February and 75 km in July, whereas the corresponding model values are much smoother. On the bottomside of the inversion layer, the temperature gradient becomes positive and N^2 becomes much bigger. On the topside, the temperature gradient becomes negative and N^2 becomes much smaller. Sometimes, though not in these two examples, the temperature gradient can become so much more negative that N^2 becomes zero or negative. This relationship among temperature structure, temperature gradient, and Brunt-Väisälä frequency is very clear in parts a, b, and c of these figures. In addition, examination of these three profiles for a given night show what appear to be wave structures with about a 12-15 km vertical wavelength on February 21, 1995 and a 7.5-12 km vertical wavelength on July 23, 1996 below the inversion layer and, perhaps, above it. These waves lead to structure in the N^2 profile. In addition, the model is systematically too cold in the upper mesosphere on the July day, in agreement with the more extensive comparison by Herron and Wickwar [2009b].

Thus, we have examined how to determine the Brunt-Väisälä frequency squared throughout the mesosphere starting from the Rayleigh-scatter lidar observations. We have also shown winter and summer examples based on all-night data averages and

compared them to the best current empirical model. The observations are much more variable than the model, apparently reflecting inversion layers and monochromatic gravity waves, leading to both smaller and larger values of N^2 and the corresponding Brunt-Väisälä periods τ_b . These examples show N^2 values of $2\text{--}6 \times 10^{-4} \text{ (rad/s)}^2$ and corresponding τ_b values of 8–4 minutes. While these values are fairly typical, an examination of the whole data set extends both limits. In addition, the smallest N^2 values (and longest periods), while depending on the temperatures on a particular day, are also a function of the integration time. On a few nights in this data set (see Chapter 7), N^2 is zero or negative for the all-night averages. Shorter integration times (see Chapter 7) uncover many more brief periods when N^2 is zero or negative, i.e., when convective instability occurs. However, for this climatological study the basic integration times come from all the observations on a given night, which can range from 4 to 12 hours, and then from averaging all these results over a 31-day or a seasonal window spanning 11 years.

Following up on the similarity of the $\partial T/\partial z$ and N^2 profiles, we examined the climatology of temperature gradients. We averaged all the all-night average gradient profiles over a 31-day window spanning 11 years centered on each night to see the general features of inversion layers in the ALO data. This climatology is given in Figure 11. Over most of the year, the gradient is positive at and just above 45 km, indicating a gradient is more positive (i.e. bottomside of temperature inversions) between 68 and ~75 km and 80 and 85 km. From May through September the positive temperature gradient occurs between ~80 and 90 km, most likely reflecting the lower thermosphere. The

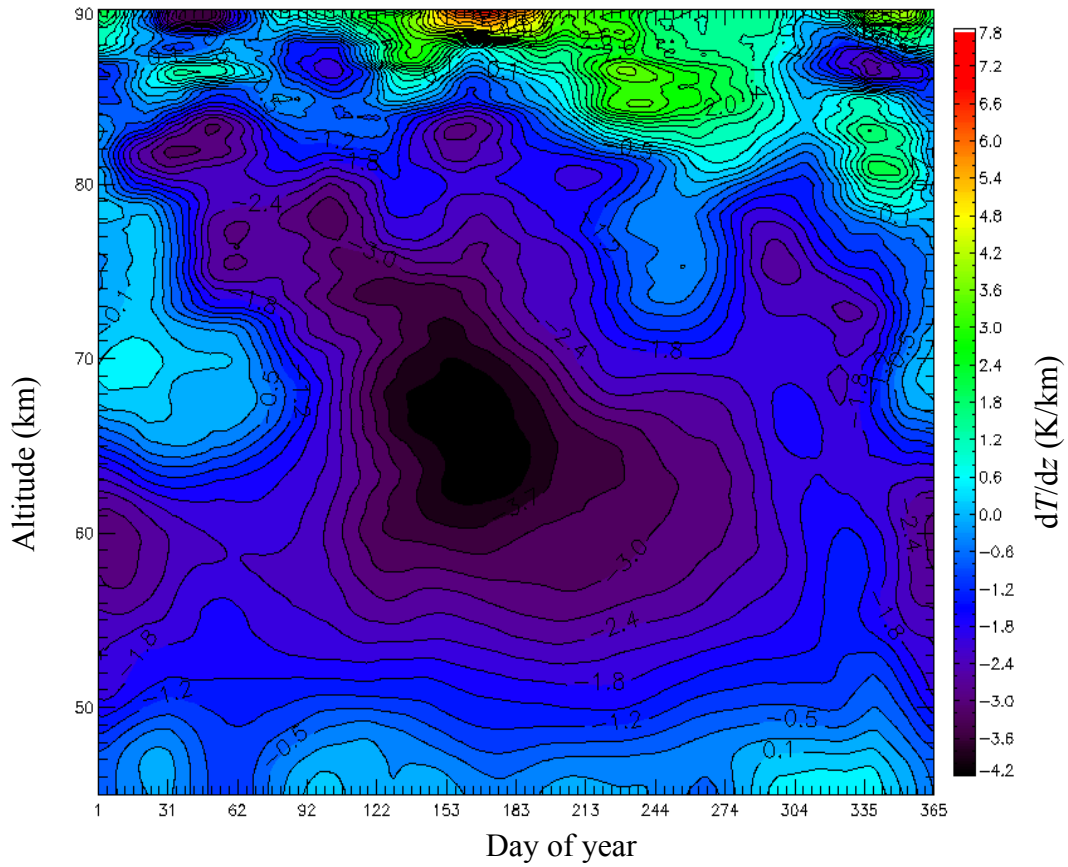


Figure 11. Temperature gradient climatology above USU from 1993-2004 Rayleigh lidar observations. Each profile is the result of a 31-day multiyear average of nights that extend above 90 km.

temperature gradient climatology shows both annual and semi-annual variations with downward phase progression. From what we saw in Figures 9 and 10, this temperature gradient climatology gives us a preview of what the N^2 climatology will look like. It will be discussed in Section 3.1.

3. Results and Discussion

3.1. Climatology of the Brunt-Väisälä Frequency-Squared

We made a multiyear average of all the $N^2(z)$ profiles from each month within the 11-year period. These monthly N^2 profiles are shown in Figure 12. Overall, the values

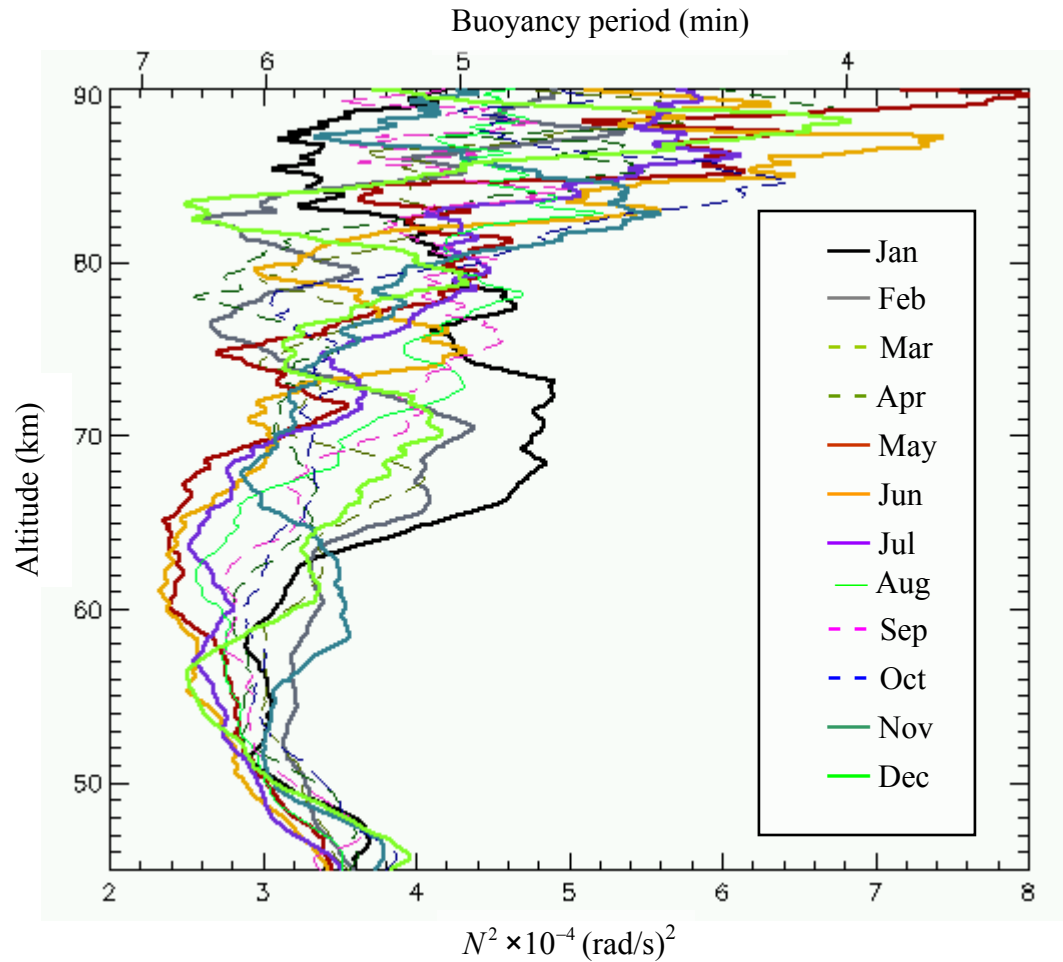


Figure 12. Monthly averaged N^2 values above USU from the 1993-2004 observations.

range between 2.2×10^{-4} and $8.0 \times 10^{-4} \text{ (rad/s)}^2$ with a relative maximum at 45 km, a minimum at 60 ± 5 km, and a maximum near 90 km. The corresponding periods are 7.0–3.7 minutes. The minimum value of $2.2 \times 10^{-4} \text{ (rad/s)}^2$ shows that for these long integrations, the atmosphere is convectively stable. In more detail, there appears to be a seasonal variation in these curves with the biggest differences between winter (November, December, January, and February) and summer (May, June, July, and August). In winter N^2 values decrease to a minimum centered on 55 km and then increase to a maximum centered on 70 km. Above this maximum, and especially above

80 km, the values become more variable with increasing altitude, tending to decrease and then increase. In summer N^2 values decrease to a smaller minimum centered on 65 km, increase to a relative maximum near 80 km, and then increase to values greater than the winter values by 90 km. Again, the values become much more variable above 80 km. Both spring equinox (March and April) and fall equinox (September and October) values tend to be between the winter and summer values below 70 km and above 85 km. In between, there is a tendency for the spring values to be small and the fall values large.

Another way to present the time and altitude variation is as a contour plot extending over a composite year. The values are calculated in the same way as for the temperature climatology [Herron and Wickwar, 2009a] and the temperature gradient climatology shown in Figure 11. For each day of the year an average is made over 31 days centered on the day and spanning 11 years. The results are shown in Figure 13. As seen in Figure 13, between 50 and 80 km or so there is a semi-annual structure. The smallest values occur in summer near 1 June at 63 km. It appears to be part of a region of comparatively small values that propagates down from early December at 85 km. Another region of small values is centered on 1 January at 56 km. It too appears to propagate down, starting near mid October at 80 km. A region of comparatively large values extends upward from about 55 km in February to 80 km in December. Another extends from 55 km in late November to 85 km in August. Below 50 km the semi-annual variation is replaced by four relative maxima. Above approximately 85 km the values are significantly bigger than elsewhere, with the maximum values centered on early June.

Figures 12 and 13 show that, climatologically, the atmosphere is convectively stable, with minimum gravity wave periods ranging from 3.5 to 7.0 minutes. While the

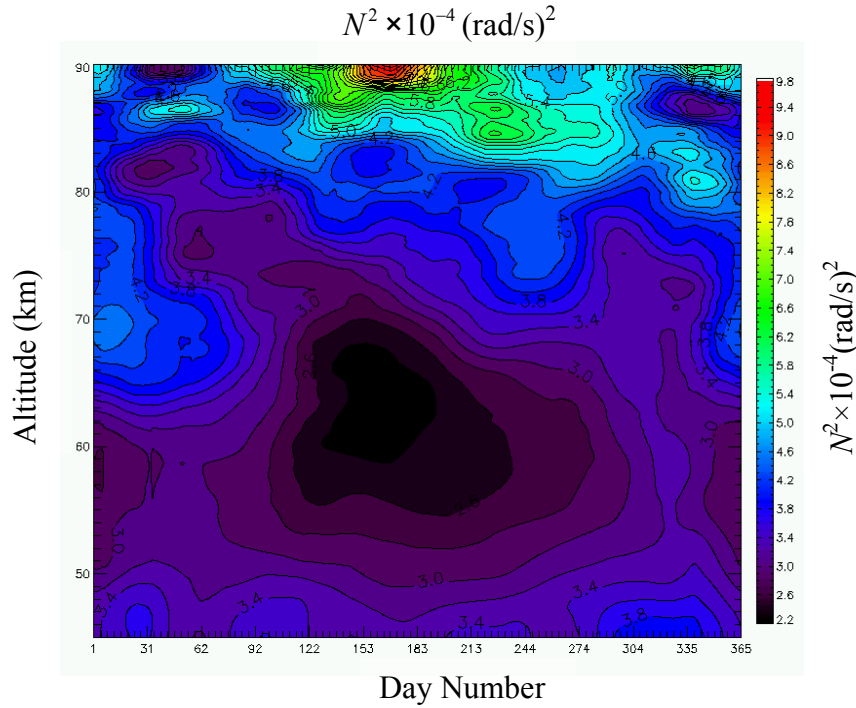


Figure 13. N^2 climatology above USU from 1993-2004 Rayleigh lidar observations. Each profile is the result of a 31-day multiyear average of nights that extend above 90 km.

climatology based on these all-night, multiyear averages shows a stable mesosphere, shorter averages over an hour or even a whole night can show $N^2 \leq 0$. Thus, periods of convective instability do exist, but they are more limited in time and altitude, placing them beyond the scope of this climatology paper.

3.2. Seasonal Variation of N^2

The variability from month to month in Figure 12 suggests that more insight into the seasonal behavior of N^2 could be gained by additional smoothing. In addition, because the N^2 values are dependent on temperature and, especially, temperature gradient, these quantities must be examined simultaneously. For this, we average the T , $\partial T / \partial z$, and N^2 values according to season, where the seasons are defined, as in the

previous section, by their similar N^2 behaviors. The results are shown in Figures 14a and b. The N^2 averages show a clear seasonal variation, one that differs below and above 70–75 km. Below that altitude, the maximum N^2 value ($4.2 \times 10^{-4}(\text{rad/s})^2$) is observed in winter and the minimum value ($2.5 \times 10^{-4}(\text{rad/s})^2$) in summer. The spring and fall values lie in between the summer and winter values. Above that altitude region, the profiles are more structured, the maximum solstice N^2 value ($5.5 \times 10^{-4}(\text{rad/s})^2$) occurs in summer and the minimum solstice value ($3.2 \times 10^{-4}(\text{rad/s})^2$) occurs in winter along with an equinox

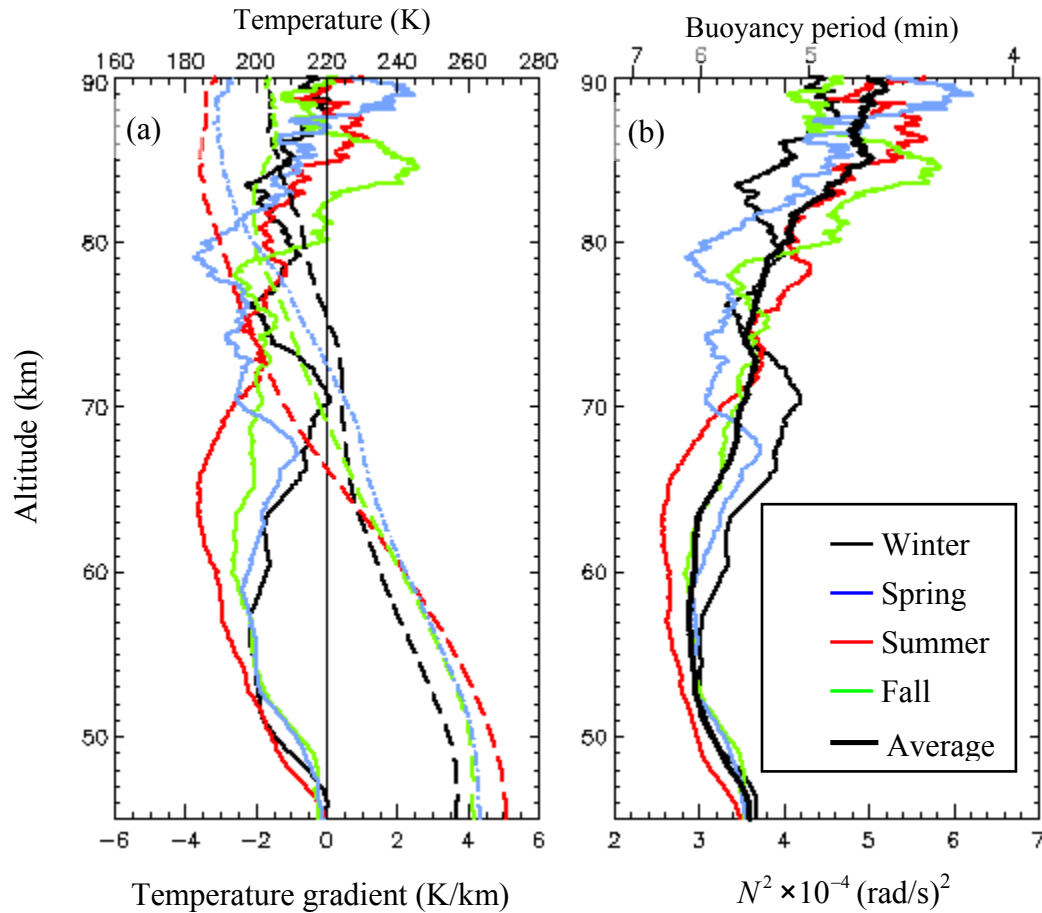


Figure 14. Profiles showing seasonal variation of temperature, temperature gradient, and N^2 . (a) Temperatures are shown as colored dashed curves and gradients as colored solid curves. (b) N^2 values are shown as colored curves and the annual mean as a thick black curve.

maximum value of $(6.2 \times 10^{-4} \text{ rad/s})^2$ in fall equinox and an equinox minimum value of $(2.8 \times 10^{-4} \text{ rad/s})^2$ in spring.

The annual mean values of N^2 are shown as a thick black curve in Figure 14b, varying between $2.8 \times 10^{-4} \text{ (rad/s)}^2$ and $5.2 \times 10^{-4} \text{ (rad/s)}^2$ over the entire mesosphere with corresponding periods of 6.2 and 4.6 minutes. The same N^2 values and corresponding buoyancy periods are presented every 3 km in Table 1. The typical values for uncertainties in N^2 and period at 70 km are $0.2 \times 10^{-4} \text{ rad/s}$ and 0.2 min, respectively. See Table 2 for more detail.

Table 1. Annual Mean Rayleigh Lidar N^2 Values for the Mesosphere Above Logan, UT

Altitude (km)	45	48	51	54	57	60	63	66	69	72	75	78	81	84	87	90
N^2 (rad/s) ²	3.5	3.3	3.0	2.9	2.8	2.9	3.0	3.3	3.4	3.6	3.6	3.7	4.1	4.7	5.2	5.0
Period (min)	5.5	5.7	6.0	6.1	6.2	6.1	6.0	5.7	5.6	5.4	5.4	5.4	5.1	4.8	4.6	4.7

As seen in Figure 14a, in the lower mesosphere, the temperatures have a maximum in summer and minimum in winter, consistent with radiative control. The opposite seasonal behavior of the N^2 values in Figure 14b is largely attributed to the seasonal differences in the temperature gradient. The gradient is more negative in summer than in winter below 83 km. In the upper mesosphere, the temperatures have a maximum in winter and a minimum in summer, consistent with dynamic control and the two-level mesopause [She and von Zahn, 1998]. Again, N^2 in Figure 14b exhibits the behavior opposite to that of the temperatures. In this region it is attributed to a

Table 2. Examples of Uncertainties Calculated for N^2 at Various Altitudes

Altitude (km)	45	50	60	70	80	90
$\sigma_{N^2} \times 10^{-4}$ (rad/s)	0.02 (3.5)	0.03 (3.2)	0.08 (2.9)	0.20 (3.4)	0.50 (4.0)	1.1 (5.0)

combination of the seasonal differences in temperature and temperature gradient in Figure 14a. The increase in N^2 at 90 km relative to 45 km comes largely from the decrease in mesospheric temperature from 45 to 90 km. The structure largely arises from changes in the gradient. For example, the bump in N^2 in winter between 65 and 73 km arises from the effect of inversion layers in the averaged temperature profile.

Because of the large amount of data averaging, the winter temperatures in Figure 14 show a region of nearly constant temperature and near zero gradient in the vicinity of 70 km instead of a distinct inversion layer. However, this is sufficient to give rise to a bump in N^2 values. All-night and 1-hour averages (not shown) show stronger inversion layers and bigger N^2 bumps. During summer and equinoxes above about 80 km, the temperature gradients become less negative, zero, or even positive giving rise to N^2 maxima. *Hauchecorne et al.* [1987] and *Whiteway et al.* [1995] showed that the number of inversion events observed during northern mid-latitude winter has a maximum between 55 and 72 km. In contrast, the number of inversion events observed in summer has a maximum between 70 and 83 km. This change in the inversion layer altitude affects the seasonal variation of N^2 . On the bottom side of an inversion layer, N^2 values are large because $\partial T / \partial z$ becomes positive. On the topside of an inversion layer the N^2 values often decrease enough that N^2 becomes small and on occasion negative [*Hines*, 1991; *Whiteway et al.*, 1995; *Sica and Thorsley*, 1996; *Gardner et al.*, 2002; Chapter 7]. This

behavior leads to a seasonal change in the N^2 peak altitude centered about 75 km. Above 75 km, we generally observed higher N^2 values ($5.8 \times 10^{-4}(\text{rad/s})^2$) during summer and lower N^2 values ($3.2 \times 10^{-4}(\text{rad/s})^2$) during winter. Just below 75 km, we generally observed higher N^2 values ($4.2 \times 10^{-4}(\text{rad/s})^2$) during winter and lower N^2 values ($2.5 \times 10^{-4}(\text{rad/s})^2$) during summer. Both equinox seasons show secondary maxima at 80 km, 85 km and 90 km. The larger N^2 values during summer above 80 km may also be associated with the lower altitude of the summer mesopause and increasing temperatures above it. This also shows that during summer the inversion events above ALO are very rare or they exist only above about 80 km which is almost consistent with that reported by *Hauchecorne et al.* [1987] and *Whiteway et al.* [1995]. However, a detailed analysis of inversion events over ALO needs to be done to verify this.

3.3. Annual and Semiannual Variation of N^2

The seasonal variation was further examined by fitting the all-night values of N^2 with annual and semiannual variations. For this analysis, the all-night average values of N^2 were least squares fitted at each altitude by a constant and five sinusoids (24 hours and 4 harmonics). However, a comparison of the amplitudes of the different components of the fit with the measurement uncertainty σ_{N^2} showed that the amplitudes of the harmonic fits for periods shorter than 6 months (not shown) are significantly smaller than the σ_{N^2} values, which are shown in Table 2. In Table 2, the actual annual mean values are given inside the parentheses (from Table 1). In addition, the chi-square χ^2 values for the fits were not significantly reduced by including the higher harmonics. Therefore we are working with only the constant, annual, and semi-annual components. Examples of the

fits at six altitudes: 45, 50, 60, 70, 80, and 90 km are shown in Figure 15. In Figure 15, while the harmonic fits nicely represent the N^2 values, the daily points have great variability, which increases dramatically with altitude. This variability is much greater than the measurement uncertainty, which as mentioned above, is given in Table 2. For instance, the root mean square variation (rms) about the fit at 90 km is $1.2 \times 10^{-4} \text{ (rad/s)}^2$, whereas at 45 km it is only $0.05 \times 10^{-4} \text{ (rad/s)}^2$. Between 60 and 90 km, the growth rate of this rms value has an e-folding distance of 12 km. As already mentioned, both annual and semi-annual amplitudes grow considerably with increasing altitude. However, between 60 and 90 km, they grow a little more slowly than the rms value. Their growth rate has an e-folding distance of 16 km.

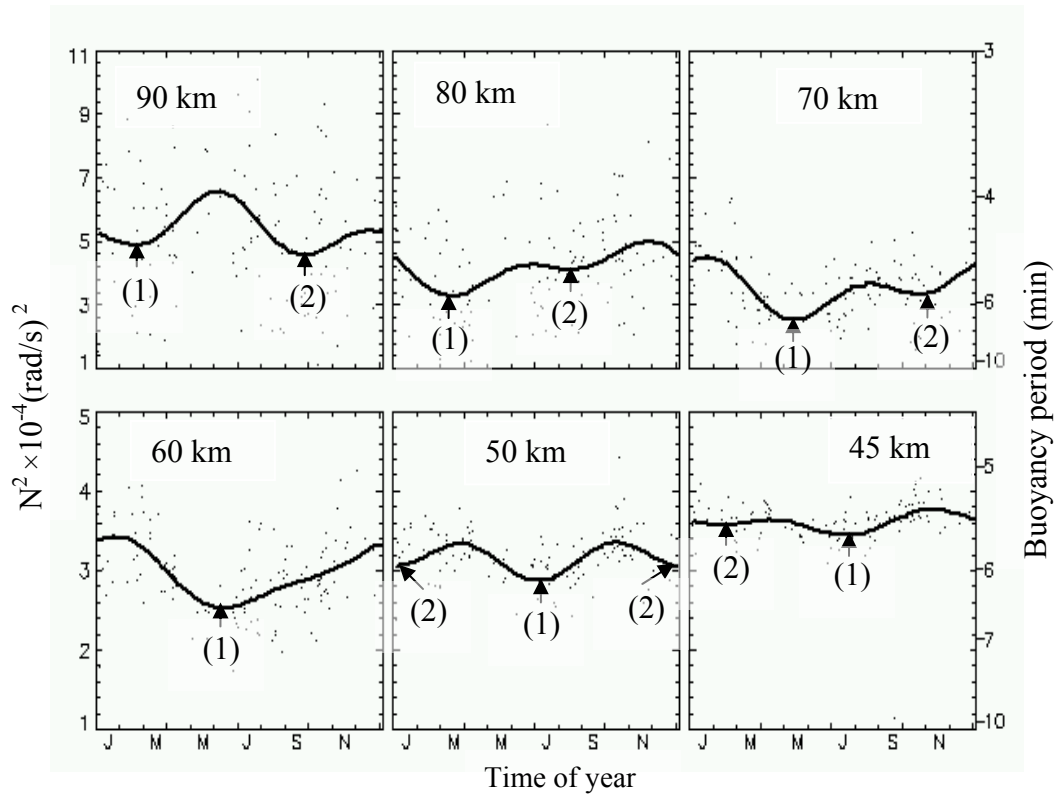


Figure 15. Variations of N^2 throughout the year at several altitudes. Individual days are given as dots. A least squares fit to a constant, annual, and a semi-annual terms is given by the smooth curves. Arrows indicate the observed minima, showing significant annual and semi-annual variations. (The scales are different on the upper and lower panels.)

They show significant annual and semiannual variations. Profiles of the constant, annual, and semi-annual amplitudes and phases from 45 to 90 km are shown in Figure 16a-e. The constant value curve matches the average curve in Figure 14b. Magnitudes of both variable components are very similar and approximately 5-20% of the mean N^2 values. Because they exceed the uncertainty of the mean value at most altitudes, they are significant. The phases show downward phase progressions, as strongly suggested in Figures 13, 14 and 15. The annual variation has a downward phase progression from 90 km to 67 km, and is constant from 67 to 45 km. Between 90 and 67 km it changes phase by approximately 230° . The semi-annual variation has an almost constant downward phase progression over the full altitude range. Between 90 and 67 km it shifts by 75° , whereas between 90 and 45 km, it shifts by approximately 150° . This difference in the downward phase progressions is also very clear in Figure 15, where arrows have been added to show the relative minima. Furthermore, Figure 15 clearly shows the almost 180° phase change between summer and winter between 60 and 90 km. At 90 km the annual and semiannual phases coincide in May-June. At 60 km the annual phase has shifted by almost 180° and the semi-annual amplitude is almost zero.

In addition to accounting for some of the other observations, the approximate factor of three differences in the rate of downward phase change between 90 and 67 km, and the different phase behaviors below 67 km indicate different origins for the annual and semi-annual phase variations. In addition, the annual and semiannual amplitudes increase from $0.1 \times 10^{-4} \text{ s}^{-2}$ at 45 km to $0.9 \times 10^{-4} \text{ s}^{-2}$ at 90 km with a relative maximum between 65 and 70 km and with near zero values of the semi-annual component between 52 and 62 km.

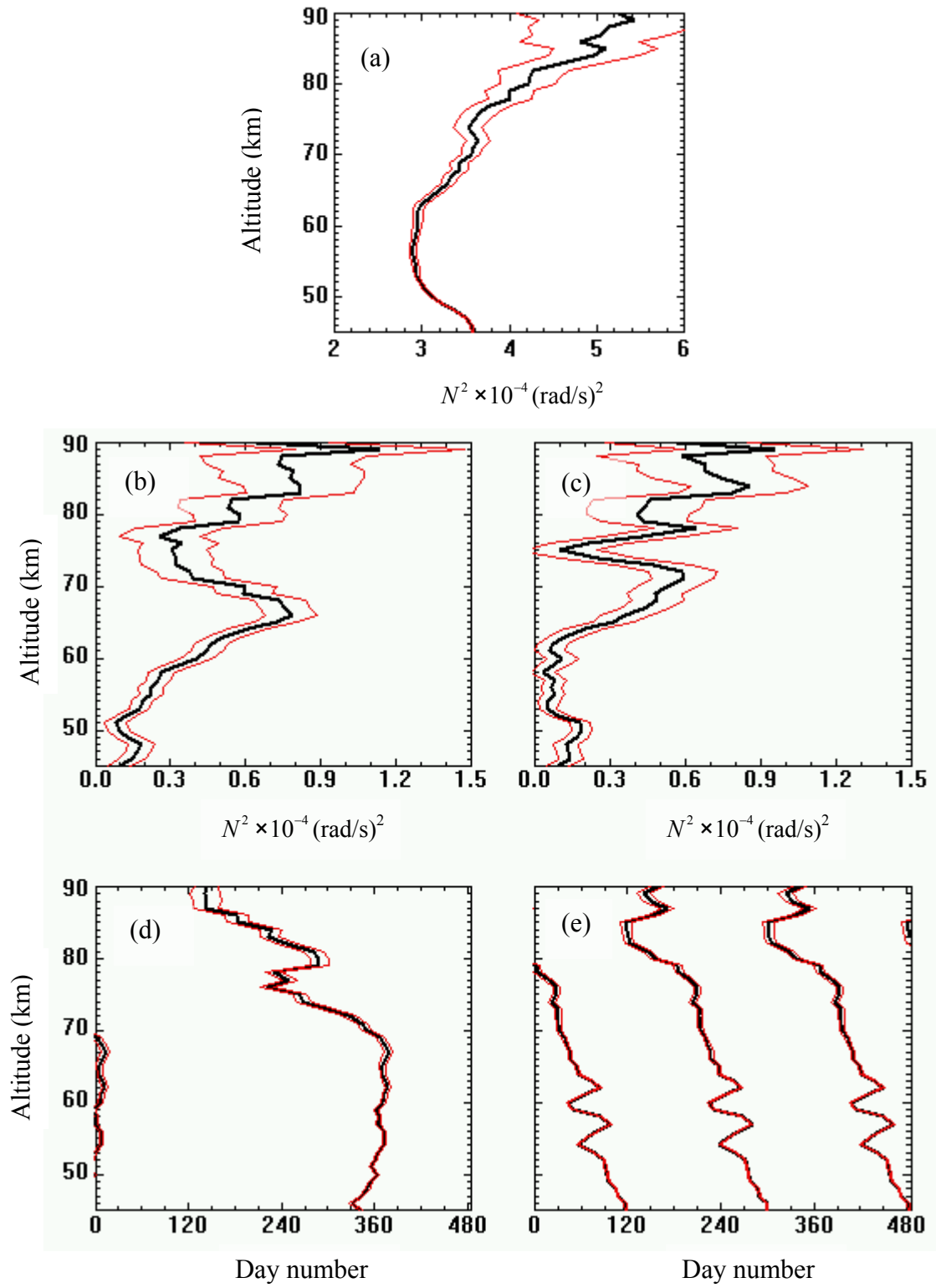


Figure 16. Profiles of mean N^2 , annual, and semi-annual amplitudes and phases. (a) Mean N^2 from fit, (b) annual amplitudes, (c) semi-annual amplitudes, (d) annual phases, (e) semi-annual phases. Uncertainties are shown as red curves.

3.4. Geophysical Variability

As apparent in Figures 12, 14, 15, and 16, the N^2 variability increases rapidly with altitude. It exceeds the propagated uncertainty from the measurements, for which examples are shown in Figures 9 and 10 for individual days and typical values are given in Table 2. Thus this is mostly geophysical variability. The total variability $\sigma_{N_T^2}^2$ for each night measurement and geophysical was calculated using the multiyear monthly averaged N^2 profile and the individual nighttime N^2 profiles for that month. Although the measurement uncertainty is small compared to the geophysical uncertainty at lower altitudes, it can make an appreciable contribution at higher altitudes. To properly assess the geophysical uncertainty, the measurement uncertainty has to be taken into account. To do this, the variance from the measurement uncertainty is subtracted from $\sigma_{N_T^2}^2$ [Whiteway and Carswell, 1995; Leblanc et al., 1998; Argall and Sica, 2007]. The results are the geophysical variance and standard deviation $\sigma_{N_G^2}^2$ and $\sigma_{N_G^2}$, for each night. The rms value of $\sigma_{N_G^2}$ for each season was calculated by averaging the nighttime geophysical variance, $\sigma_{N_G^2}^2$, profiles for a particular season and taking the square root of that seasonal average. The results for all four seasons are shown in Figure 17a.

Figure 17a shows that the seasonal geophysical $\sigma_{N_{GS}^2}$ values grow with altitude for all seasons. The seasonal $\sigma_{N_{GS}^2}$ values are compared with an exponential curve with an e-folding distance of 20 km (the pink curve) during summer and equinoxes and an e-folding distance of 30 km (gray curve) during winter. These increases in $\sigma_{N_{GS}^2}$ with altitude generate an obvious question as to why this increase happens.

This behavior appears to be related to wave activity in the atmosphere. For the propagation of AGWs and tides, the rms temperature (and density) perturbations are expected to grow exponentially with altitude in response to competition between diminishing density and energy loss to the surrounding atmosphere [Hines, 1960]. To examine how the wave-induced perturbations grow with altitude, the rms geophysical temperature variability σ_T was calculated for the same data and are shown in Figure 17b. The σ_T shows an exponential growth with an e-folding distance of 20 km (pink curve) during summer and equinoxes and an exponential growth with an e-folding distance of 30 km (gray curve) during winter. This altitude growth is almost identical to that of $\sigma_{N_{GS}^2}$.

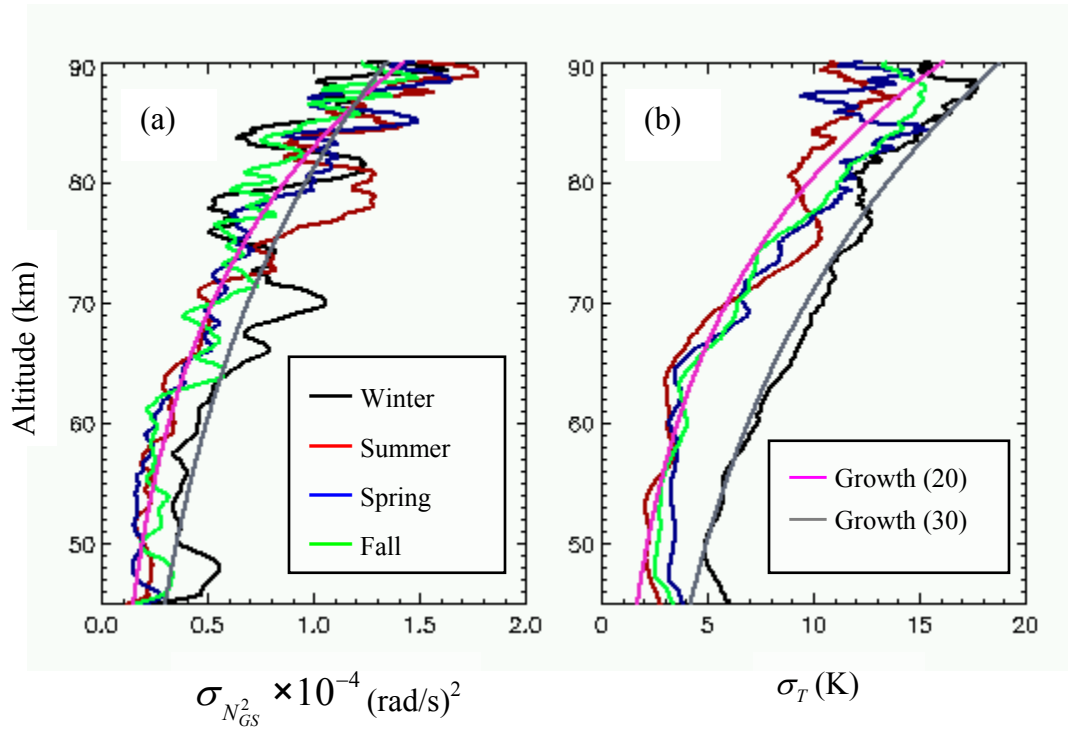


Figure 17. Growth of the geophysical variability of N^2 and T with altitude. (a) Seasonal variation of $\sigma_{N_{GS}^2}$ for the ALO climatology calculated with respect to 11-year monthly mean values of N^2 — black (winter), red (summer), blue (spring equinox), and green (fall equinox). (b) Same as (a) except for σ_T for temperature. In both (a) and (b) the pink curves represent exponential growth with an e-folding distance of 20 km and the gray curves represent exponential growth with an e-folding distance of 30 km.

This supports the idea that the growth of variability in N^2 with altitude is related to the same gravity waves that are responsible for the growth of temperature variability with altitude. This makes sense in that as the wave amplitude (leading to temperature fluctuations) increases by a certain amount, the magnitude of the slope of the wave at its zero crossing (leading to the temperature gradient which dominates in the N^2 calculations) increases by the same factor.

3.5. N^2 Comparisons

It is instructive to compare seasonally averaged N^2 values from this study to N^2 values from other studies. Figure 18a compares winter and summer N^2 profiles from ALO to profiles derived from early rocket-borne temperatures [*Charney and Drazin, 1961*] and to results from Na lidar observations [*Zhao et al., 2003*]. At 45 km, the rocket values of N^2 are approximately 30% greater than those from ALO. Assuming good temperature measurements, this could reflect a higher stratopause in the rocket measurements, which would lead to lower temperatures and a more positive temperature gradient. In both cases, the winter values are bigger than the summer values. Both sets of values decrease with increasing altitude, creating minima within the next 25 km, and then increase with altitude. However, significant differences exist. The ALO values have structure between 63 and 76 km in winter and between 70 and 80 km in summer. As discussed earlier, this structure probably reflects the presence of inversion layers. They are possibly missing from the rocket data because of timing or latitude. The effect of this structure is to change the altitudes of the minima and the values of the minima. Above the minima, all the curves come together between about 74 and 79 km. However, the ALO

summer and winter values cross at 74 km, with the winter N^2 values becoming smaller. In contrast above 78 km the rocket winter values of N^2 again become bigger than the summer values, and they are significantly greater than the ALO winter values. This would imply a temperature structure in the winter data with a more positive gradient than in summer or in the ALO data.

The Na lidar values overlap in altitude with the ALO values between 80 and 90 km, but the values and altitude variation are very different. The Na lidar values near 80 km are much smaller than the ALO values; near 88 km they are significantly bigger. At 80 km the winter Na values are bigger than the summer values, only becoming smaller above 85 km. This cross over occurs 10 km higher than for ALO.

Several things may contribute to these differences. Higher altitude inversion layers or large oscillations could cause both the small and large values. These values would be accentuated by the smaller altitude resolution, 500 m instead of 3 km, and the shorter integration times, 15 minutes instead of all night. As indicated earlier, the ALO data shows more periods with small or negative N^2 when the integration time is shortened. Presumably the same is true for the altitude interval. The other significant difference between the two data sets is that the Na lidar data are integrated over fewer nights. More nights would usually reduce the extreme values. Another potential difference is that the Na lidar results were obtained at a latitude approximate 7°S of ALO. That might affect the occurrence of inversion layers and additional oscillations at higher and lower altitudes that seem to accompany them. We also compare the ALO results with the corresponding results obtained from the NRL-MSISe00 model for the ALO location. Figure 18b shows that they behave similarly in both winter and summer. In particular, the

winter N^2 values are greater than the summer values below about 75 km and the summer values are greater than the winter values above that. Even the values are fairly similar. However, there are some differences. Mostly, there is considerably more structure in the ALO profiles than in the model profiles. This is very apparent in winter between 63 and 76 km and in summer between 70 and 80 km. As commented on earlier, this structure at ALO arises from the change in the temperature gradient on the bottom side and topside of inversion layers. Because of much greater real and effective smoothing in altitude and time, the model does not show inversion layers. In addition, the ALO N^2 values above 76 km tend to be larger than the model values. This probably arises because the model has

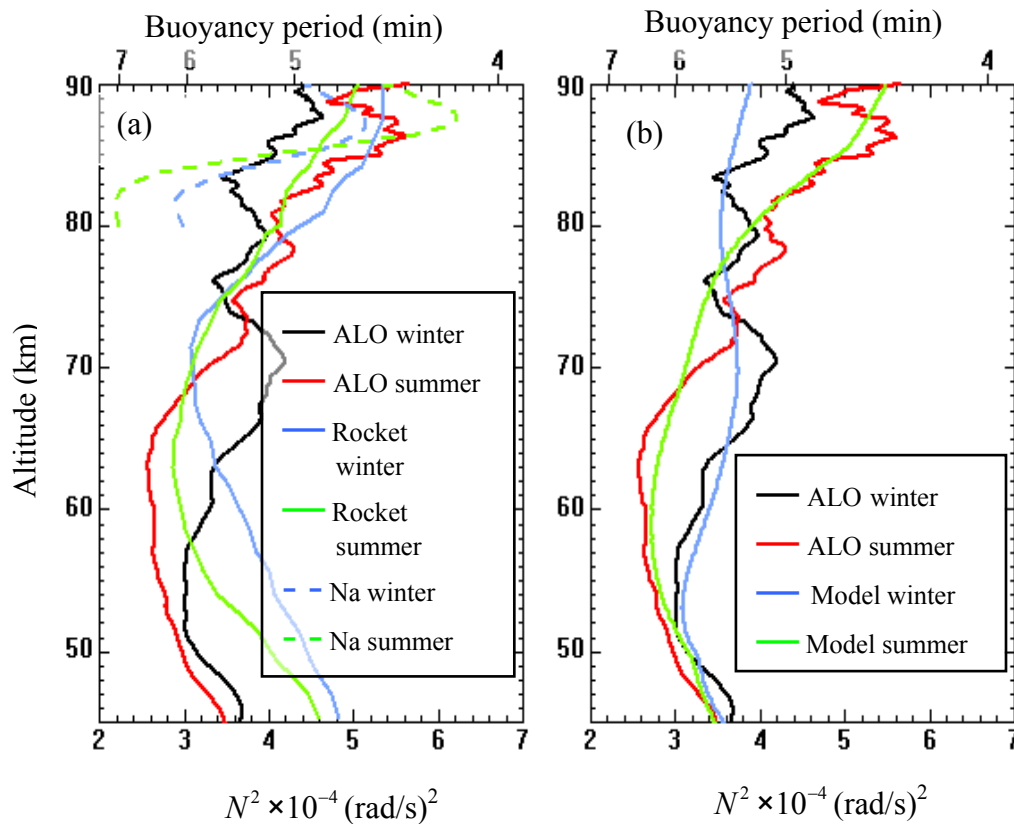


Figure 18. Comparison of winter and summer N^2 profiles from several sources. (a) Comparison of ALO, Na lidar, and rocket results. (b) Comparison of ALO and NRL-MSISE00 model results.

lower temperatures in the upper mesosphere, hence more negative gradients than the ALO temperature climatology [Herron and Wickwar, 2009b].

To examine the differences better between N^2 derived from the observations and the model, we created an N^2 climatology from the model, Figure 19, to compare with the lidar climatology in Figure 13. Profiles were calculated for the days corresponding to the 150 days in the data set and then averaged over 31 day to create the composite year. Several standouts in the comparison. Much higher values ($9.0 \times 10^{-4}(\text{rad/s})^2$) were observed in the data in summer above 85 km than in the model ($5.4 \times 10^{-4}(\text{rad/s})^2$). The summer maximum at 90 km in the data occurs a month earlier than in the model. More structures

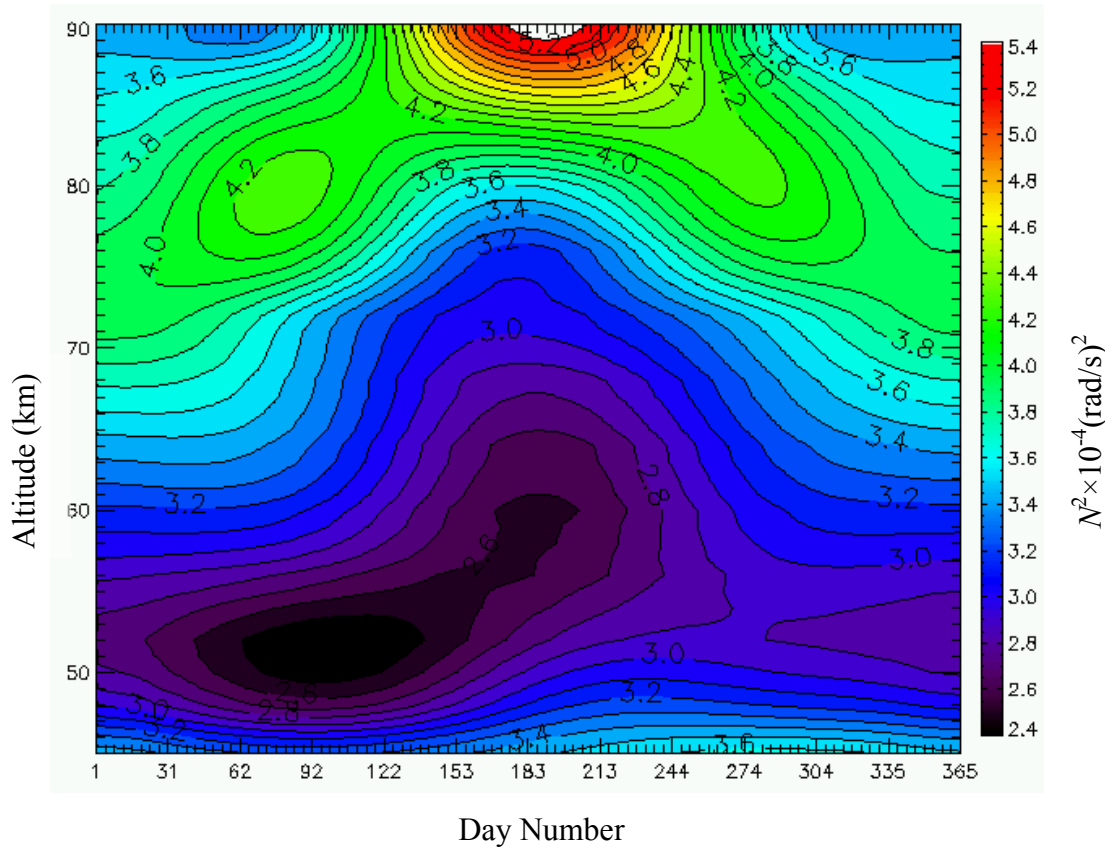


Figure 19. N^2 climatology derived from NRL-MSISe00 model temperatures. Each profile is the result of a 31-day average of nights that extend above 90 km.

occur in the data than in the model. The smallest N^2 values occur in the model over 10 km lower and a month earlier than in the data. Phase propagations are very different. There is upward phase progression in the model between January and June, followed by a downward phase progression between July and December. There is a clear annual variation in the model below 75 km, whereas the lidar data are more dominated by a semi-annual variation. Only above 75 km does the model show a small semi-annual variation.

4. Summary and Conclusions

Nighttime, average temperature profiles and their temperature gradients obtained using a Rayleigh lidar at ALO from late 1993 through 2004 and extending in altitude up to at least 90 km were used to determine the Brunt-Väsälä frequency squared N^2 throughout the mesosphere from 45 to 90 km. Individual profiles of N^2 look very similar to the profiles of $\partial T/\partial z$. The N^2 climatology presented in Figure 13 is for a composite year obtained using these 150 nighttime N^2 profiles averaged over a 31-day window spanning 11 years centered on each day. In structure it is very similar to the $\partial T/\partial z$ climatology presented in Figure 11. We believe this is the first N^2 climatology covering the entire mesosphere. Significant results are summarized below:

- The minimum and maximum values of N^2 over the entire mesosphere vary between $2.2 \times 10^{-4} \text{ (rad/s)}^2$ and $9.0 \times 10^{-4} \text{ (rad/s)}^2$, respectively. The corresponding buoyancy periods vary between 7.0 minutes and 3.5 minutes.

- For these highly averaged climatological values (Figure 13), N^2 is greater than zero implying that the mesosphere is convectively stable. However, all-night and hourly profiles (see Chapter 7) do show many occurrences of $N^2 < 0$.
- We found a clear seasonal variation in N^2 profiles with up to 30% larger values during winter than summer below 75 km and larger values during summer than winter above 75 km. This reversal agrees well with a downward phase progression in the annual and semi-annual variations of N^2 .
- Structures in the temperature profiles, particularly inversion layers and waves, lead to significant structure in the N^2 profiles.
- Above about 60 km, in the region where dynamics dominates over radiation, the amplitudes of the annual and semi-annual oscillations are most pronounced. This correspondence suggests a relationship between these oscillations and the overall dynamics in the upper mesosphere. Furthermore, their different downward phase variations suggest different causes.
- The geophysical variability in N^2 grows rapidly with altitude. Because it grows exponentially with the same e-folding distances as the geophysical variability in temperature, we deduce that the N^2 variability arises from the growth of gravity waves with altitude.

In addition to the results from the N^2 climatology and seasonal profiles, the N^2 values were compared to existing values from other sources and a climatology derived from the NRL-MSISe00 empirical temperature model. Some of the results are summarized below:

- As with shorter integration times for Rayleigh observations, the higher time and spatial resolution for Na lidar determinations show both smaller and larger N^2 values in the altitude of overlap.
- The most extensive comparison is with N^2 values derived from the NRL-MSIS00 empirical model. The basic values are similar, but structures in time and altitude are very different.
- Although there is a clear annual oscillation in the N^2 climatology derived from the NRL-MSIS00 model, the semi-annual oscillation and many of the structures are not accounted for. These differences are large because N^2 depends strongly on dT/dz , which varies little in the model.

In conclusion, we have presented a mid-latitude, mesospheric, N^2 climatology based on extensive temperature measurements. This climatology is most applicable to situations involving the average behavior of the mid-latitude mesosphere over the period of a day or longer. It does not apply to short time periods of the order of minutes to hours when convective instabilities, i.e., when $N^2 \leq 0$, may exist. We also found significant differences between our N^2 climatology and values calculated from the NRL-MSIS00 model atmosphere, the widely used empirical model. These differences arise because of the combination of sensitivity of the N^2 calculation to the temperature gradient and a lack of structure in the model, especially structure from inversion layers, the annual oscillation, and, the semiannual oscillation.

CHAPTER 5

CHARACTERISTICS OF MONOCHROMATIC GRAVITY WAVES

IN THE MESOSPHERE OBSERVED BY RAYLEIGH LIDAR

ABOVE LOGAN, UTAH

Abstract

Atmospheric gravity wave characteristics were examined by using the Rayleigh lidar data collected over a period spanning 11 years above Logan, UT (41.7°N, 111.8°W), over an altitude range from 45 to 90 km. Variations of the relative density perturbations obtained with 3-km vertical resolution and 1-hour temporal resolution are used to identify the presence of monochromatic gravity wave features throughout the mesosphere. The measured vertical wavelengths λ_z ranged from 6 to 19 km with 12 to 16 km the most prevalent and the measured vertical phase velocities c_z ranged from 0.2 to 1 m/s (0.70 to 3.6 km/hr) with 0.5 to 0.6 m/s (2.0 to 2.2 km/hr) the most prevalent. These values of λ_z and c_z were used to infer wave periods τ , horizontal wavelengths λ_x , horizontal phase velocities c_x , and horizontal distances to the source region X . The values of deduced τ ranged from 2 to 19 hours with 6 to 8 hours in winter and 4 to 6 hours in summer the most prevalent. The λ_x values ranged from 160 to 3000 km with 550 to 950 km the most prevalent. Deduced values of c_x ranged from 24 to 53 m/s (85 to 190 km/hr) with 32 to 35 m/s (120 to 130 km/hr) the most prevalent. The values of X ranged from 1,000 km to 7,000 km for waves at 45 km with 2500 to 3500 km the most prevalent and double these values for waves at 90 km. The source of these AGWs is, thus, far from USU. Furthermore for one of these monochromatic waves to exist all night

or appear to extend from 45 to 90 km, it has to originate from a very extended region and persist for a long time. There appears to be a seasonal dependence in c_z , τ , λ_x , and X but not in λ_z and a minimal dependence in c_x . The vertical phase velocities maximized in summer whereas the apparent periods, horizontal wavelengths, and horizontal distance to the source region maximized in winter. Moreover, because background vertical winds are extremely small, the measured c_z is a very good approximation to the intrinsic vertical velocity and by its derivation c_x is therefore a very good approximation to the intrinsic horizontal velocity.

1. Introduction

Theoretical studies suggest that AGWs play a major role in determining the structure and large-scale circulation of the middle atmosphere [Lindzen, 1981; Matsuno, 1982; Geller, 1983]. These waves are believed to originate in the troposphere, the most often suggested sources being orography [Nastrom and Fritts, 1992], convective storms [Alexander et al., 1995; Fritts and Alexander, 2003], and the jet stream [Fritts and Nastrom, 1992]. These waves propagate horizontally and vertically. The upward propagation of gravity waves generated at lower altitudes provides a significant coupling between different regions of the atmosphere. As these waves propagate upward conservation of energy per unit mass arguments say that the wave amplitude will grow by a factor of e every 2-scale heights H . However, this upward motion and energy growth is not always unimpeded. The propagation of AGWs to higher altitudes is significantly affected when their intrinsic horizontal phase speed, i.e., the horizontal phase speed of the wave relative to the mean flow, equals the prevailing background wind in the

atmospheric region through which they propagate. This is a critical level [*Lindzen*, 1981]. At this level the upward motion and energy growth cease, and the energy and momentum are absorbed into the mean wind. In addition, the growth in wave amplitude will also be significantly reduced when a wave enters a region with convective or dynamic turbulence [*Lindzen*, 1981]. Furthermore, under some conditions the wave is continuously losing small amounts of energy and momentum to the surrounding atmosphere as it propagates upward.

The atmospheric density and temperature profiles are expected to present wave-like structures due to gravity wave perturbations. Their characteristics have been calculated by means of perturbation theory [*Hines*, 1960] and have been observed by a variety of techniques. Those techniques include direct measurements from rocket experiments [e.g. *Hirota*, 1984; *Hirota and Niki*, 1985], radar observations of falling spheres [*Eckermann and Vincent*, 1989], and lidar measurements of Rayleigh backscatter [*Chanin and Hauchecorne*, 1981; *Shibata et al.*, 1986; *Miller et al.*, 1987; *Gardner et al.*, 1989; *Mitchell et al.*, 1991; *Wilson et al.*, 1991a; *Collins et al.*, 1996; *McDonald et al.*, 1998; *Rauthe et al.*, 2006]. The density and temperature profiles measured by a Rayleigh lidar are precise enough to describe density (or temperature) fluctuations caused by atmospheric gravity waves. Thus, the Rayleigh lidar is a very powerful method to observe wave structures in the middle atmosphere [*Hauchecorne and Chanin*, 1980, 1983; *Shibata et al.*, 1986].

Of the techniques capable of measuring gravity-wave parameters at middle-atmosphere heights, only Rayleigh lidar can provide successive profiles that cover the entire mesosphere for periods of several hours. Lidar studies of gravity wave activity

often concentrate on observations of monochromatic structures, because they appear clearly in almost all lidar profiles. Several lidar results on gravity waves have been published, but most of them cover only a rather small altitude region or have observations over periods of only a few days or months. None of them have extensive observations that cover the entire mesospheric region, a very crucial region as this is where much gravity wave dissipation is believed to occur. This paper presents a comprehensive report on the characteristics of monochromatic gravity waves derived from Rayleigh lidar measurements between 45 and 90 km made on 150 nights at the ALO, located on the USU campus (41°N 111°W), over an 11-year period.

The observations and derivation of gravity wave parameters from the lidar data are presented in section 2, results of the analysis are given in section 3, the results are discussed in section 4, and the summary and conclusions are presented in section 5.

2. Observations and the Derivation of Gravity Wave Parameters

2.1. Observations

The Rayleigh-scatter lidar system is part of the ALO at the Center for Atmospheric and Space Sciences, on the USU campus in Logan, UT (41.74° N, 111.81° W and 1.47 km above sea level). It has been operated since late 1993, giving rise to an extensive database of nighttime mesospheric profiles of relative densities and absolute temperatures. The ALO Rayleigh lidar is a vertically pointing, coaxial system. It consists of a frequency-doubled Nd:YAG laser operating at 30 Hz generating 18–24 watts at 532 nm and having a 44-cm diameter Newtonian telescope. The signals from below ~18 km are blocked by a mechanical chopper and the gain is reduced by almost 10^3 by an

electronic gate for altitudes below 38 km, leading to good data from 45 km to ~90 km. A narrow-band interference filter (1 nm) is used to remove most of the background light from stars, moon, airglow and scattered city lights. The single, gated detector is a green-sensitive, bialkali photomultiplier tube (Electron Tubes 9954B) in a Peltier-cooled housing. A more extensive description of this system is given by *Beissner* [1997], *Wickwar et al.* [2001], *Herron* [2004, 2007] and *Herron and Wickwar* [2009a].

In total more than 900 nights of observations were collected during the 11-year period, resulting in approximately 5000 hours of data. Of these profiles, 150 (1214 hours of data for an average of 8.1 hours per night) from this 11-year period extend to 90 km or above and they are the ones used in this study and several others. A histogram of the number of nights and hours from each month in a composite year are shown in Figure 20.

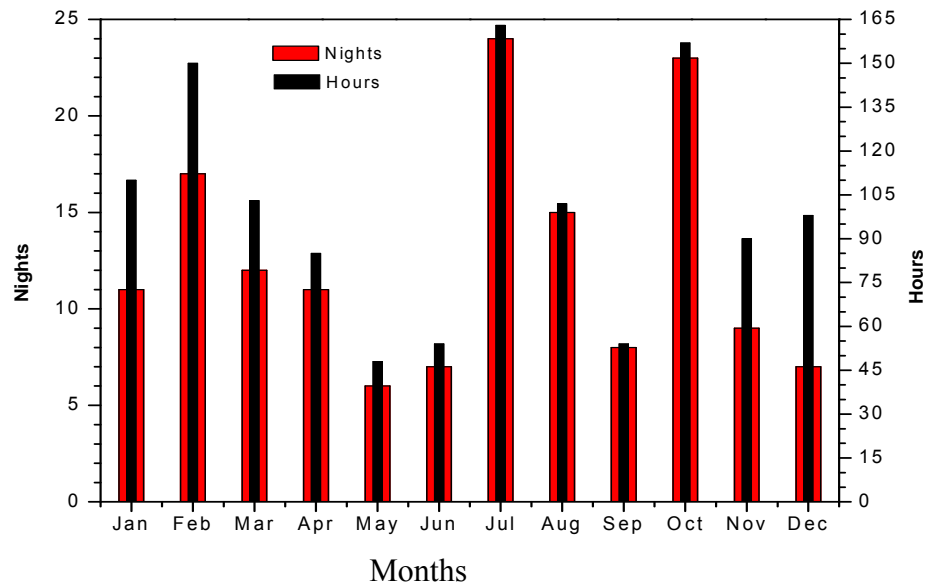


Figure 20. Histogram of the observations made each month over the 11-year period from the 150 nights that reached 90 km. Red bars indicate the number of nights and black bars indicate the number of hours.

The data on these clear nights were collected continuously for periods of 4 to 12 hours. The recorded raw data is in the form of photon count profiles with an altitude resolution of 300 m (3600 laser pulses) from the ground to 500 km. The data of interest for this study start at 45 km. At each altitude(z), the observed photon counts are the sum of a background signal (from the detector, moon, starlight, airglow, and scattered city lights) and the signal of interest from the backscattered laser pulses. The background signal is determined between 120 and 180 km and subtracted from the total. This remaining signal, multiplied by the square of the range from the laser, is proportional to the mass density of the atmosphere $\rho(z)$, assuming constant mean-molecular mass m in the portion of the atmosphere we are interested in. However, the constant of proportionality may vary from one two-minute profile to the next because of changes in the atmosphere's transmittance or because of variations in the laser's power. To reduce the influence of signal fluctuations caused by these effects, we normalized the profiles to unity at 45 km. Before normalizing the profiles to unity, the data are averaged over 3 km (81 sampling intervals) and 1 hour. The all-night averaged profiles are obtained by averaging the individual soundings of the atmosphere for the entire night together into a single relative density profile that is normalized to unity at 45 km. Temperatures are determined from these relative densities by using hydrostatic equilibrium and the ideal gas law [Hauchecorne and Chanin, 1980]. The details, as applied to this lidar, are reviewed by Beissner [1997], Wickwar *et al.*, [2001], Herron [2004, 2007] and Herron and Wickwar [2009a].

The individual measured density profile $\rho(z)$ can be represented as $\rho(z) = \rho_0(z) + \rho_1(z)$, where $\rho_1(z)$ is the wave induced perturbation density and $\rho_0(z)$ is the background mean state of the atmosphere (i.e., the unperturbed density profile). The background profile is first obtained by least squares fitting a sixth order polynomial to the logarithm of the nightly averaged density profile. The best method to find $\rho_0(z)$ is not obvious as just about every author has adopted a different method. However, we settled on this method after considerable experimentation that will be reviewed in another paper. The difference of the measured profiles $\rho(z)$ from the fitted background profile $\rho_0(z)$ provides the density perturbation profiles $\rho_1(z)$ and the fractional or relative density perturbation profiles $\frac{\rho_1(z)}{\rho_0(z)}$. The fractional or relative density perturbations are caused by gravity waves in the atmosphere [Hines, 1960]. In addition, tides and planetary waves could contribute to these perturbations, but the larger amplitude ones have longer periods. By normalizing the densities to unity at 45 km we are also minimizing the contribution of tidal components and long-period gravity waves. We treat what remains as being part of the background density. Temporally, $\rho_1(z)$ and $\frac{\rho_1(z)}{\rho_0(z)}$ profiles contain information about waves with periods greater than twice the integration time used for $\rho(z)$. For this paper with a 1-hour integration time that, in principle, means waves with periods longer than 2 hours and shorter than approximately the all-night observing period (i.e., ~4–12 hours). These perturbation profiles are used to derive information about these gravity waves.

2.2. Observed Gravity Wave Parameters

In this section we examine variations in $\rho_1(z)/\rho_0(z)$ profiles to determine general features of the mid-latitude gravity wave field over the altitude range 45-90 km. We do this by examining the monochromatic wave-like perturbations that are found on almost every night. Sometimes they exist for only a few hours, other times for a whole night, up to 10-12 hours. They sometimes become less apparent above ~ 80 km. To illustrate these monochromatic perturbations, profiles of relative density fluctuations at 1-hour intervals are shown in Figures 21a-b and Figure 22 for the nights of January 4, 1995, August 17, 1995, and February 22, 1995, respectively. The fluctuations vary between approximately 1% and 10%. Lines have been drawn on these figures to show the downward phase progression of wave minima or maxima. These solid lines are least squares fits to the corresponding minima or maxima at 1-hour intervals. The average separation between these lines gives λ_z . The vertical phase velocities c_z are then directly measured from the slope of the lines of constant phase in the time-height plots. For each wave, the period τ is calculated from the measured values of λ_z and c_z . Two or more 1-hour profiles that have clear wave structures with a downward phase progression were used to derive λ_z and c_z . On a few nights, the waves were such that the period could be determined directly from the perturbation profiles.

On January 4, 1995, Figure 21a, the sequence of density perturbation profiles shows evidence of a dominant monochromatic wave extending throughout the whole night with a vertical wavelength λ_z of approximately 14 km below about 80 km and a downward phase progression with a vertical phase velocity of $c_z = 0.2$ m/s (0.8 km/hr).

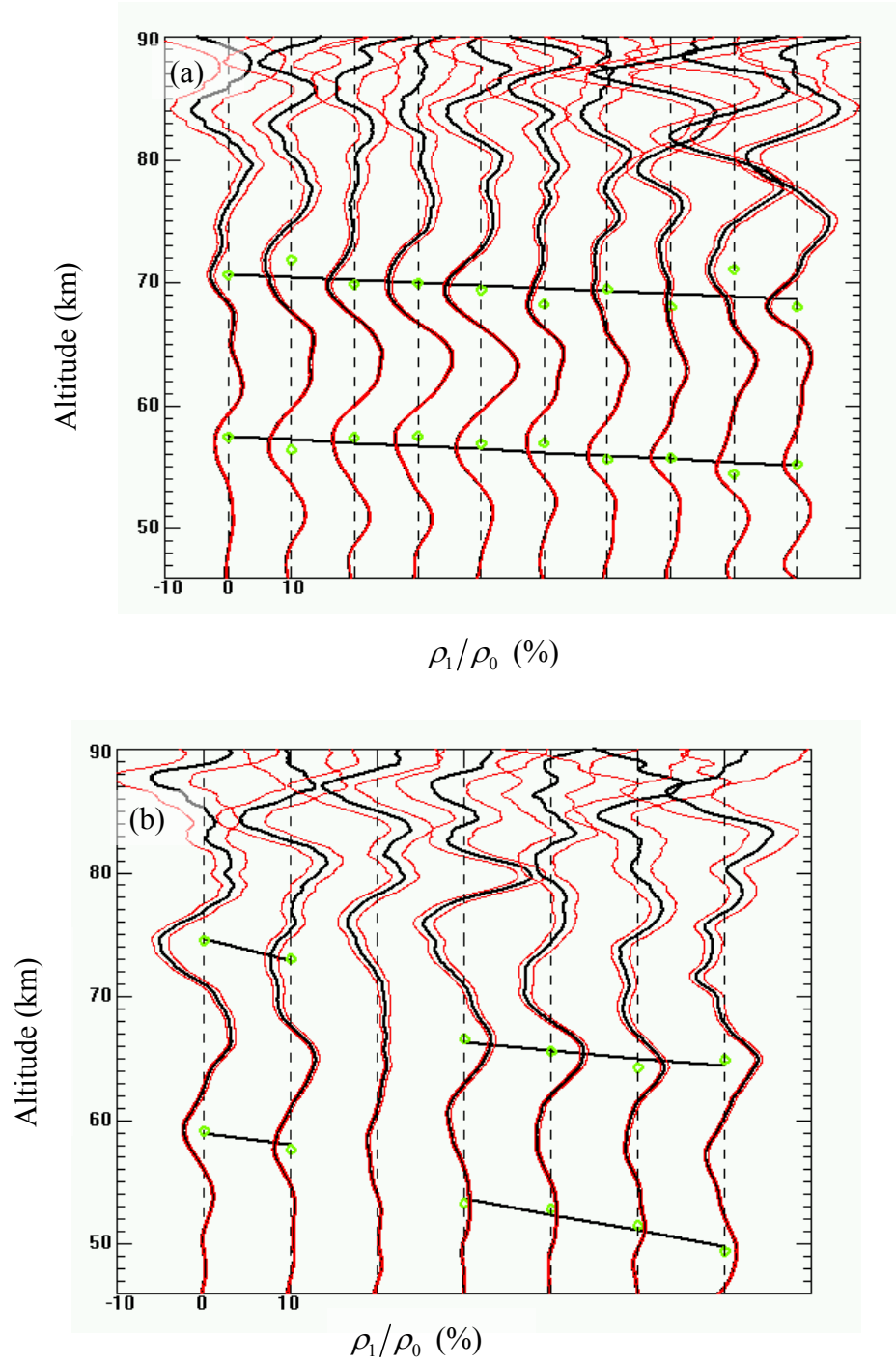


Figure 21. Profiles of relative density perturbations for (a) January 4, 1995 (b) August 17, 1995. Each 1-hour profile is offset by 10%. The measurement uncertainties are shown by red lines. The black straight lines are the least squares fit to the minima, as shown by green dots, in the 1-hour perturbation profiles. The vertical wavelength λ_z and phase velocity c_z are derived from those fits.

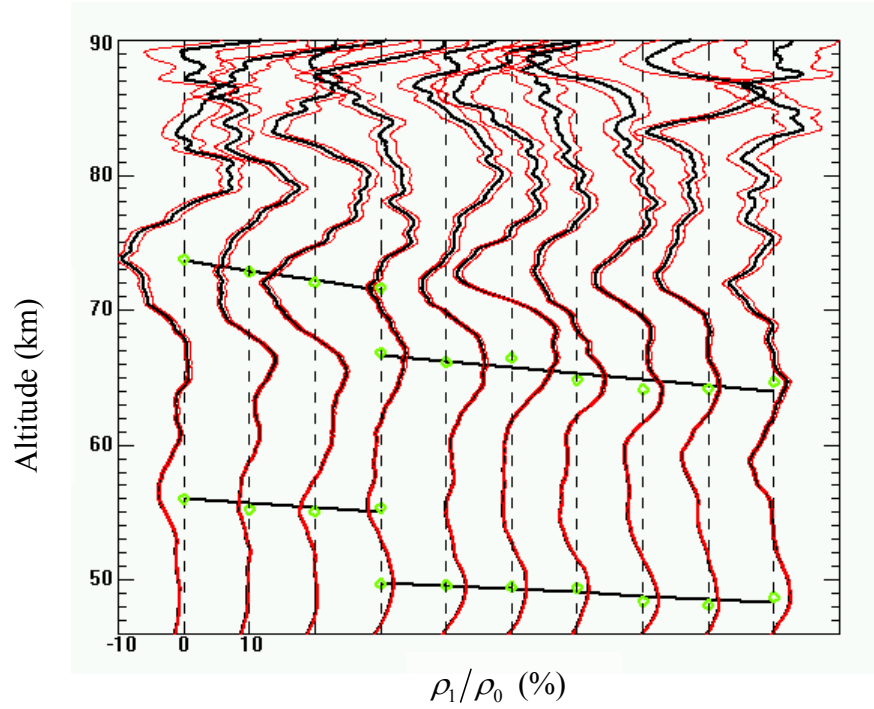


Figure 22. Profiles of relative density perturbations for February 22, 1995. Each 1-hour profile is offset by 10%. The measurement uncertainties are shown by red lines. The black straight lines are the least squares fit to the minima, as shown by green dots, in the 1-hour perturbation profiles. The vertical wavelength λ_z and phase velocity c_z are derived from those fits.

There is also evidence of other smaller amplitude waves that lead to variations in the altitudes of the minima and maxima relative to the least-square fit lines. Above 80 km the pattern becomes more complex. As expected, the perturbations become bigger. But the pattern is less clear. For some hours the perturbation minima are λ_z above the previous minimum. For other, the perturbation is 180° out of phase. In general, the pattern becomes more complex above 80 km.

On August 17, 1995, Figure 21b, the sequence of density perturbation profiles shows clear evidence of monochromatic features for 2 hours with a vertical wavelength, λ_z , near 13 km up to 80 km for the first 2 profiles. The sequence of the last

four profiles also shows evidence of monochromatic features with vertical wavelengths, λ_z , near 13 km up to about 80 km. Above 80 km, there appear to be more waves and the phase progression may be upward or downward. In general, sequences of waves are not as identifiable. Below 80 km, the wave has a downward phase progression with a vertical phase velocity of $c_z = 0.5 \text{ m/s}$ (1.7 km/hr).

On February 22, 1995, Figure 22, the sequence of density perturbation profiles shows evidence of a couple of monochromatic features for most of the night with vertical wavelengths, λ_z , of approximately 17 km below about 80 km and a downward phase progression with vertical phase velocity of $c_z = 0.4 \text{ m/s}$ (1.5 km/hr). Like August 17, 1995 this is a complicated night with multiple waves during the night and smaller amplitude waves superposed on the dominant wave. As on the other two days, the behavior becomes much more complex above 80 km.

All density perturbation profiles for the entire selected dataset of 150 nights over the 11 years have been analyzed individually, in a manner similar to what was done for the three nights in Figures 21 and 22 to determine the λ_z and c_z values for all monochromatic wave features. The analysis differed in that the least square fits were done by eye instead of by a computer calculation. Clear wave-like structures were observed in almost all profiles. Earlier Rayleigh lidar observations at Haute Provence, but in the 30–70 km altitude range, also indicated that wave structures are almost always present in the density profiles obtained with 5- to 60-minute integration periods [*Chanin and Hauchecorne, 1981*].

In this analysis, a downward phase progression was identified in most of the 1-hour consecutive profiles during each of the 150 nights. On a very few nights there were

waves that appeared to have zero or upward phase velocities. A further indication of the unusualness of these nights is that we did not have a continuous distribution of phase velocities below 80 km. With the exception of these very few nights with zero or upward phase velocities, all the other nights has a downward phase velocity with a magnitude greater than 0.2 m/s. Thus these few nights appeared to be unusual and were not considered in this analysis. In the future they may deserve their own special study. For instance, they might represent reflected waves.

Thus, the analysis of the monochromatic gravity waves, which are so obvious in the fractional density perturbation profiles, gives both the vertical wavelength λ_z and downward vertical phase velocity c_z . From these the period for the gravity wave is given by $\tau = \lambda_z / c_z$ and the angular frequency by $\omega = 2\pi / \tau$. These can be combined with the Brunt-Väisälä frequency [Chapter 4] and the AGW dispersion relation to derive the horizontal properties of these AGWs. But first, we have to make an important observation about the derived c_z and ω . Clearly, from their determination, they are observed values. But the important question for the determination of horizontal AGW parameters is whether they are good approximations of the intrinsic values. Jumping ahead, it will be shown that the derived vertical phase velocities are large compared to the background wind speeds [Fauliot *et al.*, 1997], which is reasonable for a horizontally stratified atmosphere. Accordingly, the values of c_z and ω are good approximations of the intrinsic values and therefore the derived horizontal properties will also be good approximations of the intrinsic values.

2.3. Derived Gravity Wave Parameters

For high-frequency waves (i.e., $\hat{\omega} > f$, where $f = 9.5 \times 10^{-5}$ rad/s is the inertial frequency at ALO, corresponding to a period of 18.4 hours, and $\hat{\omega}$ is the intrinsic wave frequency, which we derived from the observations in the previous section), the vertical wavenumber k_z ($k_z = 2\pi/\lambda_z$) is given by the approximate dispersion relation [Walterscheid *et al.*, 1999]

$$k_z^2 = \frac{N^2}{\hat{\omega}^2} k_x^2 - k_x^2 - \frac{1}{4H_p^2}, \quad (5.1.1)$$

where H_p is the scale height, $k_x = 2\pi/\lambda_x$ is the horizontal wavenumber, N is the Brunt-Väisälä frequency or buoyancy frequency, and $\hat{\omega}$ is the observed wave frequency. In this paper, while we use observed parameters rather than the intrinsic parameters, they are very good approximations of the intrinsic values. For gravity waves with midrange frequencies (i.e., $N \approx \hat{\omega} \approx f$), for which $k_z^2 \approx 1/4H_p^2$, the dispersion relation (5.1.1) further simplifies to

$$\hat{\omega} \approx N \frac{k_x}{k_z}. \quad (5.1.2)$$

Using $c_x = \hat{\omega}/k_x$, the intrinsic horizontal phase velocity c_x is very closely approximately

$$\hat{c}_x = \frac{N}{k_z}, \quad (5.1.3)$$

and using the definition of N , k_z , and \hat{c}_x we obtain

$$\hat{c}_x \approx \frac{N}{k_z} \approx \frac{\lambda_z}{\tau_b} \quad (5.1.4)$$

and

$$\lambda_x = \frac{\tau}{\tau_b} \lambda_z, \quad (5.1.5)$$

where, τ_b is the buoyancy period.

Using the dispersion relation (5.1.1) of the atmospheric gravity waves we can also obtain the horizontal distances X traveled by waves seen at altitude Z from the relation [Walterscheid *et al.*, 1999]

$$\frac{Z}{X} = \frac{v_g}{u_g} = -\frac{k_x}{k_z} \frac{k_z^2}{k_z^2 + \frac{1}{4H_p^2}}, \quad (5.1.6)$$

where v_g and u_g are vertical and horizontal group velocities, respectively. (Note: $k_z < 0$ for waves with upward energy transfer, i.e., downward phase progression.)

Furthermore, for upward propagating AGWs for which $k_z^2 \ll 1/4H_p^2$, equation 5.1.6 gives the horizontal source distance as

$$X = \frac{\lambda_x}{\lambda_z} Z. \quad (5.1.7)$$

2.4. Uncertainties in Wave Parameters

While the monochromatic waves are very obvious in the data and, therefore, the wavelength determinations should be very reliable, we would like to confirm the reliability of this technique. We do this by applying Fourier analysis to the density perturbation profiles to find the dominant spatial frequency (and wavelength). This was done for a number of days to see if the results were similar to those obtained from the manual analysis used for most of this work. Very similar wavelengths were found. Examples of the all-night mean vertical wavenumber spectra for January 04, 1995,

August 17, 1995, and February 22, 1995 are shown in Figures 23a-b, and Figure 24, respectively. Because of the 3-km data averaging, they are valid for wavelengths greater than 6 km. The 6-km boundaries are shown by thin black solid lines.

On January 04, 1995, a vertical wavelength of 14 km is found in agreement with the result found in Figure 21a by examining the wave minima. On August 17, 1995, a vertical wavelength of 13 km is found in agreement with the result found in Figure 21b by examining the wave minima. Similarly, on February 22, 1995, a vertical wavelength of 17 km is found in agreement with the results found in Figure 22. This is particularly reassuring because the data in Figure 21b had to be examined in two segments. This good agreement arises because the waves are so truly monochromatic.

Having verified the determination of λ_z , we need to determine its uncertainty. The approach is to find λ_{zi} for each of the 1-hour density perturbation profiles for a night, and then to find the mean vertical wavelength $\bar{\lambda}_z$ that was identified from Fourier analysis (Figures 23 and 24), standard deviation σ_{λ_z} , and standard deviation of the mean $\sigma_{\bar{\lambda}_z}$. The last quantity provides a good estimate of the uncertainty for the nighttime value of λ_z . The uncertainty of $\bar{\lambda}_z$ i.e., $\sigma_{\bar{\lambda}_z}$ was calculated as

$$\sigma_{\lambda_z} = \sqrt{\frac{1}{(N_p - 1)} \sum_{i=1}^{N_p} (\lambda_{zi} - \bar{\lambda}_z)^2} \quad (5.1.8a)$$

$$\sigma_{\bar{\lambda}_z} = \frac{\sigma_{\lambda_z}}{\sqrt{N_p}}, \quad (5.1.8b)$$

where N_p is the number of profiles, λ_{zi} is wavelength of the i^{th} individual 1-hour profile.

The uncertainty in λ_z was calculated for a number of days and the values for the three days that have been used as examples (January 4, 1995, February 22, 1995, and August 17, 1995) are given in Table 3. Also given in Table 3 are the actual values (inside braces)

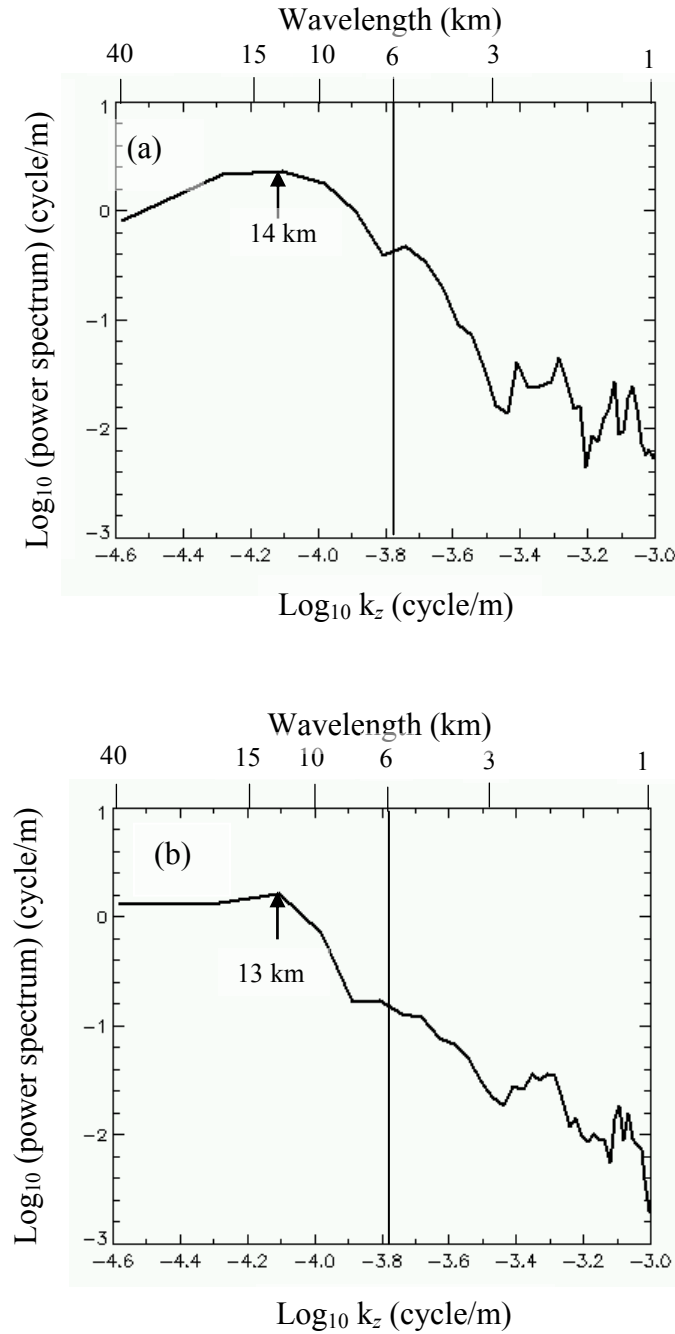


Figure 23. All-night average vertical wavenumber spectrum for: (a) January 04, 1995, (b) August 17, 1995. The data used come from the 45-80 km altitude range. Thin black lines correspond to 6 km vertical wavelengths.

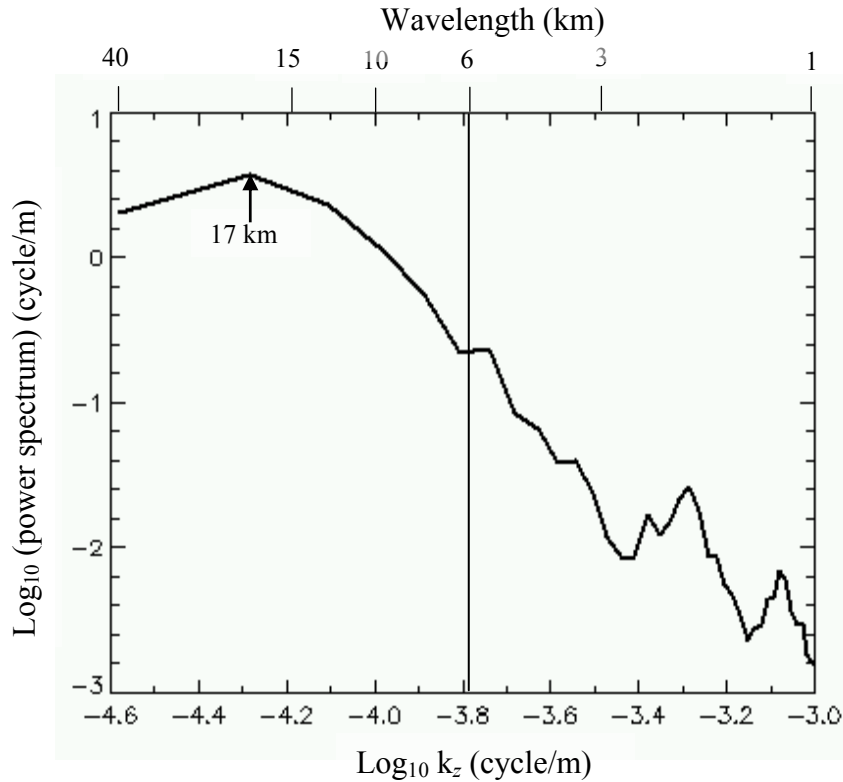


Figure 24. All-night average vertical wavenumber spectrum for February 22, 1995. The data used come from the 45-80 km altitude range. Thin black lines correspond to 6 km vertical wavelengths.

and the percentage uncertainties (inside parenthesis). These three examples had long nights. For shorter nights, the uncertainty increased, as would be expected, inversely in proportion to the square root of the number of 1-hour profiles. Thus in decreasing from 12 hours to 3 hours, the uncertainty would double.

The uncertainty in the vertical phase velocity is then calculated from the uncertainty in the distance traveled in time t . More specifically, using the linear, least-squares fit to the minima or maxima, the descent speed is simply the slope m and the uncertainty in the descent speed is derived from the uncertainty in m , i.e., from σ_m , which is taken from the IDL linear fit routine. As for the vertical wavelength, values of the uncertainty in c_z in

absolute and percentage terms along with the actual c_z values are tabulated in Table 3 for the three example days.

These uncertainties in λ_z and c_z are then propagated to determine the uncertainties in τ , c_x , λ_x and X at 45 km. In doing so, no uncertainty was associated with τ_b . The results are tabulated in Table 3.

Table 3. Examples of Uncertainties Calculated for Different Gravity Wave Parameters^{*}

Date	σ_{λ_z} (km)	σ_{c_z} (km/h)	σ_{τ} (hours)	σ_{λ_x} (km)	σ_{c_x} (km/h)	σ_X (km)
Jan 04, 1995	0.65 {14} (4.6%)	0.01 {0.81} (1.3%)	0.85 {17} (5.0%)	150 {2200} (6.8%)	6.0 {130} (4.6%)	580 {7000} (8.3%)
Feb 22, 1995	0.72 {17} (4.2%)	0.02 {1.5} (1.4%)	0.50 {11} (4.5%)	110 {1700} (6.2%)	6.6 {160} (4.2%)	340 {4500} (7.6%)
Aug 17, 1995	0.50 {13} (3.8%)	0.03 {1.7} (1.8%)	0.31 {8.0} (3.9%)	52 {960} (5.4%)	4.6 {120} (3.8%)	220 {3300} (6.7%)

^{*}Actual values are given inside the braces and the corresponding percentage uncertainties are given inside the parenthesis.

3. Results of the Analysis

The measured vertical wavelengths ranged from 6 km to 19 km between 45 and 70-80 km altitude. The relative perturbation amplitudes increased with altitude, e.g., from about 2% in the lowest region (45-60 km) on February 22, 1995 to about 8% in the highest region (60-90 km). However, the observed amplitudes for the all-night averaged density perturbation profiles for all 150 nights used in this study vary between about 0.5% in the lowest part to about 9% in the highest part. As noted previously, above 80 km the clarity of the monochromatic wave-like features is reduced. *Mitchell et al.* [1991] also observed this and suggested that the reduction in clarity might come from the decrease in precision of individual perturbation profiles with increasing height. However, in the

present case as seen in Figures 21a–b and Figure 22, the measurement uncertainties in the perturbation profiles at 80 km are smaller than the perturbation amplitudes of 7–9% implying that the reduction in clarity of the wave-like features is probably due to geophysical causes.

3.1. Seasonal Variation of Gravity Wave Parameters

The measured and calculated AGW parameters for all nights are plotted versus time during a composite year in Figures 25a–f. Each set of points is also fitted with a constant and an annual sinusoid, which is shown as a solid line. No seasonal trend is evident in vertical wavelengths (Figure 25a) and the values are highly variable. Variations in vertical phase speed c_z with time are shown in Figure 25b. A clear seasonal trend is observed with a faster speed in summer and a slower speed in winter. The observed vertical phase speeds range from 0.2 to 1.0 m/s (0.72 km/hr to 3.5 km/hr). Values of the observed AGW period, τ , ranged from 2–18 hours. The seasonal variation of τ , given in Figure 25c, shows longer periods in winter months than in summer months. The values and seasonal variation of the horizontal wavelengths λ_x are shown in Figure 25d. There is a seasonal trend with longer values in winter than in summer. The observed horizontal phase velocities, c_x , are shown in Figure 25e. Previous researchers used a constant value for τ_b to calculate c_x [e.g., *Gardner et al.*, 1989; *Rauthe et al.*, 2006]. But we used a seasonal seasonal variation in τ_b to calculate c_x . Profiles of the seasonally averaged τ_b derived in Chapter 4 are shown in Figure 26. These values are further averaged between 55 and 70 km, the approximate region from which most of the λ_z and c_z values were found, for each season separately. Although λ_z has little if any seasonal

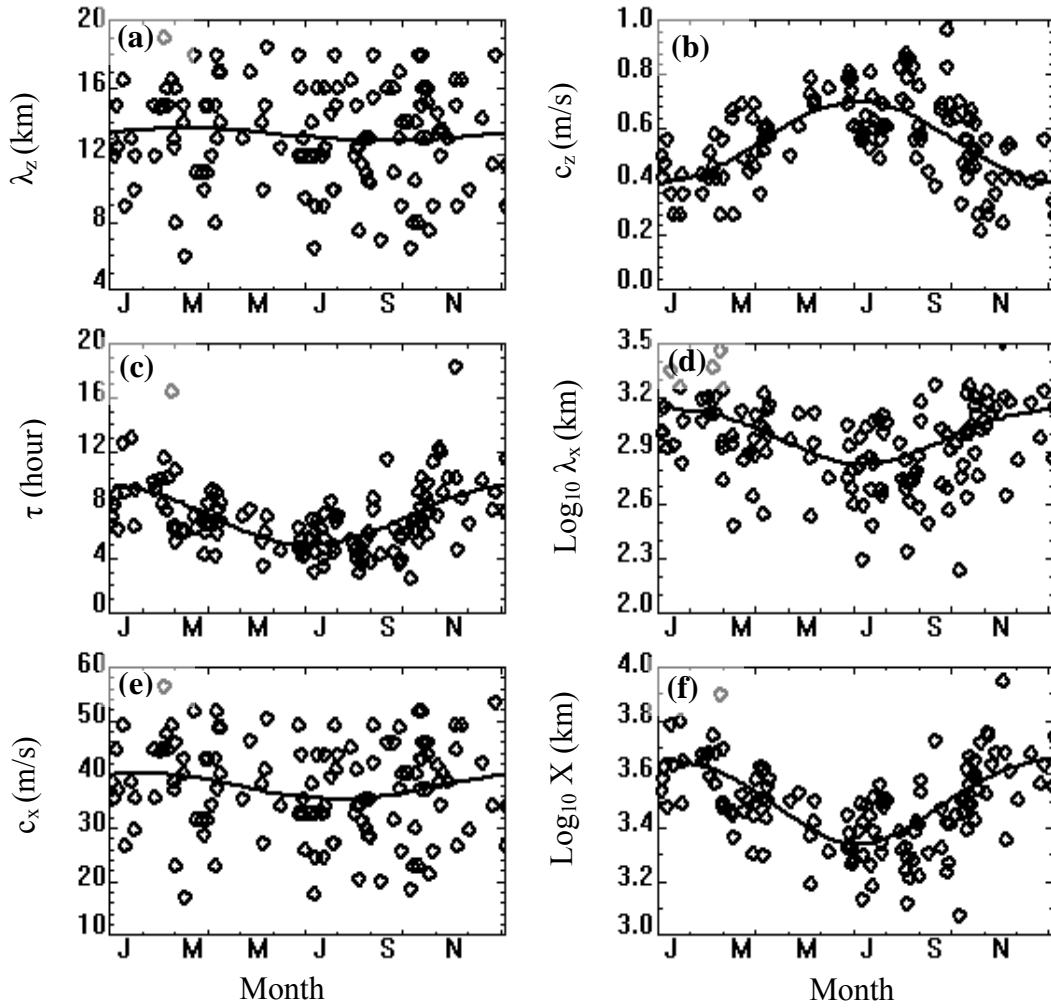


Figure 25. Seasonal variations in gravity wave parameters. (a) Observed vertical wavelengths. (b) Observed vertical phase velocities. (c) Deduced periods. (d) Log of the deduced horizontal wavelengths. (e) Deduced horizontal phase velocities. (f) Log of the deduced horizontal distance to the source region at 45 km. Solid curves are the least squares fit of a constant and an annual sinusoid.

variation, τ_b is enough bigger in summer than in winter that the c_x values are bigger in winter than in summer. The seasonal variation in estimated horizontal distance X to the source region is given in Figure 25f for waves observed at 45 km. A clear seasonal trend in X is seen with larger values in winter than in summer.

The day-to-day variation in all parameters in Figure 25 is very large. As seen in Table 2, the uncertainties in the parameters vary from 3–8%, whereas the variations

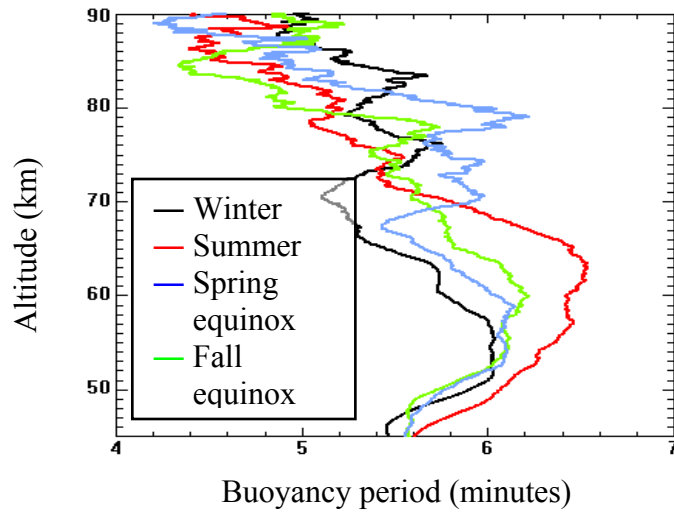


Figure 26. Seasonal variation of buoyancy period.

shown in Figure 25 are much larger. This implies that the large day-to-day variations are real and dominated by geophysical contributions.

3.2. Distribution of Gravity Wave Parameters

Figures 27-31 show frequency plots of the gravity wave parameters from which characteristic values and the spread in values can be determined. A histogram or frequency plot depicting the number of observed waves versus vertical wavelength is shown in Figure 27. The range is from 6 to 19 km, with the most common vertical wavelengths between 12 and 16 km. The frequency falls off more sharply for longer wavelengths than for shorter ones. As seen in Figure 25b, there is a clear seasonal variation in c_z that affects almost all the other parameters. To examine this more closely, we separately analyzed c_z values for winter (November, December, January, February, March, and April) and summer (May, June, July, August, September, and October). A frequency plot depicting the values of observed vertical phase velocities c_z during winter

and summer are shown in Figure 28a and 28b, respectively. The values of c_z range from 0.2 m/s (0.8 km/hr) to 1 m/s (3.6 km/hr) with the most prevalent values 0.5 m/s (1.8 km/hr) in winter and between 0.6 m/s (2 km/hr) in summer.

Wave periods are also separately analyzed for winter and summer. The calculated wave periods (τ) range from 2 hours to 18 hours with the most prevalent wave period near 6 hours. However, the wave periods are significantly shorter in summer than in winter. The maximum period calculated, 18 hours, is very close to the inertial period

$$\left(\frac{2\pi}{f} = \frac{2\pi}{9.50 \times 10^{-5}} = 6.47 \times 10^4 s = 18.0 \text{ hours}\right) \text{ at ALO, the longest period that can be}$$

supported. The calculated periods are shown in a frequency plot in Figures 29a-b. The minimum period that can be observed is a function of the time resolution of the data. The 1-hour integration time used limits the observed periods to 2 hours or longer. A shorter integration time could be used in the data reduction, but appears to be unnecessary because the dominant period is significantly greater than 2 hours.

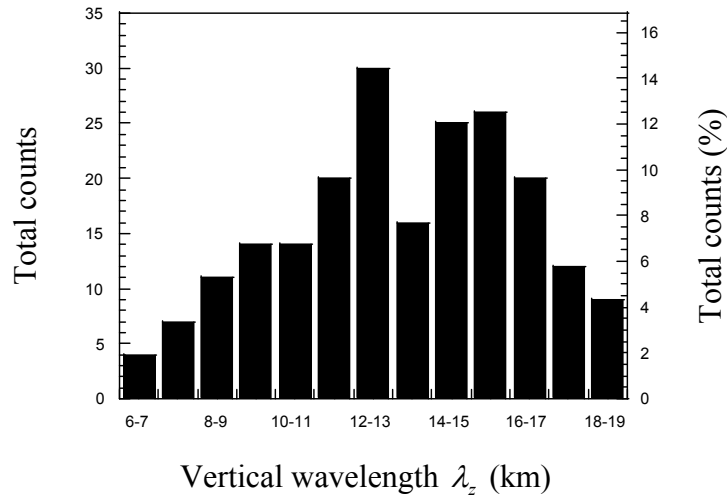


Figure 27. Histogram of gravity wave vertical wavelengths.

However, this is something that could be tried in the future to see if there is another distribution of AGWs with shorter periods. Frequency plot of the horizontal phase velocities c_x and horizontal wavelengths λ_x are shown in Figures 30a and 30b. The

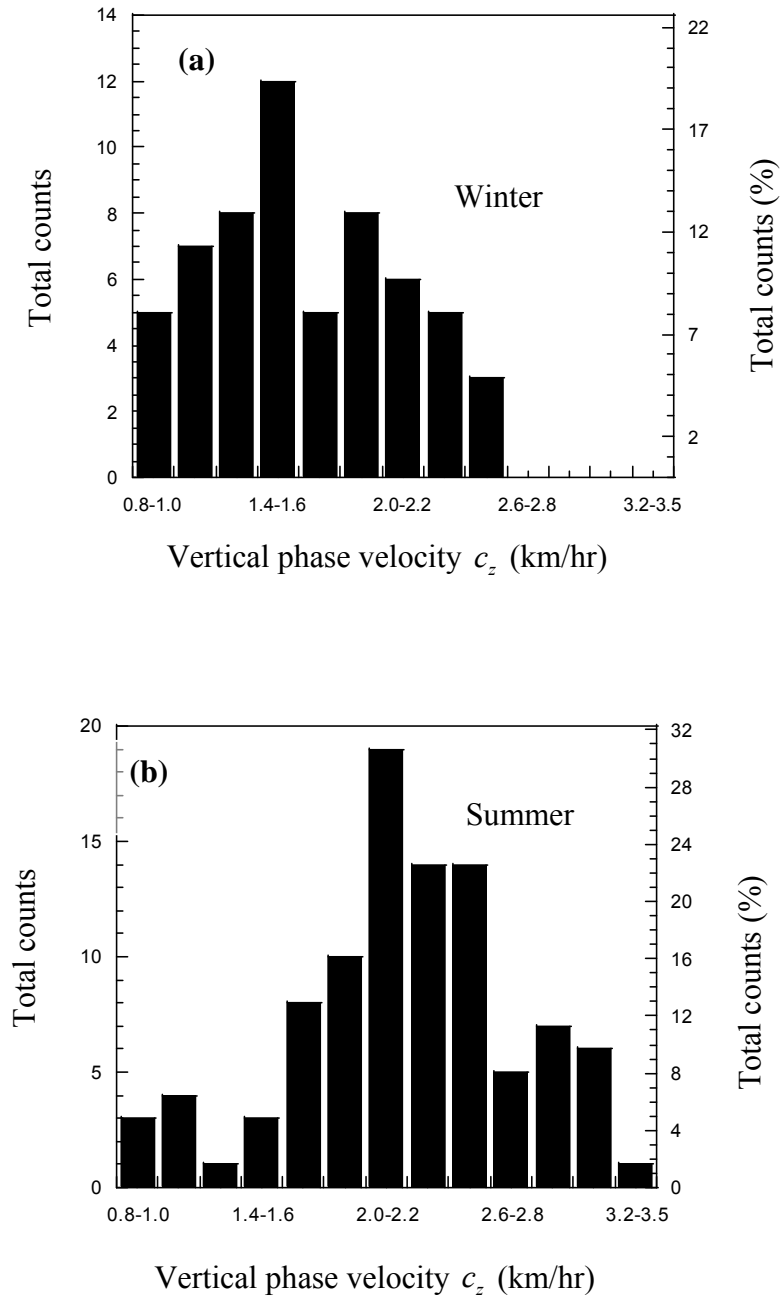


Figure 28. Histograms of gravity wave vertical phase velocities for (a) winter and (b) summer.

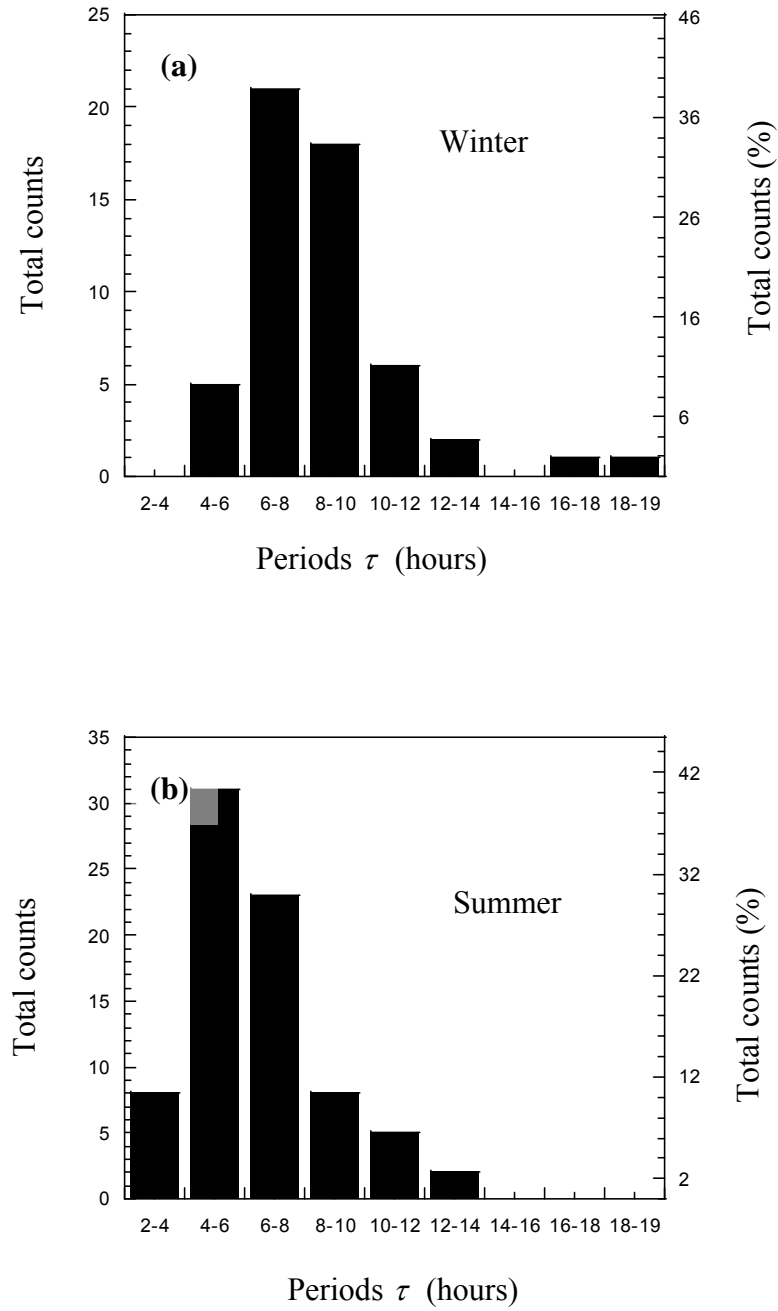


Figure 29. Histograms of deduced gravity wave periods for (a) winter and (b) summer.

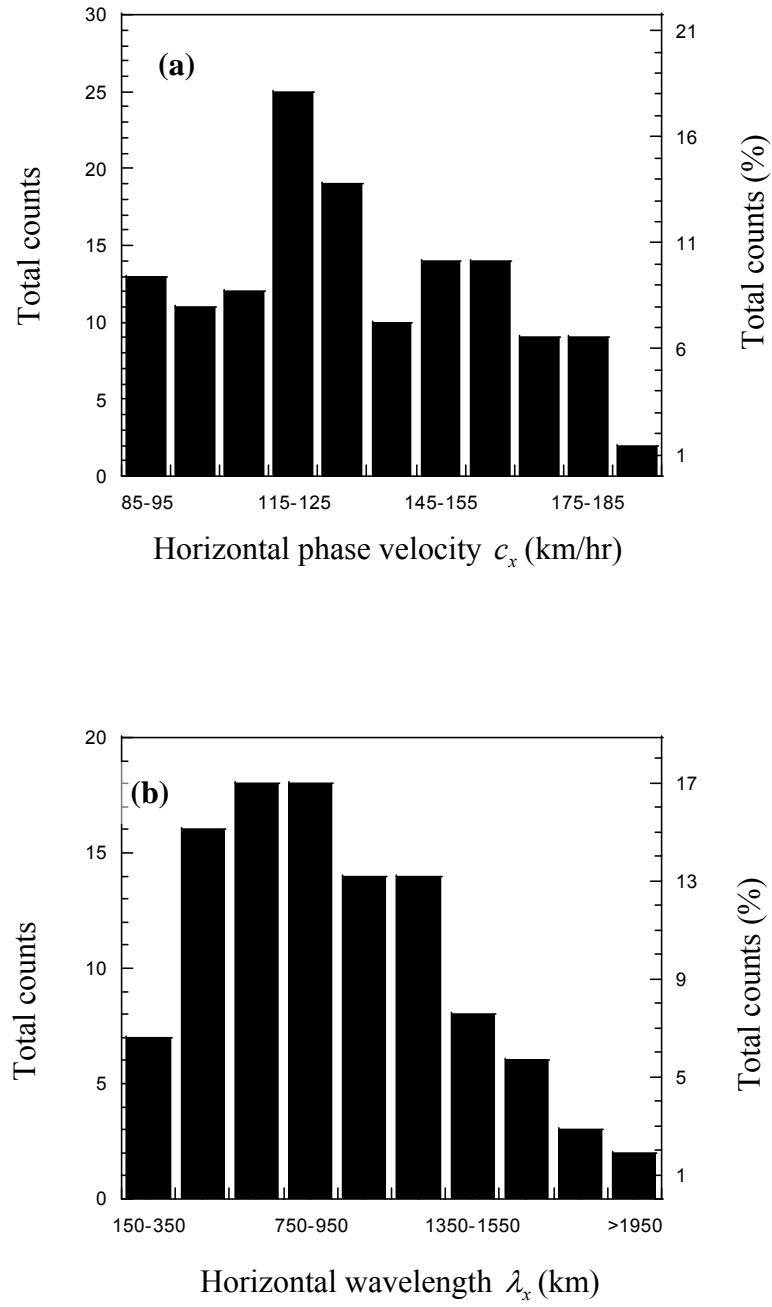


Figure 30. Histograms of deduced gravity wave parameters. (a) Horizontal phase velocities and (b) horizontal wavelengths.

c_x values range from 24 m/s (85 km/hr) to 50 m/s (180 km/hr) with the most common values between 31 m/s (110 km/hr) and 34 m/s (120 km/hr). The λ_x values range from 150 km to 3,000 km with the most common values between 550 km and 950 km. The horizontal distance to the source region, X for waves originating at a 45-km altitude range from 1,000 km to 7,000 km with the most prevalent X values between 2,500 km and 3,500 km. The frequency plot is shown in Figure 31. The X values for wave originating at a 90-km altitude would be twice as big. For reference, 4,000 km is approximately 10% of the Earth's circumference. A source at that distance is a very long way away.

For the lidar observations, the gravity waves have vertical wavelengths ranging from 6 km to 19 km, with dominant wavelengths between 12 and 16 km. The corresponding vertical wave numbers ($k_z = 2\pi/\lambda_z$) range from 10.5×10^{-4} to 3.3×10^{-4}

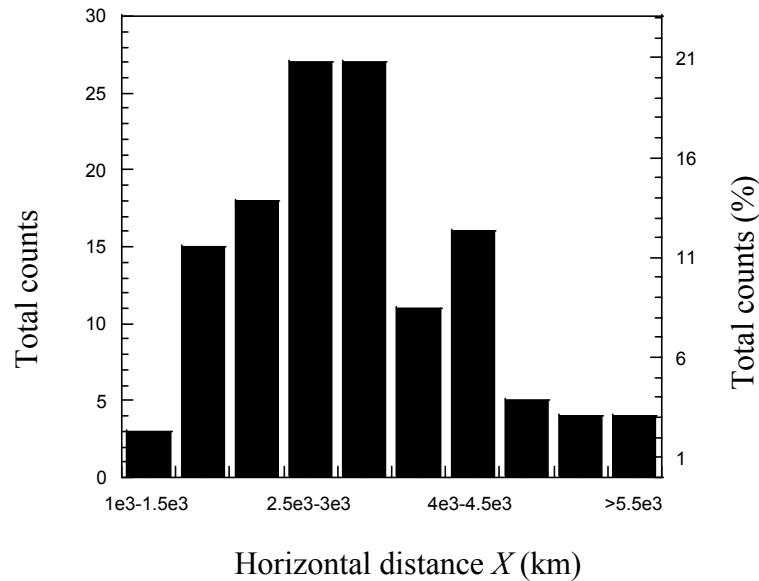


Figure 31. Histogram of gravity wave deduced horizontal distance to the source region for 45 km altitude above ALO.

rad/m with dominant values of 5.2×10^{-4} rad/m and 3.9×10^{-4} rad/m. The dominant values of wave number squared are significantly greater than $1/4H_p^2$ ($5.1 \times 10^{-9} \text{ m}^{-1}$), which is consistent with the approximations used to derive equations (5.1.1) and (5.1.6). The most dominant periods are 6 hours to 8 hours and the corresponding dominant frequencies ($\omega = 2\pi/\tau$) are 2.2×10^{-4} to 3.0×10^{-4} rad/s, which are also significantly higher than the inertial frequency, f (9.5×10^{-5} rad/s). Thus the criteria needed to apply the approximations to derive the gravity wave dispersion relation in Chapter 5 section 2.3 are satisfied.

4. Discussion

Detailed examination of profiles of relative density perturbations observed with the Rayleigh lidar at ALO shows the presence of monochromatic gravity wave motions in the mesosphere (45–90 km). These waves were found on almost every night examined. Some times they exist for only 2 to 3 hours (e.g., Figure 21b), other times for the whole night, up to 10–12 hours (e.g., Figure 21a). They often become less distinct but more complex above about 80 km. For instance, we see many waves with an upward apparent phase velocity in the region above 80 km, but almost none in the region below. Thus, there appears to be a change in the AGW population at approximately 80 km.

A possible hint about what is happening above 80 km comes from *Gardner and Liu* [2007]. They examined the probabilities of dynamic and convective instabilities between 80 and 105 km using Na resonance lidar at the Star Fire Optical Range in New Mexico. They found high probabilities of these instabilities between 80 and 90 km. This supports the idea that the change in AGW behavior above 80 km may arise from the

occurrence of short-lived instabilities leading to gravity wave breaking between 80 and 90 km. As the primary waves break they may give rise to secondary waves propagating in both (upward and downward) directions [Zhou *et al.*, 2002; Lane and Sharman, 2006]. That would also lead to mixture of small- and large-amplitude waves with a mixture of phases.

Returning to the region below 80 km, we examined the spectrum of AGWs with vertical wavelengths from 6 to ~35 km and found waves with vertical wavelengths ranging from 6 to 19 km, with the most frequent values being between 12 and 16 km (Figure 27). Thus, our 3-km averaging in altitude for this analysis appears appropriate. However, there is clearly a short wavelength tail that we would like to explore by reanalyzing the data using a shorter altitude average. We did not find significant seasonal variation in λ_z values (Figure 25a).

The other measured parameter is the vertical downward phase velocity. Unlike the vertical wavelength, the vertical phase velocity shows a clear and strong seasonal variation with larger values in summer and smaller ones in winter (Figure 28a-b). The minimum and maximum values of vertical phase velocities observed are 0.2 to 1.0 m/s (0.72 km/hr to 3.5 km/hr). The most frequent phase velocities in winter are between 0.39 and 0.44 m/s (1.4 and 1.6 km/hr) and in summer between 0.55 and 0.61 m/s (2.0 and 2.2 km/hr) (Figures 28a-b). Thus there appears to be a significant difference between the summer and winter AGW populations. This difference may be related to filtering or to the sources. The two observed parameters are combined in Figure 32 to show the range of values observed with the lidar. The scatter of points also suggests that these two parameters are independent of each other.

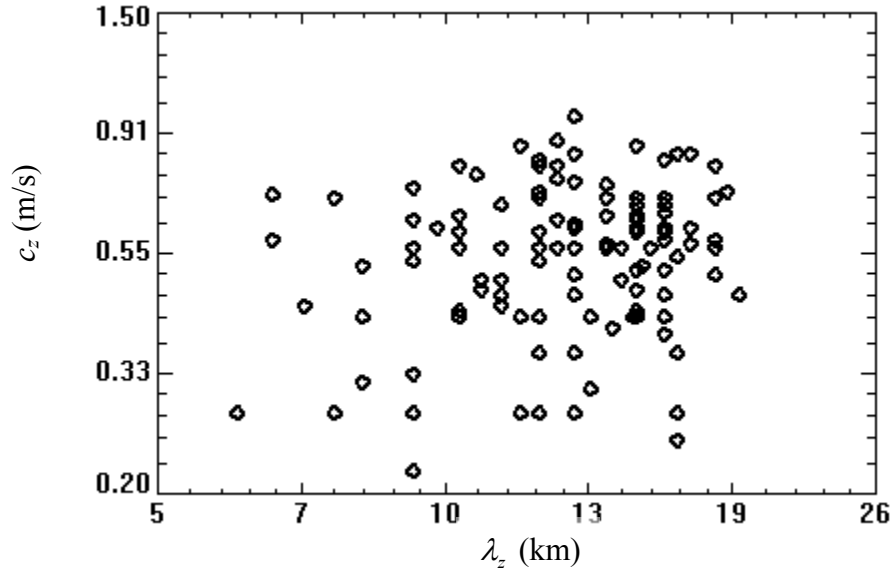


Figure 32. The two measured parameters: downward vertical phase velocity versus vertical wavelength.

Gravity waves have been observed previously in the region between 30 km and just below 60 km [Mitchell *et al.*, 1991; Shibata *et al.*, 1986; Chanin and Hauchecorne, 1981; Gardner *et al.*, 1989; Whiteway *et al.*, 1995]. These waves are characterized by a λ_z value of 10 km in the 45–55 km region and 4 km in the 30–45 km. Periods are commonly less than the inertial period for the latitude of observation and c_z values of the order of 1 km/hr are often observed. To our knowledge, no similar studies have been done before in the region between 45 and 80 or 90 km. Due to lack of long-term observations no one else has reported the clear seasonal studies of the wave parameters. The persistent values of λ_z of 12 to 16 km reported in this study are larger than the values reported in other studies. This discrepancy is reasonable as we covered a much more extended region of the mesosphere. At heights between 45 and 70 km at ALO, Gao *et al.* [1998] spectrally analyzed Rayleigh lidar density perturbations collected over a period of 18 months. They

reported a characteristic vertical wavelength of ~ 12 km, which just overlaps with the present results. However, they did not report any seasonal variation.

Another way to determine the part of the AGW spectrum observed with the lidar is to combine the λ_z and c_z observations to derive the horizontal wavelengths, λ_x , and then to compare λ_z and λ_x . This has been done and the results are shown in Figure 33. While the vertical wavelengths extend from 6 to 19 km, the horizontal wavelengths extend from 150 to 3100 km. The distribution of points show a nice functional relationship between λ_x and λ_z .

As discussed earlier, the values of c_z found in this study lead to the conclusion that both the vertical and horizontal wavelengths are, to a very close approximation, the intrinsic wavelengths. Because the vertical component of the background wind is negligibly small (1-2 cm/s) [Fauliot *et al.*, 1997] compared to the vertical phase speed of

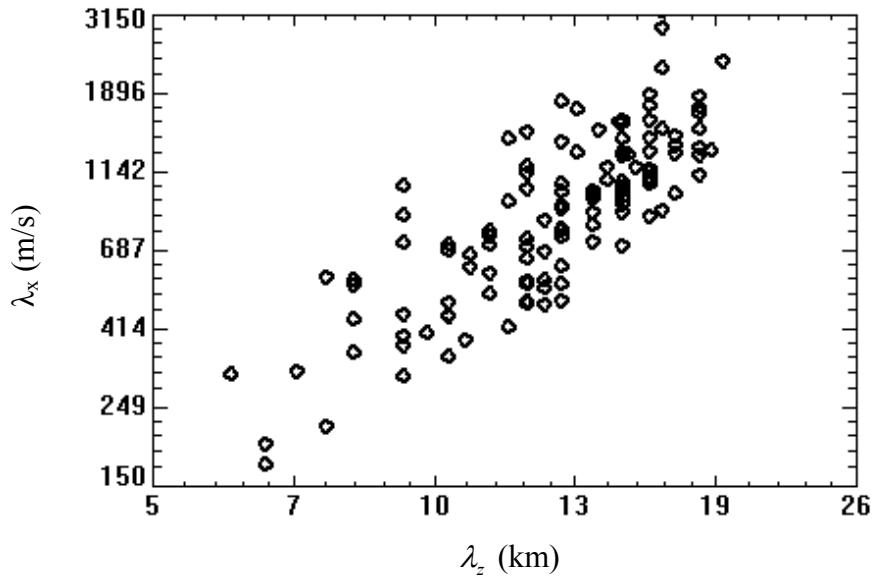


Figure 33. The portion of the AGW spectrum observed with the ALO Rayleigh lidar. This figure shows the horizontal wavelengths (λ_x) and vertical wavelengths (λ_z).

the observed gravity waves, the background vertical wind has essentially no effect on the observed vertical phase velocity. This implies that the observed vertical phase velocities are approximately the intrinsic velocities. As a result, the values of horizontal velocities and horizontal wavelengths derived from equations (5.1.4) and (5.1.5) are approximately the intrinsic values. This result is an important distinction between what can be derived observing vertical phase velocities instead of horizontal phase velocities.

In the foregoing we mentioned the possibility of filtering by critical layers. We will now examine that in more detail. *Lindzen* [1981] reported zonal winds ranging from 2.0 to 50 m/s (7.2–180 km/hr) in summer and 7 to 75 m/s (25–270 km/hr) in winter at mid latitudes between the ground and 90 km. Furthermore, at lower levels (below ~40 km), the zonal wind rarely exceeded 20 m/s in either season. These winds overlap with the horizontal phase speeds we deduced implying that on some days waves might have been filtered and on other days might not have been. It is noteworthy that we did not observe waves with vertical phase speeds smaller than 0.2 m/s. This would be consistent with filtering out waves with slower horizontal phase speeds. We did not see waves with horizontal phase speeds less than 16 m/s. The jet stream near the tropopause has a consistently eastward flow. The mesospheric jet, on the other hand, reverses direction during the equinox seasons. In winter its flow is eastward while in summer its flow is westward. At higher altitudes (above ~45 km, in our observation range), some waves may experience filtering effects depending on their propagation directions and their horizontal phase speeds. This filtering effect may give rise to the seasonal variation in wave parameters. Assuming the same east and west velocity distributions at low altitudes, the observed summer-winter difference in c_z would signify more filtering of lower speed

waves in summer from a stronger mesospheric jet. However, that does not explain the entire observed difference. c_z has a high-speed tail in summer that does not exist in winter. This suggests that the source function, whether the same or different, is stronger in summer than in winter.

We can also deduce the horizontal distance to the source. For waves at 45 km altitude, it ranges from $\sim 1,000$ km to $\sim 7,000$ km, whereas the distances at 90 km are doubled. The distribution of source distances is not uniform between 1,000 km and $\sim 14,000$ km (Figure 31). As just indicated, most of the waves observed in the mesosphere above ALO originated from regions $\sim 1,000$ km to $\sim 7,000$ km distant from ALO. Thus none of the observed waves could have been generated locally. This says that gravity waves observed in the mesosphere above ALO propagated horizontally through a very extended region (at angles ranging between 0.4° and 2.6°). For example, for every 10 km increase in altitude, the typical source region is ~ 570 km further away. Thus an individual vertical profile is as much a measure of how the AGWs are distributed horizontally as it is of what happens when they propagate vertically. Thus the vertical profiles depend on the uniformity of the source region and filtering. It is hard to believe that both (filtering and sources) are truly uniform. Hence, to get a good representative view of what is happening vertically, it is essential to have many observations that can be averaged together.

The extent of the source region, as opposed to its distance, can be estimated in two different ways. For instance, if similar AGWs are seen for eight hours at 45 km, the source has to be turned on for 8 hours. If the horizontal phase velocity is c_x km/hr, then the source is $8c_x$ km in extent along the line from the source. For an average c_x of 130

km/hr from Figure 30a, the source would have to extend over 1100 km. Alternatively, if the wave extends from 45 to 90 km, then it took $45/c_z$ hours to propagate up. The horizontal extent of the source is then that time multiplied by the average horizontal speed. Using an average c_z of 2 km/hr from Figure 28a and 28b, the wave takes 23 hours to rise 45 km, and has a horizontal extent of 3000 km. This is an even greater extent. In either case the source is huge and far away. Based on extent in space and time, many possible sources can be eliminated. They are too big to be a convective squall line or a mountain range. Furthermore, it is far enough away, it could well be over the ocean. It is also too big to be the jet stream. Seemingly, the only possible source big enough is a weather system. Because of the large size of the source region, it is not surprising that the wave pattern often changes during the night. It is only reasonable that the source region is going to vary in time and space.

These waves have horizontal phase velocities ranging from 24 m/s (85 km/hr) to 53 m/s (190 km/hr). They took 14 hours to 63 hours to reach 45 km and 28 hours to 120 hours to reach 90 km. This also reinforces the point that the gravity waves we observe in a vertical profile between 45 km and 90 km originated from a great distance from a very extended source. The profile in reality has to reflect structures in this extended horizontal source region and its time variation as much as it does the effects of vertical transport.

5. Summary and Conclusions

The extensive observations acquired with the Rayleigh-scatter lidar at ALO at the Center for Atmospheric and Space Sciences at Utah State University were used to analyze the relative molecular density perturbations. Unlike previous observations, these observations cover the full mesosphere up to 90 km and long period of time. This

extensive analysis shows the presence of monochromatic gravity wave motions. But, above 80 km, these waves become less identifiable. The wave motions are present on almost all nights. Below 80 km, they have a clear downward phase progression corresponding to upward energy propagation. From the relative density perturbation profiles, the vertical wavelengths and vertical phase velocities are readily apparent and their values easily calculated. The values of the vertical wavelengths and vertical phase velocities are approximately the intrinsic values noting that the vertical background wind is negligibly small. The summary of the results are as follows:

- Although the observations allow wavelengths between 6 and ~ 35 km to be found, the ones found are between 6 and 19 km, with 12 to 16 km being the most prevalent. The prevalent values of λ_z reported in this study are larger than the values reported from other studies. This difference is reasonable as we omitted the stratosphere and covered a much more extended region of the mesosphere.
- Vertical phase velocities vary between 0.2–1.0 m/s (0.72–3.6 km/hr), with 0.5–0.6 m/s (2.0–2.2 km/hr) the most prevalent.
- There is a clear seasonal variation in c_z with larger values in summer than in winter. This extensive seasonal variation in the mid-latitude mesosphere is a new result.
- The wave periods inferred from λ_z and c_z range from 2–18 hours, with 6–8 hours in winter and 4–6 hours in summer being the most prevalent. This extensive seasonal variation in the mid-latitude mesosphere is another new result.
- The horizontal wavelengths and horizontal phase velocities were calculated using the gravity-wave dispersion relation, wave period, and buoyancy period τ_b . The

values of horizontal wavelengths range from $\sim 160\text{--}3,100$ km, with $550\text{--}950$ km being the most prevalent.

- The horizontal phase velocities range from $24\text{--}53$ m/s ($85\text{--}190$ km/hr), with $32\text{--}35$ m/s ($120\text{--}130$ km/hr) the most prevalent.
- While there appears to be a clear seasonal dependence in vertical phase velocity c_z , none appears in the vertical wavelengths λ_z . The parameters c_z and λ_z are important observed parameters and are independent. The seasonal variation in most other parameters depends on c_z . It appears in the period, horizontal wavelength, and the horizontal distance to the source region. A small seasonal variation occurs in the horizontal phase velocity c_x because of small seasonal variation in τ_b .
- The vertical phase velocities maximize in summer whereas the periods, horizontal wavelengths, and horizontal distances to the source region maximize in winter.
- These monochromatic gravity waves are generated between $\sim 1,000$ km and $\sim 14,000$ km from ALO, and often from a very extended region. For monochromatic gravity waves lasting eight hours and for average vertical and horizontal speeds, the extent of the source is a minimum of 1000 km and could be more than 3000 km. In either case the source region is huge and has to last a long time. This great extent suggests that the source is a weather system. Identification of the source extension with such an extensive lidar data set in the entire mesosphere is a new result.

- The uncertainties in the measured and derived wave parameters are much smaller than the day-to-day variations indicating that these large day-to-day variations represent large geophysical variability.

CHAPTER 6

SEASONAL VARIATION OF MESOSPHERIC GRAVITY WAVE

POTENTIAL ENERGY OBSERVED BY RAYLEIGH

LIDAR ABOVE LOGAN, UTAH

Abstract

This work is based on observations of the mesosphere with the Rayleigh Lidar at the Atmospheric Lidar Observatory (41.74° N, 111.81° W) at the Center for Atmospheric and Space Sciences (CASS), Utah State University. This analysis of the lidar data for the gravity wave potential per unit mass E_p is based largely on density fluctuations with 3-km height resolution and 1-hour temporal resolution from 150 nights with data from 45 to 90 km. This provides information on waves with vertical wavelengths between six and ~ 45 km and periods between 2 and ~ 12 hours. The amplitude of the density perturbations and the mean wave potential energy per unit mass both increase with altitude at the adiabatic growth rate below 60–65 km and above 75–80 km. The AGWs give up considerable energy to the background atmosphere relative to the adiabatic growth rate in the intervening altitudes. The altitude and rate at which they give it up is reasonably dependent. Below 70 km, there is a semiannual variation with a maximum in winter and minima in the equinoxes, whereas at the highest altitudes there is an annual variation with a maximum in winter and a minimum in summer. In addition to the seasonal variations, the values of E_p from night to night show great variability, up to a factor of 20, at all heights.

1. Introduction

Atmospheric gravity waves (AGWs) exist due to the stable density stratification of the atmosphere being acted on by gravity. Any disturbances to a steady state can result in excitation of AGWs with a variety of temporal and spatial scales. These waves can have vertical wavelengths that range from less than 1 km to more than 20 km and horizontal wavelengths that range from less than 10 km to more than 3000 km. They can have periods that range from ~5 minutes to almost 18 hours at our latitude. They are believed to originate in the troposphere, the most often suggested sources being orography [*Nastrom and Fritts, 1992*], convective storms [*Alexander et al., 1995; Fritts and Alexander, 2003*] and the jet stream [*Fritts and Nastrom, 1992*]. As they propagate upwards, conservation of energy arguments for adiabatic growth say that the wave amplitude will grow by a factor of e every two-scale heights H , i.e., roughly every 14 km. The potential energy per unit mass E_p will grow by a factor of e every one-scale height H , i.e., roughly every 7 km. They will continue to grow until they reach a critical layer or until energy dissipation occurs. At a critical layer, where the horizontal phase speed of the wave equals the mean wind, the gravity wave gives up its energy and momentum to the wind. Energy dissipation may occur over extended regions, as we shall see, or may occur dramatically in small regions, most likely when the atmosphere becomes unstable. This upward propagation of gravity waves generated at lower altitudes provides a significant coupling between different regions of the atmosphere. The importance of these waves in the middle atmosphere is widely recognized. They strongly influence middle atmosphere circulation and structure by vertically transporting

horizontal momentum, energy, and constituents, which they give up when they dissipate [Lindzen, 1981; Holton, 1983; Gardner and Liu, 2007].

The physics of the middle atmosphere varies greatly over its altitude extent from roughly 10 to 100 km, from the upper troposphere to the lower thermosphere [Sechrist, 1981]. Yet, most observations in a small portion of this region are not representative of just that small altitude region. Instead what is being observed is coupled to regions above and below. Therefore, it is not sufficient to observe, for example, just the region near the stratopause or the region near the mesopause. It is critical to observe the entire middle atmosphere. Appropriate observational method or methods are needed to do that. Starting from lower altitudes, regular balloon observations usually reach only up to 30 km. Various radio techniques such as meteor, MF and MST radars can usually observe the region between 80 km and 105 km. These techniques leave a big hole between 30 and 80 km. The technique that has been developed and has proved very useful for examining this intervening region is Rayleigh-scatter lidar [Hauchecorne and Chanin, 1980]. Rayleigh-scatter lidar measurements of the background molecular number density, background temperature, and the perturbations about the background fields have contributed significantly to gravity wave studies in the middle atmosphere [Chanin and Hauchecorne, 1981; Wilson *et al.*, 1990, 1991a, 1991b; Mitchell *et al.*, 1991; Whiteway and Carswell, 1994; Sears and Wickwar, 2002; Chapter 5]. These wave perturbations when interpreted in terms of potential energy per unit mass E_p are considered a good measure of the strength of gravity wave activity [Wilson *et al.*, 1991a; Mitchell *et al.*, 1991; Whiteway and Carswell, 1995]. It is observed that both the temperature and mean molecular density have seasonal and altitude dependences. It would be reasonable to

expect that the gravity wave potential energy might also have these dependences. Indeed, at Toronto (44°N, 80°W), *Whiteway and Carswell* [1995] observed greater wave energy during winter than during the other seasons. Using the Rayleigh lidar observations from two sites, Haute Provence (44° N, 6° E) and Biscarrose (44° N, 1° W), *Chanin and Hauchecorne* [1981, 1991] and *Wilson et al.* [1991a, b] made detailed studies of GW activity in the middle atmosphere over southern France. They found that the wave potential energy was a maximum during winter and a minimum during summer. They also reported significant day-to-day variability in the potential energy.

In the present study, we use a much more extensive database of observations, covering almost the entire mesosphere (i.e., the region extending from 45 to 90 km in altitude) to further examine how E_p varies in time and altitude. We analyze the data and calculate E_p to see how the waves interact with the background atmosphere. The intent is to see, for example, what happens to these waves as they propagate upward, how they vary with season, and how they vary from day-to-day. Do the waves grow with altitude from 45 to 90 km or do they reach some altitude above which they give up energy to the background atmosphere? The measurements and analysis method are presented in section 2, results of the analysis are presented in section 3, the results are discussed in section 4, and the summary and conclusions are given in section 5.

2. Measurements and Analysis Method

The Rayleigh-scatter lidar system at the ALO in the Center for Atmospheric and Space Sciences is located on the Utah State University (USU) campus in Logan, UT (41.74° N, 111.81° W, 1.47 km above sea level). It has been operated since late 1993, giving rise to an extensive database of nighttime mesospheric profiles of relative densities

and absolute temperatures. The ALO Rayleigh lidar is a vertically pointing, coaxial system. It consists of a frequency-doubled Nd:YAG laser operating at 30 Hz, generating 18–24 watts at 532 nm, and having a 44-cm diameter Newtonian telescope. The signals from below ~18 km are blocked by a mechanical chopper and the gain is reduced by almost 10^3 by an electronic gate for altitudes below 38 km, leading to good data from 45 km to ~90 km. A narrow-band interference filter (1 nm) is used to remove most of the background light from stars, moon, and scattered city lights. The single, gated detector is a green-sensitive, bialkali photomultiplier tube (Electron Tubes 9954B) in a Peltier-cooled housing. A more extensive description of this system is given by *Beissner* [1997], *Wickwar et al.* [2001], *Herron* [2004, 2007], and *Herron and Wickwar* [2009a].

A total of more than 900 nights of observations were collected during a period that spanned 11 years. Of these profiles, 150 extend to 90 km or above and they are the ones used in this study. The data on these clear nights were collected continuously for a period of 4 to 12 hours. The recorded raw data is in the form of photon count profiles with an altitude resolution of 37.5 m (250-ns sampling interval) and a temporal resolution of two minutes (3600 laser pulses) from the ground to 500 km. The data of interest for this study start at 45 km. At each altitude z , the observed photon counts are the sum of a background signal (from the detector, moonlight, starlight, and scattered city lights) and the signal of interest from the backscattered laser pulses. The background signal is determined between 120 and 180 km and subtracted from the total. This remaining signal, multiplied by the square of the range from the laser, is proportional to the mass density of the atmosphere $\rho(z)$, assuming a constant mean-molecular mass m in the portion of the atmosphere in which we are interested. However, the constant of

proportionality may vary from one 2-minute profile to the next because of changes in the atmosphere's transmittance or because of the variations in the power of the laser. To reduce the influence of signal fluctuations caused by these effects, the profiles are normalized to unity at 45 km. Before normalizing a profile to unity, the data are averaged over 3 km (81 sampling intervals) and 1 hour. The all-night averaged profiles are obtained by averaging together the individual soundings of the atmosphere for the entire night into a single relative density profile that is normalized to unity at 45 km. Temperatures are determined from these relative densities by using hydrostatic equilibrium and the ideal gas law [*Hauchecorne and Chanin*, 1980]. The details, as applied to this lidar, are reviewed by *Beissner* [1997], *Wickwar et al.* [2001], *Herron* [2004, 2007], and *Herron and Wickwar* [2009a].

An individual measured density profile is represented by

$$\rho(z) = \rho_0(z) + \rho_1(z), \quad (6.1.1)$$

where $\rho_1(z)$ is the wave induced perturbation density and $\rho_0(z)$ is the background mean state of the atmosphere (i.e., the unperturbed density profile). The background density profile is first estimated by least squares fitting a sixth order polynomial to the logarithm of the all-night averaged density profile. The difference of the measured profile $\rho(z)$ from the background profile $\rho_0(z)$ provides the density perturbation profile $\rho_1(z)$ and the fractional or relative density perturbation profile

$$\frac{\rho_1(z)}{\rho_0(z)} = \frac{\rho(z) - \rho_0(z)}{\rho_0(z)}. \quad (6.1.2)$$

Temporally, the profiles in equation (6.1.2) contain information about waves with periods greater than twice the integration time used for $\rho(z)$. For our case with a 1-hour integration time that, in principle, means waves with periods longer than 2-hours and shorter than something related to the observation period (in our case 4–12 hours). With a vertical integration of three km between 45 and 90 km, these waves contain information about waves with vertical wavelengths between 6 km and 45 km.

Thus, for each integration period, a profile of the relative density fluctuations has been derived. These fluctuations include contributions from both geophysical variability and measurement uncertainty (photon counting). To examine the geophysical variability, these two contributions need to be separated. Furthermore, to compare what happens on different nights the variability has to be determined for the whole night. The appropriate measure is the variance. At a given altitude the total variance of density fluctuations about the estimated background density was computed from the series of 1-hour density profiles obtained on a given night. This variance represents the combined effects of waves and of statistical fluctuations (uncertainty) from the photon-counting process. Therefore, the geophysical variance of atmospheric density fluctuations at a given altitude z is

$$\overline{\rho_1^2(z)} = \frac{1}{N_p - 1} \sum_{i=1}^{N_p} \rho_{1i}^2(z) - \overline{\sigma_\rho^2} \quad (6.1.3)$$

[*Whiteway and Carswell, 1995*], where N_p is the number of 1-hour profiles used. The second term is the total variance in the one-hour measurements. The third term is the variance arising from propagating the photon counting uncertainty. Its derivation is given below.

Assuming the atmospheric transmission at 532 nm is unity in the mesosphere (i.e. the laser pulse energy remains constant above 42 km), the ratio of the backscattered photon count signal $N_s(z)$ at two altitudes (z_1 and z_2) is proportional to the ratio of the density $\rho(z)$ at these altitudes scaled by range squared $h_1^2(z)$ and $h_2^2(z)$,

$$\frac{N_s(z_2)}{N_s(z_1)} = \frac{\rho(z_2)}{h_2^2} \bigg/ \frac{\rho(z_1)}{h_1^2}, \quad (6.1.4)$$

where $h(z) = z - 1470$ in meters. Thus we can derive a relative density profile $\rho(z, z_0)$ from the backscattered lidar signal,

$$\rho(z, z_0) = \frac{\rho(z)}{\rho(z_0)} = \frac{N_s(z)}{N_s(z_0)} \frac{h^2}{h_0^2} \quad (6.1.5)$$

$$\rho(z, z_0) = \frac{(N(z) - N_B)}{(N(z_0) - N_B)} \frac{h^2}{h_0^2}, \quad (6.1.6)$$

where $N(z)$ is the observed photon counts including signal and background, N_B is the observed background photon counts, and the reference altitude z_0 is 45 km. Clearly $\rho(z_0, z_0) = 1$.

Equation (6.1.6) can be written in a simplified form as

$$X = \frac{(S - B)}{(L - B)} \times C, \quad (6.1.7)$$

where $X = \rho(z, z_0)$, $S = N(z)$, $L = N(z_0)$, and $B = N_B$ are variables and $C = h^2/h_0^2$ is a constant. The quantities S , L and B are independent, and following *Bevington and Robinson* [1969] the variance of the relative density X is given by

$$\sigma_X^2 = \left(\frac{\partial X}{\partial S} \right)^2 \sigma_S^2 + \left(\frac{\partial X}{\partial B} \right)^2 \sigma_B^2 + \left(\frac{\partial X}{\partial L} \right)^2 \sigma_L^2, \quad (6.1.8)$$

becoming

$$\sigma_X^2 = \left(\frac{X}{S-B} \right)^2 \sigma_S^2 + \left(\frac{X}{L-B} \right)^2 \sigma_L^2 + \left\{ \left(\frac{X}{S-B} \right)^2 + \left(\frac{X}{L-B} \right)^2 - \frac{2X^2}{(S-B)(L-B)} \right\} \sigma_B^2. \quad (6.1.9)$$

Because the return signals follow Poisson distributions, the return signal can be substituted in place of the variance: $\sigma_S^2 = S = N(z)$, $\sigma_L^2 = L = N(z_0)$ and $\sigma_B^2 = B = N_B/K$, where K = the number of range bins over which the average N_B is calculated. Combining these, the variance of the relative density $\sigma_{\rho_i}^2(z, z_0)$ for a 1-hour individual profile is given by

$$\sigma_{\rho_i}^2(z, z_0) = \left(\frac{N_i(z)}{N_{Si}^2(z)} + \frac{N_i(z_0)}{N_{Si}^2(z_0)} + \left\{ \frac{1}{N_{Si}^2(z)} + \frac{1}{N_{Si}^2(z_0)} - \frac{2}{N_{Si}(z)N_{Si}(z_0)} \right\} \frac{N_{Bi}}{K} \right) \rho_i^2(z, z_0), \quad (6.1.10)$$

where $N_{Si}(z) = S_i - B_i$ and $N_{Si}(z_0) = L_i - B_i$. The variance from photon counting is given by the nighttime average

$$\overline{\sigma_{\rho}^2} = \frac{1}{(N_P)} \sum_{i=1}^{N_P} \sigma_{\rho_i}^2, \quad (6.1.11)$$

where $\sigma_{\rho_i}^2 = S_i + B_i$ is the variance for the 1-hour integrations and S_i and B_i are the 1-hour photon counts for the signal plus background and the background. This gives the third term in equation (6.1.3).

Equation (6.1.3) thus gives the geophysical variance for the density fluctuations about the background density. For the subsequent analysis, a more useful quantity is the geophysical variance of the fractional or relative density perturbation profile given by

equation (6.1.2). Because $\rho_0(z)$ is the background density profile, no uncertainty is associated with it. Accordingly, the geophysical variance of the fractional or relative density perturbation profile is given by equation (6.1.3) divided by $\rho_0^2(z)$. In turn, this provides two useful parameters. The first is the square root of this variance,

$$\sigma_{\rho_1\rho_0} = \left[\frac{\rho_1^2(z)}{\rho_0^2(z)} \right]^{\frac{1}{2}}, \quad (6.1.12)$$

which will be referred to as the rms relative density fluctuation or perturbation. The second is the average potential energy per unit mass,

$$E_p(z) = \frac{1}{2} \left[\frac{g(z)}{N(z)} \right]^2 \left[\frac{\rho_1(z)}{\rho_0(z)} \right]^2 \quad (6.1.13)$$

[e.g., *Mitchell et al.*, 1991; *Wilson et al.*, 1991b; *Whiteway and Carswell*, 1995], where $g(z)$ is gravitational acceleration (m/s²) and $N^2(z)$ is the square of the Brunt-Väisälä angular frequency (rad/s)² given by

$$N^2(z) = \frac{g(z)}{T(z)} \left[\frac{\partial T(z)}{\partial z} + \frac{g(z)}{c_p} \right], \quad (6.1.14)$$

where $T(z)$ is the mean temperature for the night, $\partial T(z)/\partial z$ is the mean temperature gradient for the night, and c_p is the specific heat at constant pressure. The term $g(z)/c_p$ is the adiabatic lapse rate. The Brunt-Väisälä angular frequency squared, its uncertainty, and its climatology at ALO are discussed in Chapter 4.

The geophysical variance associated with $E_p(z)$ $\sigma_{E_p}^2$ is determined as

$$\sigma_{E_p}^2 = \left(\frac{\partial E_p}{\partial \rho_1} \right)^2 \sigma_{\rho_1}^2 + \left(\frac{\partial E_p}{\partial (N^2)} \right)^2 \sigma_{N^2}^2, \quad (6.1.15)$$

where $\sigma_{N^2}^2$ is determined as in Equation 4.1.3 and $\sigma_{\rho_1}^2(z)$ is given by equation (6.1.3).

The contribution of the covariance term to $\sigma_{E_p}^2$ was examined, but did not make a significant contribution. Consequently, it was dropped from further consideration.

3. Results of the Analysis

3.1. Examples of the Parameters Derived

A winter and a summer example of the measured and derived profiles of parameters that are used to calculate profiles of rms relative density perturbations and $E_p(z)$ between 45 and 90 km are shown in Figures 34a-f and 35a-f. Figures 34a and 35a show the observed density profiles averaged over the night and the background profile from 45-to-90-km (red dashed lines). Figures 34b and 35b show the corresponding temperature profiles derived from the relative density profiles in Figures 34a and 35a. The corresponding profiles of temperature gradient and the N^2 are given in Figures 34c and 35c and 34d and 35d, respectively. Figures 34e and 35e are the corresponding profiles of fractional or relative density perturbations averaged over the night. The green solid lines show the exponential growth curves proportional to $\exp(\Delta z/2H)$ for comparison, where $H(z) = kT(z)/mg(z)$ is the scale height and k is Boltzmann's constant, m is the mass and Δz is the altitude increment above 45 km. Figures 34e and 35e show that between 45 and about 72 km for these two days the amplitude of the observed fluctuations increases

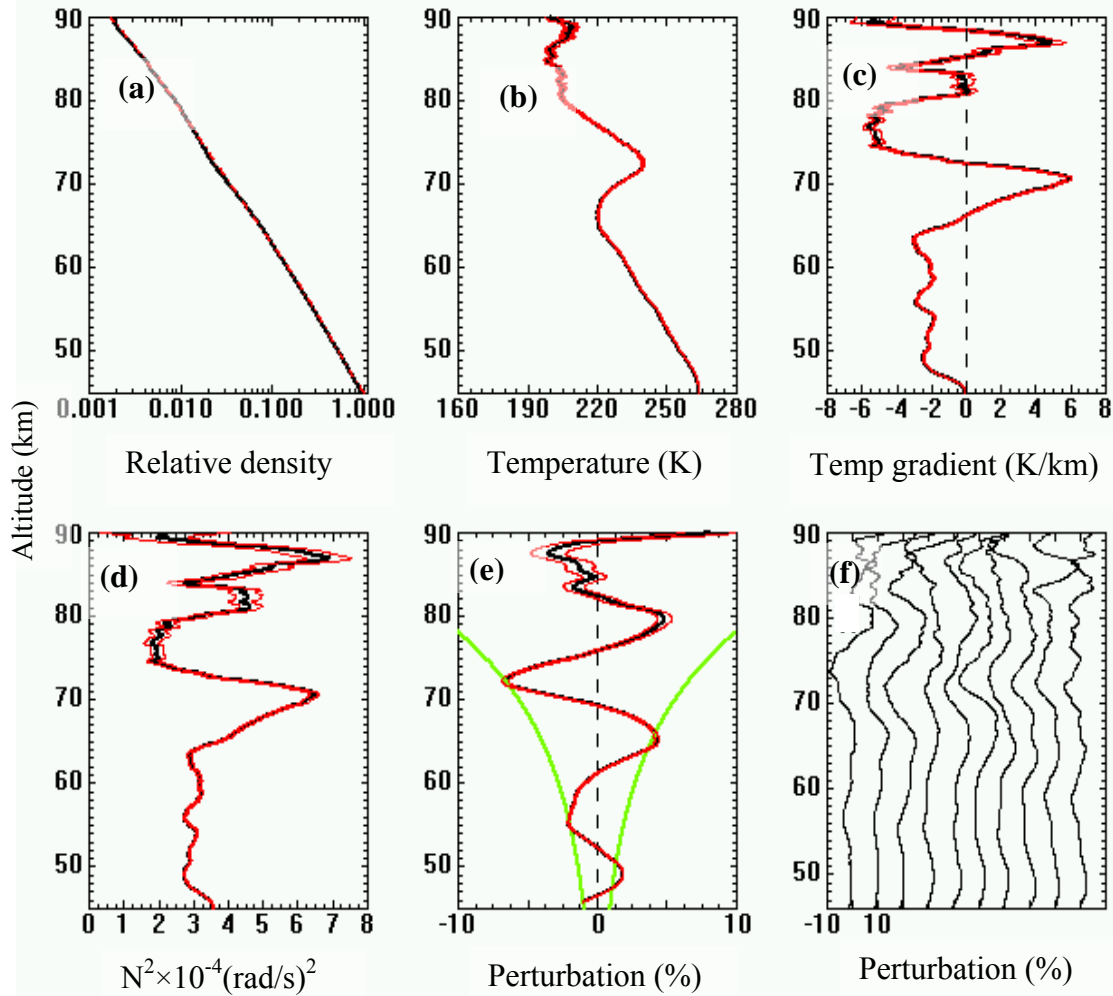


Figure 34. Temperatures, relative densities, and derived parameters for 22 February 1995. (a) A profile of observed relative density and estimated background density (red dashed line). (b) The corresponding profile of the absolute temperature averaged over the night and its uncertainty. (c) Temperature gradient profile and its uncertainty. (d) Corresponding N^2 profile and its uncertainty. (e) Average of the 1-hour relative density perturbation profiles over the night and its uncertainty. (f) Sequences of individual 1-hour relative density perturbation profiles. Each 1-hour profile is offset from the previous one by 10%. The green curves in (e), proportional to $\exp(\Delta z/2H)$, are the adiabatic growth curves. Red curves are the measurement uncertainties.

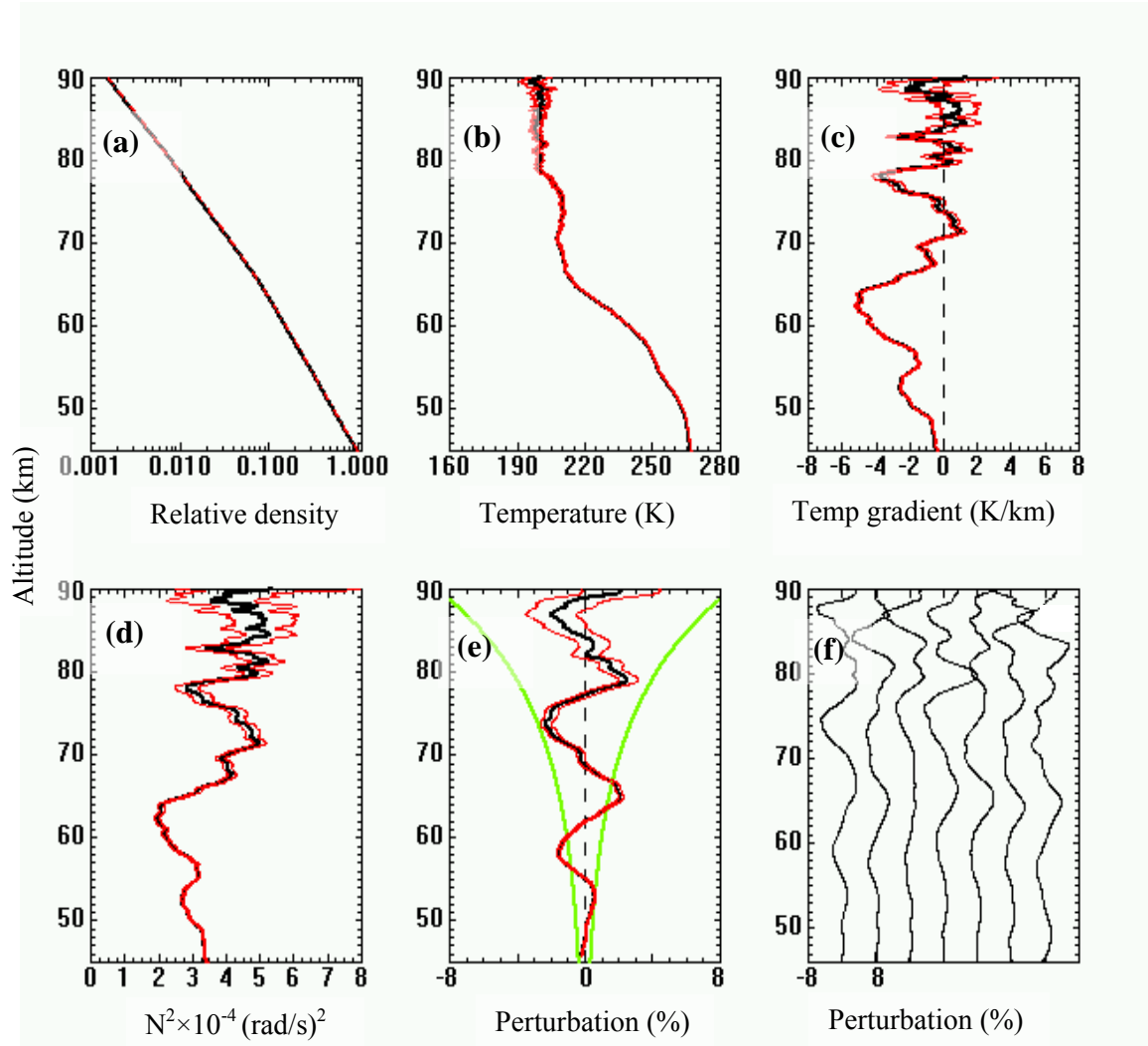


Figure 35. Temperatures, relative densities, and derived parameters for 17 August 1995. (a) A profile of observed relative density and estimated background density (red dashed line). (b) The corresponding profile of the absolute temperature averaged over the night and its uncertainty. (c) Temperature gradient profile and its uncertainty. (d) Corresponding N^2 profile and its uncertainty. (e) Average of the 1-hour relative density perturbation profiles over the night and its uncertainty. (f) Sequences of individual 1-hour relative density perturbation profiles. Each 1-hour profile is offset from the previous one by 8%. The green curves in (e), proportional to $\exp(\Delta z/2H)$, are the adiabatic growth curves. Red curves are the measurement uncertainties.

at a rate very close to that expected for adiabatic growth. However, above about 72 km, the perturbation amplitudes grow very slowly, if at all, compared to the adiabatic growth rates. Figures 34e and 35e also show that the fluctuations are much bigger on February 22, 1995, than on August 17, 1995. Sequences of 1-hour fractional density perturbation profiles are shown in Figures 34f and 35f. As in panels e, they allow the waves growing with altitude until between 75 and 80 km, at which point the wave structure ceases to grow and becomes less organized. The measurement uncertainties in several of the panels are shown by solid red lines.

These two examples also illustrate the effects of temperature inversions on the derived parameters. On February 22, 1995, a large inversion occurs with its maximum temperature at 73 km. The temperature gradient has a zero value at this temperature maximum and at 66 km, which marks the beginning of the inversion and is often given as the altitude of the inversion. In between these altitudes, at 69 km, the temperature gradient and N^2 both have maxima. The amplitude of the mean relative density perturbation over the night increases exponentially at the adiabatic rate from 1% at 48 km to 6% at 72 km. Above 72 km, the amplitude is slightly smaller and the growth rate is much slower than the adiabatic growth rate. The sequence of 1-hour density perturbation profiles shows evidence of monochromatic gravity wave features for most of the night with vertical wavelengths λ_z of approximately 17 km below about 80 km and a downward phase progression with vertical phase velocity of $c_z = 0.41 \text{ m/s}$ (1.47 km/hr). Above 80 km, the waves are more chaotic or random in phase and the amplitudes fall off (Figure 34f). The maxima and minima in relative density perturbations (Figure 34e) correspond to temperature minima and maxima (Figure 34b) as described by ideal gas

law (i.e. $p = nkT$, where p is pressure, k is Boltzmann's constant, and T is the temperature) for constant pressure. This correspondence would be more apparent on a profile of relative temperature variations.

On August 17 1995, a smaller, but distinct structure or bump occurs between 70 and 76 km on the temperature profile. In that sense it appears to be small inversion. Despite being small, the gradient and N^2 profiles have distinct relative maxima at 72 km. In both cases there are small changes in the gradients at lower and higher altitudes, which may be secondary inversions or waves. In either case, they lead to relative maxima in the gradient and in N^2 . The amplitude of the mean relative density perturbation over the night increases exponentially from 0.2% at 48 km to 2.5% at 73 km. Above 73 km, the amplitude is slightly smaller and the growth rate is much slower than the adiabatic growth rate. The sequence of density perturbation profiles shows clear evidence of monochromatic features with vertical wavelengths λ_z near 14 km up to 80 km for the first three profiles. However, these wave features are not as identifiable and are much smaller above about 80 km. There appear to be more waves, some with upward and some with downward phase progressions. Below 80 km, the wave has a downward phase progression with a vertical phase velocity of $c_z = 0.78 \text{ m/s}$ (2.80 km/hr) (Figure 35f). (More AGW information has been derived on these two days in Chapter 5 where they were also used as example.)

$E_p(z)$ and rms relative density perturbation profiles were determined from the variance of density fluctuations and used to infer whether there was dissipation of wave energy. One aspect of examining the altitude profiles of rms relative density fluctuations

and of potential energy per unit mass $E_p(z)$ is to see how these quantities grow with altitude. If we consider an adiabatic situation with conservative waves, waves that do not exchange energy with the atmosphere through which they pass, then certain predictions can be made. Assuming a constant Brunt-Väisälä frequency for non-dissipative gravity-wave propagation, the amplitude of the induced density perturbations will grow with altitude, in response to diminishing density, in proportion to $\exp(z/2H)$ (the green lines in Figure 34e and 35e) [Wilson *et al.*, 1991a; Whiteway and Carswell, 1995]. Under these some conditions, the $E_p(z)$ values will increase as $\exp(z/H)$ [Wilson *et al.*, 1991a; Whiteway and Carswell, 1995]. Profiles of rms relative density perturbation and available $E_p(z)$ values for these two winter and summer days are shown in Figures 36a-d. The adiabatic growth rates are also shown for comparison (black dashed curves in Figure 36). Profiles of rms density perturbation and $E_p(z)$ are very structured on February 22, 1995, as a result of the large amplitude monochromatic gravity wave seen in Figure 34. In addition, as most easily seen at 48 km, the rms relative density perturbations and $E_p(z)$ have an almost factor of two larger magnitude than those on August 17, 1995. For February 22, 1995, the rms relative density perturbations increase by a factor of about 10 from 48 to 90 km, and the $E_p(z)$ values increase by a factor of about 120 over the same range. There is a significant departure in rms relative densities and $E_p(z)$ values from the corresponding adiabatic growth curves (dashed black curves) in small altitude regions indicating that both increase less rapidly with altitude than expected for the adiabatic situation in these limited regions. This implies a continuous transfer of energy from the

waves to the background atmosphere. These are also the conditions for a continuous transfer of momentum to the background atmosphere [Wilson *et al.*, 1991a; Mitchell *et al.*, 1991; Whiteway and Carswell, 1995].

For August 17, 1995, the rms density perturbations increase by a factor of about 12 and the $E_p(z)$ values increase by a factor of about 150 between 48 and 90 km altitude (Figures 36c and 36d). Between 48 and 68 km the observed curves (black solid curves) follow the adiabatic curves (black dashed curves) very closely. Then between 68 and 76

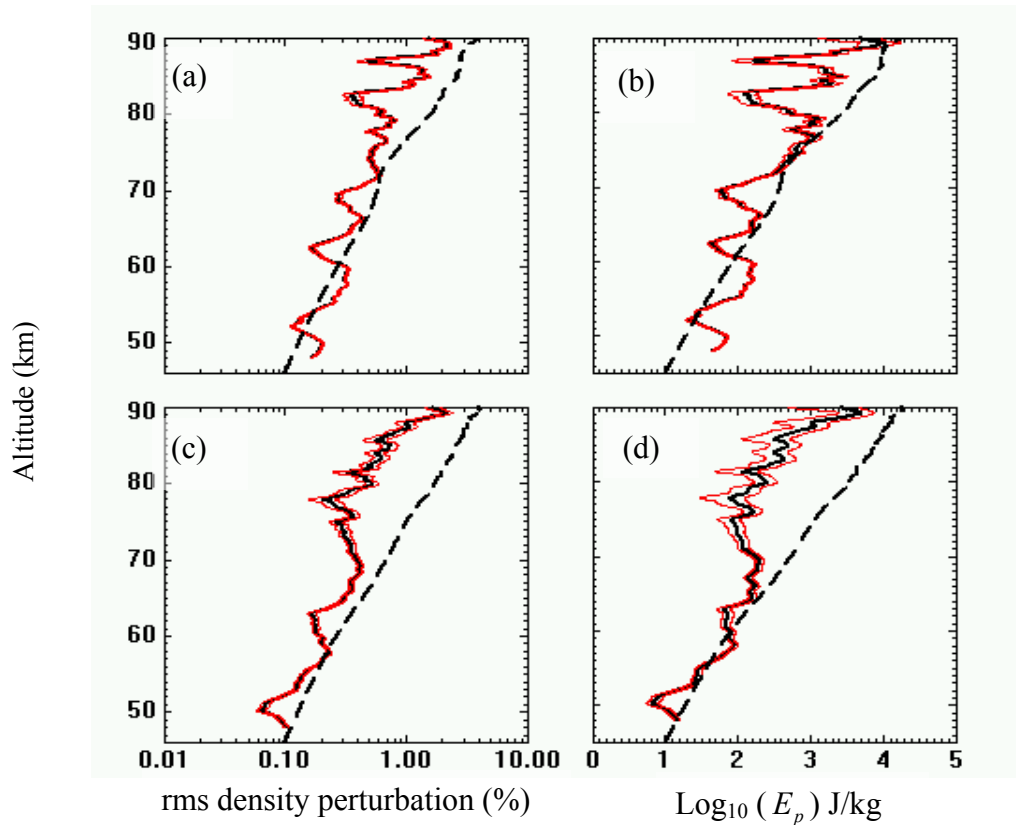


Figure 36. Profiles of root-mean-square (rms) density perturbation and available potential energy per unit mass for a winter and summer day. (a) and (c) show the rms density perturbations. (b) and (d) show the values of E_p . Dashed black curves show the adiabatic growth rates for comparison. Measurement uncertainties are shown by solid red curves.

km (when N^2 has a relative maxima) they both fall off rapidly. Then above 76 km they again grow at a rate close to the adiabatic rate. (This is very much like the behavior on 23 July, 1996, shown in Chapter 3, Figure 8.) These two specific summer days with their large E_p decreases over a small altitude range behave very differently than February 22, 1995.

3.2. Seasonal Variation in Wave Activity

Profiles of $E_p(z)$ values were averaged for each season over the period of 11 years. The seasons were defined in the same way as they were defined in Chapter 4. The seasonal mean values of $E_p(z)$ are shown in Figures 37a-e. They grow with altitude, but the rate of growth varies with altitude and season. In winter, Figure 37a, between 48 and 62 km the observed $E_p(z)$ grows at a rate very close to the adiabatic growth. From 62–68 km $E_p(z)$ falls off rapidly and then from 68–75 km it grows at a little less than the adiabatic growth rate. Above 75 km it grows at close to the adiabatic rate. In summer, Figures 37b, $E_p(z)$ grows at very close to the adiabatic growth rate from 48–58 km, followed by a slow drop off between 58 and 75 km. Above 75 km, $E_p(z)$ again grows at close to the adiabatic rate. In spring and fall equinoxes, it appears that the observed $E_p(z)$ values grow at rates very close to the adiabatic rate between 50 and 60 or 63 km, followed by a sudden drop off in spring equinox and a gradual drop off in fall equinox (Figures 37c and d). Above 65 km, $E_p(z)$ in spring equinox again grows at rates close to the adiabatic growth rate. Above 75 km, $E_p(z)$ starts to again follow the adiabatic curve

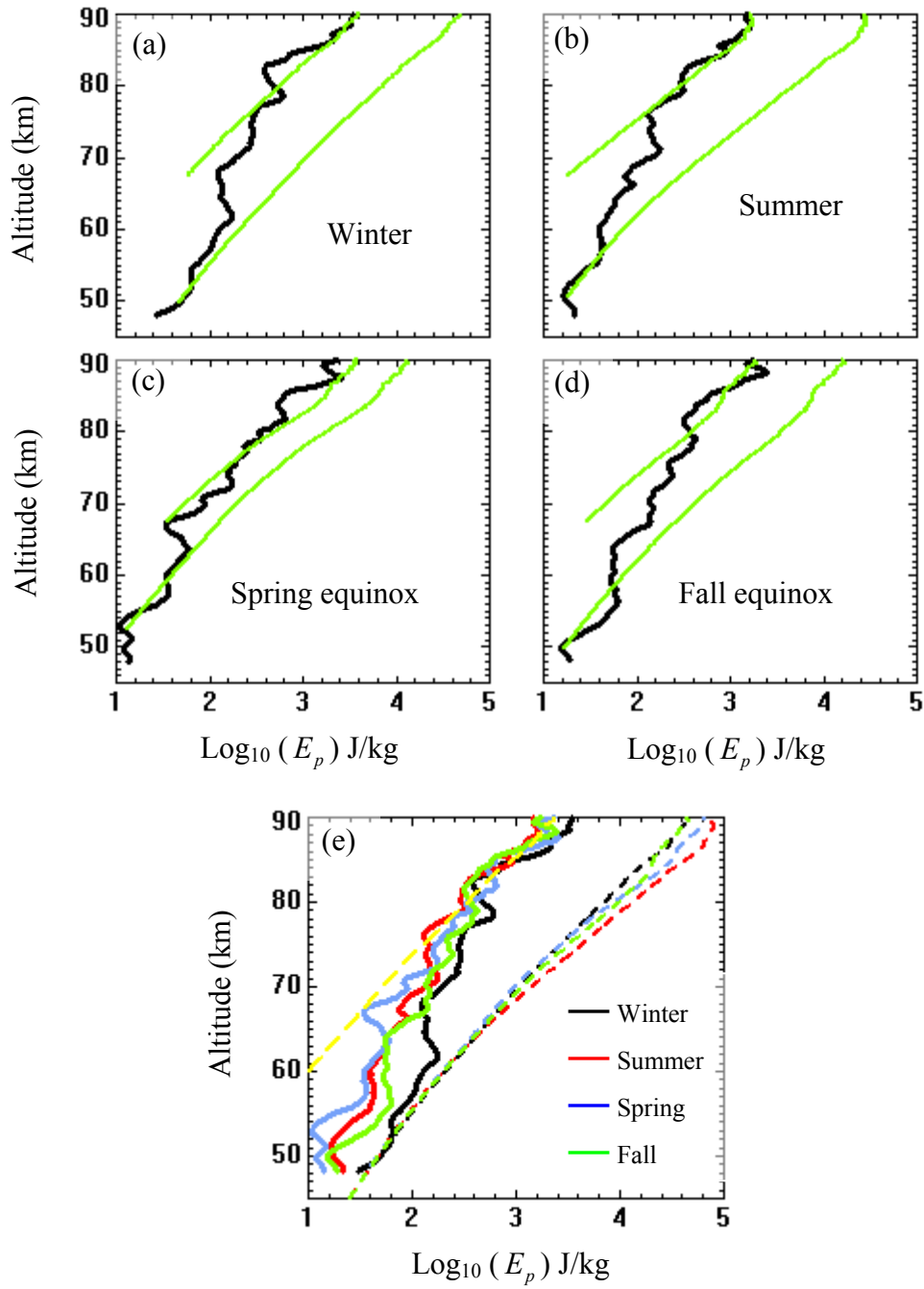


Figure 37. Profiles of mean $E_p(z)$ for different seasons. (a) Winter. (b) Summer. (c) Spring equinox. (d) Fall equinox. (e) Summary plot of Figures (a), (b), (c), and (d). The corresponding adiabatic growth rates for $E_p(z)$ are indicated by green solid curves (plots a-d) or colored dashed curves (plot e).

above 75 km. However, there seems to be a seasonal variation in the altitude where $E_p(z)$ falls off and then resumes growing at the adiabatic rate. It falls off more rapidly at a higher altitude in winter and spring equinox than in summer and fall equinox. It is not clear whether the fall off is more gradual in summer and fall equinox or whether the fall off is sharp on a given day and moves up and down in altitude from day to day giving an average that is gradual.

The seasonal and day-to-day variations are further examined by fitting the many nighttime $E_p(z)$ values with 12- and 6-months sinusoids. Figure 38 shows the results at six different altitudes: 48, 50, 60, 70, 80, and 90 km. Over this full altitude region from the stratopause to the upper mesosphere, the greatest values of $E_p(z)$ at any one altitude are approximately 20 times the smallest values. This is a huge factor for day-to-day variability. The uncertainties in $E_p(z)$, i.e., σ_{E_p} from equation (6.1.14) applied to several days at these six different altitudes, are given in Table 4. As seen in Table 4, the uncertainties are much smaller than the day-to-day variations indicating that these large day-to-day variations represent large geophysical variability. The actual mean $E_p(z)$ values are given in parentheses.

The other striking feature is the change in seasonal variation of $E_p(z)$ with altitude from semiannual at the lowest altitudes to annual at the highest altitudes. The fits show a strong semiannual and annual variation up through 60 km with a winter maximum, a summer relative maximum, and two almost equal equinox minima. The secondary summer maximum has approximately 60% of the $E_p(z)$ of the winter maximum and the equinox minima just over 40%. By 70 km the seasonal structure has

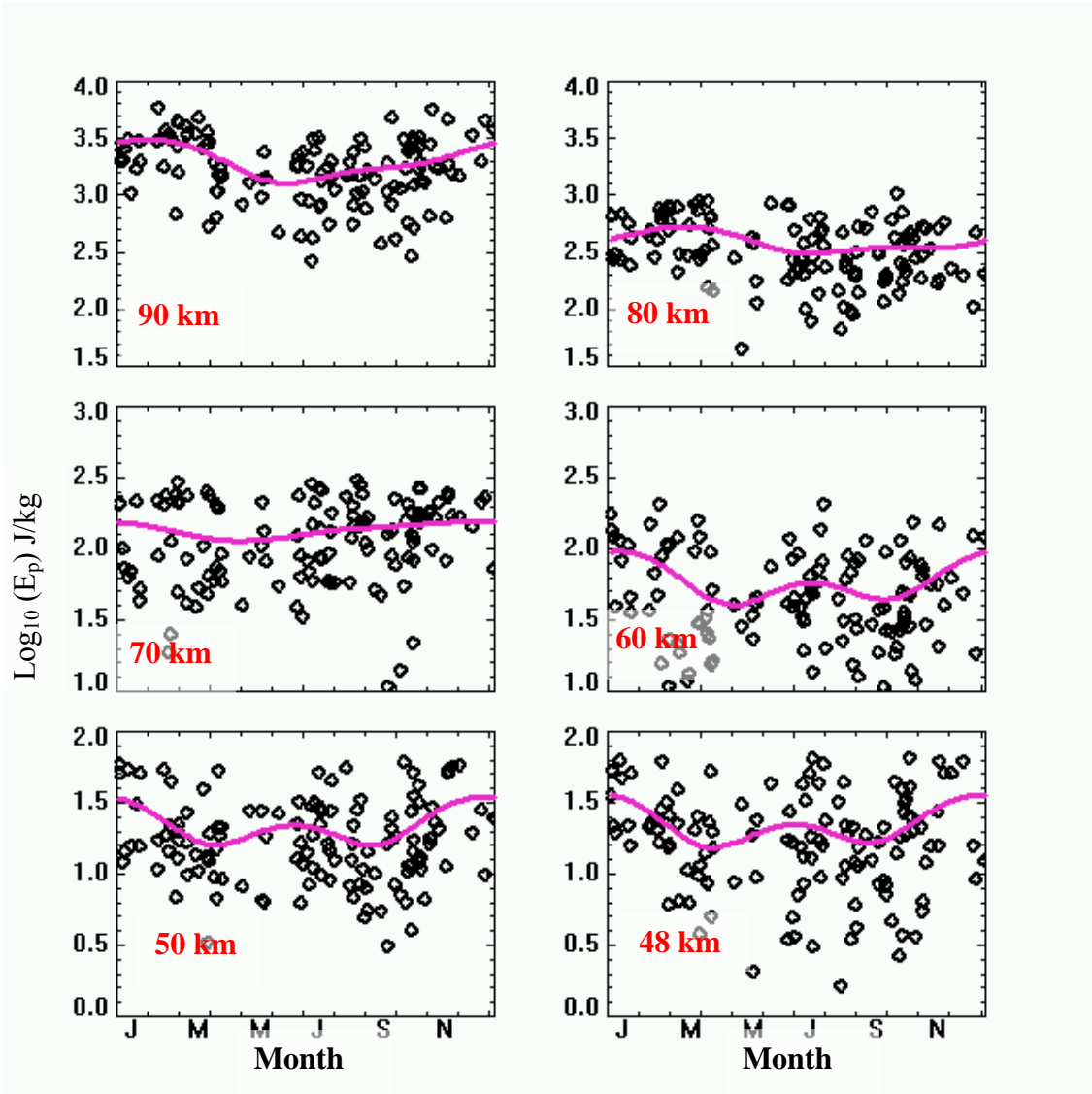


Figure 38. Day-to-day and seasonal variation in E_p values at several altitudes. Pink solid curves are the least square fits by periodic functions with periods of 12 and 6 months.

almost disappeared leaving a small minimum that is approximately 70% of the maxima.

At 80 and 90 km the seasonal variation is almost entirely annual with a June minimum about 40% of the winter maximum.

Table 4. Examples of Uncertainties Calculated for E_p at Various Altitudes

Altitude (km)	48	50	60	70	80	90
σ_{E_p} (J/kg)	1.5 (30)	1.8 (35)	5(85)	20 (200)	100 (650)	700 (3000)

4. Discussion

In this paper we examined the characteristics of what happens to the gravity wave potential energy per unit mass $E_p(z)$ carried into the mesosphere from below. We examined the temporal and altitude variation of $E_p(z)$ and found that $E_p(z)$ is highly variable from day to day, by almost a factor of 20 throughout the mesosphere. This implies major day-to-day differences in the sources, the filtering, or both. From the study of seasonal variability we found a semiannual variation in $E_p(z)$ up through 60 km with a maximum in winter, which is consistent with less filtering in winter than in summer, presumably because both jets are directed towards the east [Hines and Reddy, 1967]. It might also reflect stronger sources in winter. We cannot distinguish between these two possibilities. We found minimum $E_p(z)$ values at the equinoxes. With the mesospheric jet near zero or weak during equinoxes, there should be even less filtering than in summer. The fact that $E_p(z)$ is weakest then suggests that the sources are weakest at that time.

There is almost no seasonal variation in $E_p(z)$ at 70 km. This change is consistent with the seasonal behavior shown in Figure 37 relative to the adiabatic growth rates. Between 60 and 70 km, $E_p(z)$ falls off significantly in all seasons, but falls off much more in winter. This is consistent with the waves giving up more energy per km to

the background atmosphere in winter than in the equinoxes. They also give up a little more energy per km in summer than in the equinoxes.

At higher altitudes, we found almost an entirely annual variation in $E_p(z)$ with the strongest values in winter and the weakest in summer. To increase this annual variation, between 70 and 90 km, the summer waves have to give up more energy per km relative to the adiabatic growth rate to the background atmosphere than in winter and in the equinoxes. Again, this is consistent with the growth rates shown in Figure 37.

According to the gravity-wave, linear theory [Hines, 1960], the amplitude of AGW perturbations grow exponentially with an e-folding distance of 2-scale heights, approximately 14 km, and the potential energy per unit mass grows exponentially with an e-folding distance of 1-scale height, approximately 7 km. On a couple of summer days and on all the seasonal averages, we appear to follow the predictions of linear theory for altitude lower than 55–65 km and for altitudes higher than 75–80 km. In between 60 and 80 km (or 65 and 75 km), the waves give up considerable energy to the background atmosphere. In this paper we speculate that these are regions of convective or dynamic instability. (We examine this loss of potential energy to the background atmosphere in the next paper.)

In Chapter 5, we noted that the AGW characteristics appeared to change above about 80 km. More specifically, we saw more waves above 80 km than below, we could not as easily identify perturbation maxima or minima, and we saw waves with upward phase velocities. This study provides more quantitative information. In Figures 34e and 35e showing the relative density perturbations, i.e., $\sum_{i=1}^{N_p}(\rho_{li}/\rho_0)$, based on 1-hour

integrations for two days, the positive and negative oscillations grow in amplitude at an exponential rate with an e-folding distance of 2-scale heights until between 75 and 80 km. Above that altitude, their amplitudes are much smaller. This is confirmed by the rms perturbations $\sqrt{\sum_{i=1}^{N_p} (\rho_{1i}/\rho_0)^2}$ and of $E_p(z)$, which is proportional to $\sum_{i=1}^{N_p} (\rho_{1i}/\rho_0)^2$, shown in Figure 37. They also have a step function drop off between approximately 75 and 80 km followed by growth at close to the adiabatic rates above 80 km. The seasonal averages confirm the energy loss, but indicate it can occur over a more extended altitude region. This confirms the idea that the waves in the region above about 80 km are different from those below, and is consistent with AGWs giving up energy to the background atmosphere in the region below 80 km.

5. Summary and Conclusions

Unlike previous observations, ALO Rayleigh lidar observations cover the full mesosphere up to 90 km and span a much longer period of time. This extensive study of gravity wave activity especially in terms of gravity wave potential energy per unit mass covering the entire mesosphere is a new work. With 3-km altitude resolution and one-hour temporal resolution, waves with vertical wavelengths between 6 and ~45 km and periods between 2 and ≤ 12 hours are examined. We summarize the results as follows:

- The amplitude of the density perturbations and the mean wave potential energy per unit mass both increase at rates comparable to the adiabatic growth rates with altitude below 55–65 km and above about 75–80 km. The AGWs give up considerable energy to the background atmosphere in between these two regions.

- Seasonal fits to $E_p(z)$ over the 11 years show different variations at lower and higher altitudes. Below 70 km, there is a semiannual variation with a maximum in winter and minima in the equinoxes, whereas at the highest altitudes there is an annual variation with a maximum in winter and a minimum in summer. In both cases the maxima in $E_p(z)$ are approximately 2.5 times the minima. The greatest fall off in $E_p(z)$ relative to the adiabatic growth rate below 70 km occurs in winter. In contrast, the greatest fall off in $E_p(z)$ relative to the adiabatic growth rate above 70 km occurs in summer.
- Examination to night-to-night variability shows that it represents geophysical variability and that it is much greater than any of the seasonal variations. The largest values of $E_p(z)$ are approximately a factor of 20 greater than the smallest throughout the whole mesosphere.
- The seasonal variation in gravity wave potential energy per unit mass, with a winter maximum and summer minimum, may arise from critical-level filtering imposed by the zonal wind field [*Hines and Reddy, 1967*]. However, these data cannot rule out a seasonal variation in the sources. The minima at the equinoxes, when the zonal winds are expected to be at their weakest, do suggest that the source function are at their weakest.
- The fall off in $E_p(z)$ between 60 and 80 km relative to the adiabatic growth rates by factors between six and 18 show the importance of the mesosphere for studying critical-layer filtering, instabilities, and wave breaking.

CHAPTER 7

DECREASES IN GRAVITY WAVE POTENTIAL ENERGY WITH ALTITUDE ABOVE LOGAN, UTAH

Abstract

An extensive database of relative densities and absolute temperatures between 45 and ~90 km, i.e., over the entire mesosphere, has been acquired with the Rayleigh-scatter lidar at the Atmospheric Lidar Observatory (ALO) at the Center for Atmospheric and Space Sciences (CASS) at Utah State University (USU) in Logan, UT (41.7°N, 111.8°W). The observations are of approximately 900 nights from 1993 through 2004. Of these observations, 150 extending to 90 km were used here to examine gradual and sudden decreases of gravity wave potential energy per unit mass $E_p(z)$ with altitude relative to the adiabatic growth rate. The data were averaged over 3 km in altitude, and 1 hour or all night in time. In the all-night profiles, dips in N^2 reaching zero or negative values were found quite often; in individual 1-hour profiles, they were found even more often. These negative or zero values of N^2 were found mostly on the topside of mesospheric inversion layers where they represent the occurrence of convective instabilities. The individual 1-hour profiles showed that they often last at least two-three hours. Because of the relationship to the topside of inversion layers, they usually occurred between 70 and 80 km. Occasionally, dips occurred when there was a sharp drop in temperature on the bottom of what we are calling a negative inversion. Typically, these occurred in between 65 and 70 km. On many occasions, there was no significant correspondence between the altitudes of N^2 dips and those of the drop outs in rms density

perturbations and gravity wave potential energy per unit mass. This indicates that convective instabilities are not the main cause of the energy losses. Other possible causes might be big wind shears leading to dynamic instabilities, critical layer filtering or both.

1. Introduction

It is well known that the stability of the atmosphere plays a major role in AGW propagation. The parameter used in quantitative studies of atmospheric stability is the Brunt-Väisälä frequency, N (rad/s) and its value squared, N^2 (rad/s)². In particular, AGWs only exist when N^2 is positive, i.e., when the atmosphere is convectively stable [Hines, 1991]. When it becomes negative, the atmosphere becomes convectively unstable and AGWs cannot propagate. This parameter also provides information on the highest frequency gravity wave that the atmosphere can support. The determination of N^2 involves the temperature T , its gradient, and the differences between the actual lapse rate ($\Gamma = -\partial T/\partial z$) and the dry adiabatic lapse rate, $\Gamma_a = g(z)/c_p$, where $g(z)$ is acceleration due to gravity at altitude z and c_p is the specific heat capacity at constant pressure, 1004 J/K kg. Another instability is dynamic instability, which involves both temperature and wind shears. We will mainly focus on convective stability in this chapter.

Because of its ability to measure profiles of absolute temperature, Rayleigh-scatter lidar is an excellent method for studying convective instability throughout this region or, more specifically, between 45 and 90 km for the current lidar at the ALO at USU. In examining mesospheric inversion layers, both *Hauchecorne et al.* [1987] and *Whiteway et al.* [1995] found occasions when the lapse rate on the topside of some inversion layers

approached the adiabatic lapse rate or became superadiabatic, i.e., when N^2 became zero or less than zero. The search for convective instability was extended to much shorter time scales and much smaller altitude intervals by *Sica and Thorsley* [1996]. On the one day they examined, they found many cases of convective instabilities.

A common understanding is that when gravity waves reach the region of zero or negative N^2 (i.e., convective instability) they break and give up their energy and momentum to the surrounding atmosphere [*Hodges*, 1967; *Lindzen*, 1981]. Simultaneous study of the variation of N^2 and of gravity wave potential energy per unit mass, E_p , with altitude with the ALO Rayleigh lidar data set would be very helpful for examining this understanding. To our knowledge this type of comparison has not been made previously. Chapter 6 showed that on average the variation of E_p with altitude could follow one of three problems. It could grow with altitude as expected for adiabatic growth. Then at some altitude it could fall off very sharply compared to the adiabatic growth profile, or it could fall off gradually. This leads us to see what we can learn by examining N^2 and E_p profiles simultaneously on individual days.

In this chapter, we examine N^2 and E_p profiles to see if zero or negative N^2 coincide with a reduction in E_p . In addition, we look for other variations. Are there regions where E_p falls off sharply or gradually? If so, what else characterizes these situations. The measurements and method of analysis are presented in section 2, examples of the observations are presented in section 3, results are discussed in section 4, and conclusions are given in section 5.

2. Measurements and Method of Analysis

The Rayleigh scatter-lidar system at ALO is located in Logan, Utah, on the USU campus (41.74°N, 111.81°W), 1.47 km above sea level. It was operated from late 1993 through 2004, giving rise to an extensive database of nighttime mesospheric profiles of relative densities and absolute temperatures. The ALO Rayleigh lidar is a vertically pointing, coaxial system. It consists of a frequency-doubled Nd:YAG laser, operating at 30 Hz, generating 18–24 watts at 532 nm, and having a 44-cm diameter Newtonian telescope. The signal from below ~18 km is blocked by a mechanical chopper and below 38 km the detector gain is reduced by almost 10^3 by an electronic gate. This setup produces good data from 45 km to approximately 90 km. A narrow-band interference filter (1 nm) is used to remove most of the background light from stars, moon, airglow, and scattered city lights. The single, gated detector is a green-sensitive, bialkali photomultiplier tube (Electron Tubes 9954B) in a Peltier-cooled housing. A more extensive description of this system is given by *Beissner* [1997], *Wickwar et al.* [2001], *Herron* [2004, 2007], and *Herron and Wickwar* [2009a].

A total of more than 900 nights of observations were collected. Of these all-night profiles, 150 extend to 90 km or above. They were selected and examined to look for cases of zero, negative or small N^2 values; decreases in the root mean square relative density perturbation (rms density); and decreases in E_p . The data on these clear nights were collected continuously for periods of 4 to 12 hours. The recorded raw data is in the form of photon-count profiles with an altitude resolution of 37.5 m (250-ns sampling interval) from the ground to 500 km and a temporal resolution of 2 minutes (3600 laser pulses). The data of interest for this study start at 45 km. At each altitude z the observed

photon-counts are the sum of a background signal (from the detector, moon and starlight, airglow and scattered city lights) and the signal of interest from the backscattered laser pulse. The background signal is determined near 120–180 km and subtracted from the total. The remaining signal, multiplied by the square of the range from the laser, is proportional to the atmospheric number density $n(z)$ assuming a constant mean-molecular mass m and, hence, composition in the portion of the atmosphere we are interested in. However, the constant of proportionality may vary from one 2-minute profile to the next because of variations in the atmosphere's transmittance or changes in the power of the laser. To reduce the influence of signal fluctuations caused by these effects, the profiles were normalized to unity at 45 km. Before doing so, the data were averaged over 3 km (81 sampling intervals) and over the night. Temperatures are determined from these relative densities by using hydrostatic equilibrium and the ideal gas law. The details, as applied to this lidar, are reviewed by *Beissner* [1997], *Wickwar et al.* [2001], *Herron* [2004, 2007], and *Herron and Wickwar* [2009a]. The temperatures $T(z)$ are the sum of two terms:

$$T(z) = T(z_{\max}) \frac{n(z_{\max})}{n(z)} + \frac{1}{kn(z)} \int_z^{z_{\max}} m(z')g(z')n(z')dz'. \quad (7.1.1)$$

The integration runs from the altitude of interest z to the maximum altitude z_{\max} at which $T(z_{\max})$ is the supplied initial value. k is Boltzman's constant and $g(z)$ is the gravitational acceleration.

To calculate the absolute temperature, an *a priori* value of the temperature $T(z_{\max})$ at the start of the downward integration is necessary. The initial values were

taken from the 8-year climatology from the sodium lidar at Colorado State University (CSU) [She *et al.*, 2000], which is only 575 km away and just over 1° equatorward of ALO. The CSU temperatures were from 1990 to 1999, covering much of the same time period as the ALO data. The use of this nearby climatology should be more appropriate than using an empirical model, especially in view of the comparisons discussed in Herron and Wickwar [2009b]. In any case, any systematic error from this initial temperature decreases rapidly with the downward integration. For instance, the difference between the initial and actual temperatures decreases by a factor of ~ 4 after 10 km of integration. The starting altitude z_{\max} for the temperature integration is usually determined as the point where the signal is 16 times its standard deviation. For this analysis it is the lower of that calculation or 95 km.

At the upper limit of the lidar's range, the background becomes a large portion of the total signal. Its accurate determination in the region above 120 km is most important for the data selection, because a bad background leads to systematic temperature errors at all altitudes [Herron, 2004]. Observationally, bad backgrounds can have slopes, oscillations, or spikes. To minimize potential background problems, the background region was chosen specifically for each night and each night reduced separately. Subsequent averaging of many nighttime temperatures further reduces any adverse effects from the background selection. The temperature profiles used here are included in the Herron and Wickwar [2009a] climatology, i.e., this is not a new (and different analysis) of the data.

Using these derived absolute nightly averaged temperature profiles $T(z)$ the temperature gradient profiles $\partial T(z)/\partial z$ were calculated by applying the IDL numerical

differentiation routine, which uses three-point, Lagrangian interpolation. The corresponding nightly averaged $N^2(z)$ profiles were calculated according to

$$N^2(z) = \frac{g(z)}{T(z)} \left[\frac{\partial T(z)}{\partial z} + \frac{g(z)}{c_p} \right], \quad (7.1.2)$$

where c_p is the specific heat capacity at constant pressure, which is $1004 \text{ J K}^{-1} \text{ kg}^{-1}$, and

$g(z)/c_p$ is the dry adiabatic lapse rate $\Gamma_a(z)$, which is 9.8 K/km at sea level.

The variance for the $N^2(z)$ profiles were calculated according to

$$\sigma_{N^2}^2 = \left(\frac{N^2(z)}{T(z)} \right)^2 \sigma_T^2 + \left(\frac{g(z)}{T(z)} \right)^2 \sigma_{\frac{\partial T}{\partial z}}^2, \quad (7.1.3)$$

where σ_T^2 is the temperature variance, which is derived analytically from equation (7.1.1)

by propagating the uncertainty in the photon counts [e.g., *Gardner*, 1989; *Beissner*, 1997;

Herron, 2004, 2007]. The temperature gradient variance, $\sigma_{\frac{\partial T}{\partial z}}^2$, is calculated using the

IDL routine. The covariance term for $\sigma_{N^2}^2$ were examined, but do not make a significant contribution. Consequently, we treated $T(z)$ and $\partial T(z)/\partial z$ as independent.

An individual measured density profile is represented by $\rho(z) = \rho_0(z) + \rho_1(z)$, where $\rho_1(z)$ is the wave-induced density perturbation and $\rho_0(z)$ is the background mean state of the atmosphere (i.e., the unperturbed density profile). The background density profile is first estimated by least squares fitting a sixth order polynomial to the logarithm of the all-night averaged density profile. The deviation of the measured profile $\rho(z)$ from the background profile $\rho_0(z)$ provides the density perturbation profile $\rho_1(z)$

and the fractional density perturbation profile $\rho_1(z)/\rho_0(z)$. These perturbations represent the combined effects of waves and of statistical fluctuations (uncertainty) from the photon-counting process. Therefore, the actual variance of atmospheric density fluctuations at a given altitude, z , is

$$\overline{\left[\frac{\rho_1(z)}{\rho_0(z)}\right]^2} = \frac{1}{N_p - 1} \sum_{i=1}^{N_p} \left[\frac{\rho_{1i}(z)}{\rho_0(z)}\right]^2 - \frac{1}{N_p} \sum_{i=1}^{N_p} \frac{\sigma_{\rho_i}^2(z)}{\rho_0^2(z)} \quad (7.1.4)$$

[*Whiteway and Carswell, 1995*], where N_p is the number of 1-hour profiles used and $\sigma_{\rho_i}^2(z)$ is the noise variance associated with the relative density uncertainty arising from the Poisson measurement uncertainty. The perturbation profiles ρ_{1i} are calculated from 1-hour individual density profiles.

This profile of the variance of the relative density perturbations is then used to determine the profile the average potential energy per unit mass $E_p(z)$, which is given by

$$E_p(z) = \frac{1}{2} \left[\frac{g(z)}{N(z)} \right]^2 \overline{\left[\frac{\rho_1(z)}{\rho_0(z)} \right]^2} \quad (7.1.5)$$

[e.g., *Mitchell et al., 1991*; *Wilson et al., 1991b*; *Whiteway and Carswell, 1995*].

The variance associated with $E_p(z)$ uncertainty arising from measurement, i.e., $\sigma_{E_p}^2$, is determined as in equation (6.1.15) given in Chapter 6.

The observed values of the rms relative density perturbations and $E_p(z)$ are also compared with the corresponding values that are growing adiabatically. The values for the adiabatic growth for rms relative density perturbations $\sqrt{\overline{[\rho_1(z)/\rho_0(z)]_G^2}}$ and potential energy per unit mass $E_G(z)$ are calculated as

$$\sqrt{[\rho_1(z)/\rho_0(z)]_G^2} = \sqrt{[\rho_1(z_0)/\rho_0(z_0)]^2} \exp(\Delta z/2H_\rho) \quad (7.1.8)$$

$$E_G(z) = E_p(z_0) \exp(\Delta z/H_\rho), \quad (7.1.9)$$

where $\Delta z = z - z_0$ and $H_\rho = \left(\frac{1}{H} + \frac{1}{T} \frac{dT}{dz} \right)^{-1}$ is the density scale height and $H = kT/mg$ is the pressure scale height. In the figures that we will discuss, we arbitrarily normalize the rms density and E_G values at 45 km to 1.5% and 10 J/kg, respectively.

3. Examples of the Observations

Examples of the simultaneous analysis of temperatures, $N^2(z)$, rms relative density perturbations, and $E_p(z)$ between 45 and 90 km are shown for individual days in Figures 39 through 45. These examples include both winter and summer days. In the winter profiles for February 19, 1995 in Figure 39, N^2 values for all 1-hour profiles in Figure 39b are positive below about 75 km. However, for short intervals between 75 and 80 km N^2 values for many of the profiles are negative, and the altitudes of those negative N^2 regions agree well with the topside of the temperature inversions with the biggest lapse rates seen in the individual temperature profiles in Figure 39a. This good altitude agreement continues for the all-night profiles of temperature and N^2 in Figures 39c and d. In Figure 39c the dashed green curve represents the dry adiabatic lapse rate Γ_a . Between 81 and 83 km Γ is very close to Γ_a , and N^2 is negative between 81 and 82 km. Figures 39e and 39f show the corresponding profiles of rms density and $E_p(z)$. In both of them the two biggest drop outs occur at 71 and 84 km. Accordingly, the negative

N^2 values do not occur at the same altitudes as dips in the rms density or $E_p(z)$. Quite the contrary, the dip at 71 km corresponds where N^2 has a maximum on the bottomside of the inversion layer. The adiabatic growth curves for rms density and $E_p(z)$ calculated using equations (7.1.8) and (7.1.9) are shown as black thick solid curves for comparison. Below approximately 65 km, the rms density and $E_p(z)$ grow adiabatically. Between 65 and 73 km they give up two thirds of their energy to the surrounding atmosphere in what looks like a gradual step function. Above 73 km, they again grow adiabatically. Something significant happens in this small region where the wave energy falls off dramatically and where N^2 appears to have a relative maximum on the bottomside of an inversion layer.

Examples of summer days are shown in Figures 40 and 41. In the summer profiles of July 23, 1996 in Figure 40, N^2 values for all 1-hour profiles in Figure 39b are positive below about 75 km. However, for short intervals between 75 and 80 km N^2 values for many of the profiles are negative, and the altitudes of those negative N^2 regions agree well with the topside of the temperature inversions with the biggest lapse rates seen in the individual temperature profiles given in Figure 40a. The 1-hour temperature profiles vary considerably affecting the lapse rate and the occurrence of negative N^2 . Unlike the winter example, the averaged temperature inversion for the all-night temperature profile in Figure 39c is smaller and Γ between 77 and 80 km, while big, is not as big as Γ_a . As a result N^2 has a big dip but does not drop to zero, Figure 40d. Instead the big dip in rms density and E_p in Figures 40e and f occurs at 72 km, about 1 km below a relative maximum in N^2 on the bottomside of the inversion layer. This dip at 72 km is not an

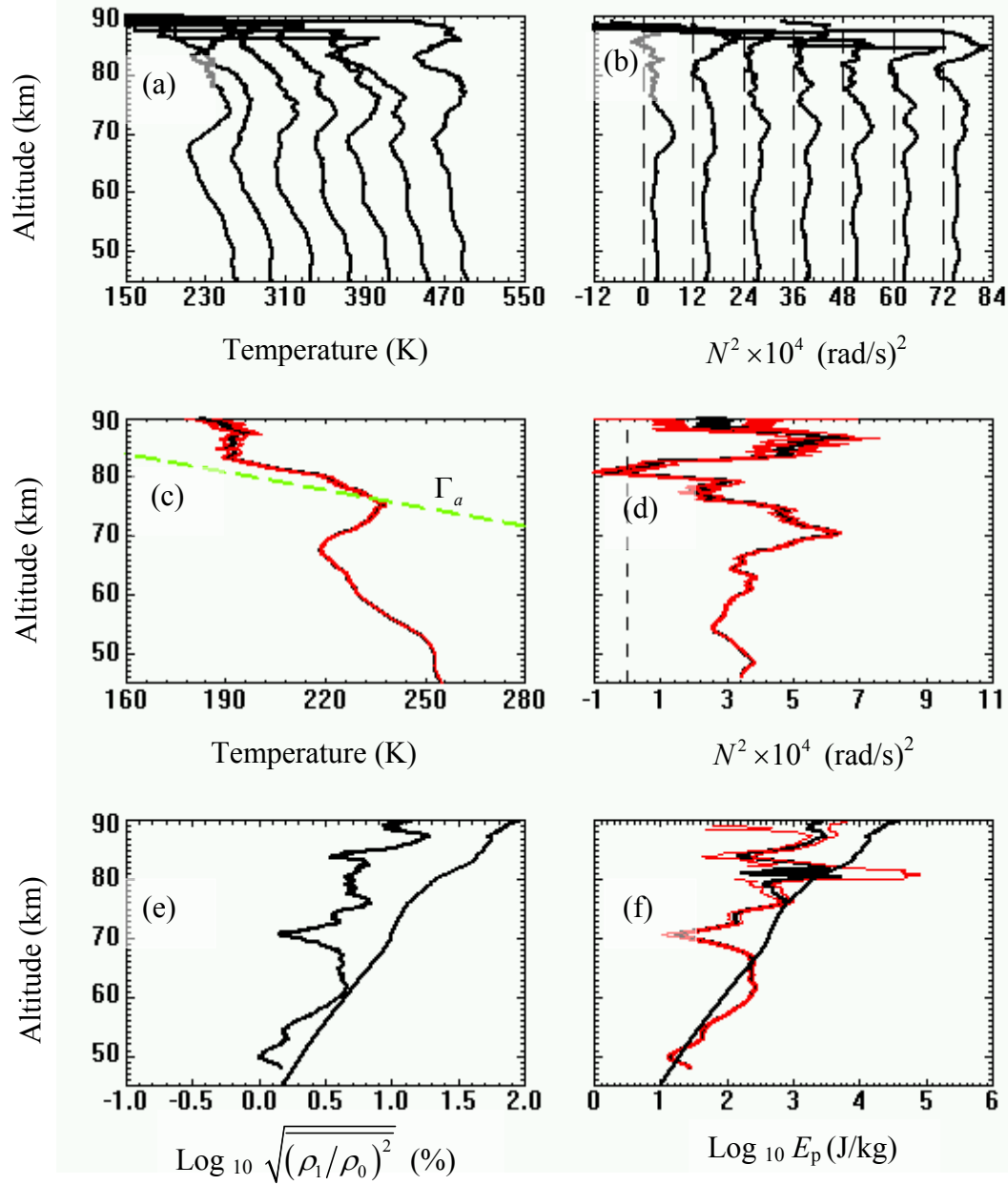


Figure 39. Behavior of several parameters on the night of February 19, 1995. (a) Individual 1-hour temperature profiles. Each profile is offset by 40 K. (b) Individual 1-hour N^2 profiles. Each profile is offset by 12 $(\text{rad/sec})^2$. (c) All-night temperature profile. (d) All-night N^2 profile. (e) rms relative density profile. (f) All-night E_p profile.

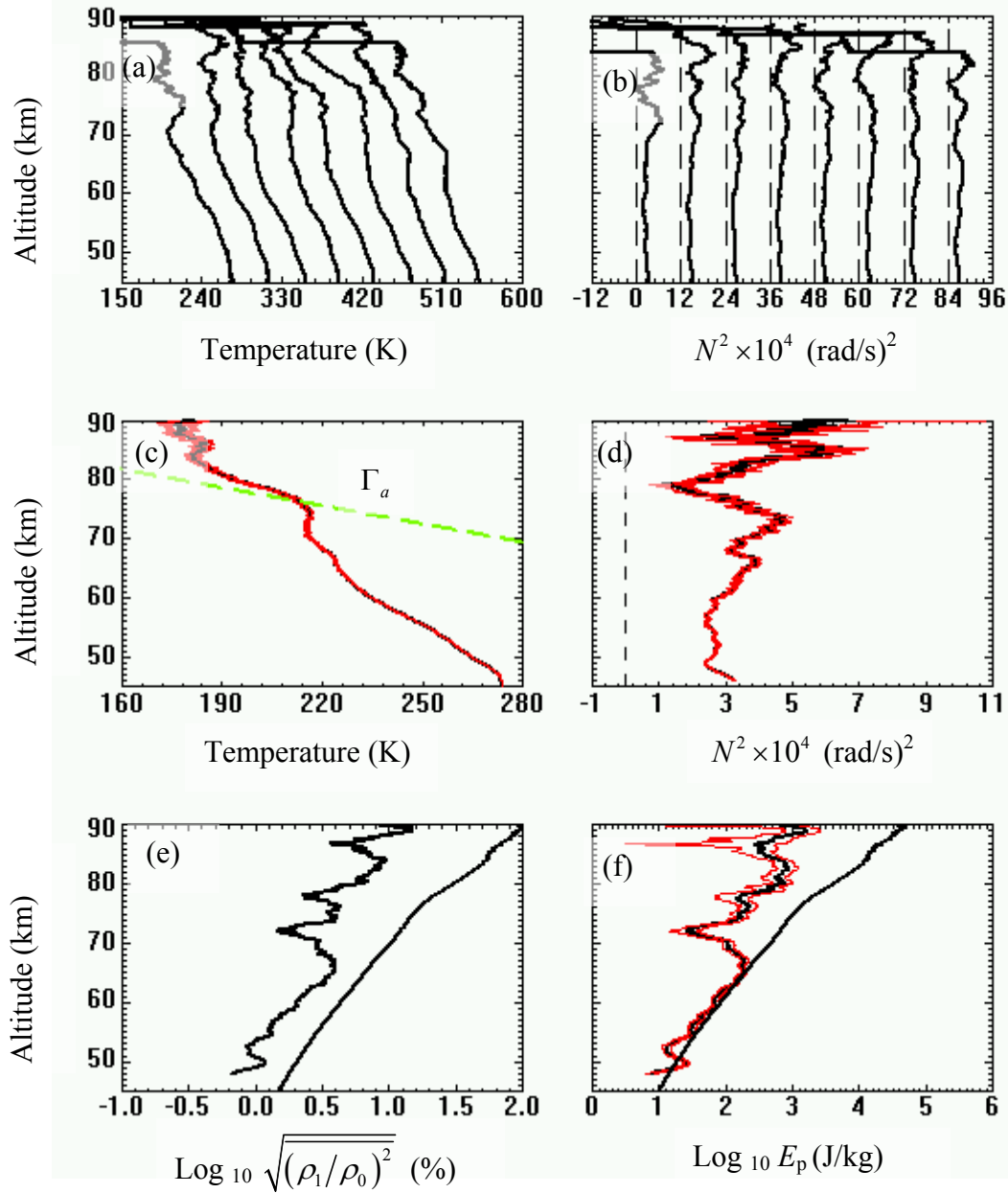


Figure 40. Behavior of several parameters on the night of July 23, 1996. (a) Individual 1-hour temperature profiles. Each profile is offset by 40 K. (b) Individual 1-hour N^2 profiles. Each profile is offset by 12 (rad/sec^2). (c) All-night temperature profile. (d) All-night N^2 profile. (e) rms relative density profile. (f) All-night E_p profile.

isolated event. These two measurements of wave activity lose about 80% of their value compared to the adiabatic curve. Thus, considerable energy is given to the surrounding atmosphere in this region. Below 67 km and above 73 km they again grow adiabatically. As in the winter day, this gradual step function in the wave activity appears to be associated.

The following day, July 24, 1996, has a similar situation, which is presented in Figure 41 in the same format as the previous two figures. In this case two of the 1-hour N^2 profiles, those with the biggest lapse rates, dip to zero between 81 and 82 km. The all-night average profile of N^2 has a major dip at 80 km, but does not reach zero. The altitude of that dip coincides with the biggest lapse rate on the topside of the inversion layer in the all-night temperature profile. Neither the rms relative density perturbation nor E_p has a major dip at 80 km. Instead, they have a major dip centered at 71 km. Between 65 and 72 km, these measures of wave activity lose approximately 85% of their value relative to the adiabatic growth curves, in what looks like a gradual step function. Below 65 km and above 72 km, these measures of the wave activity follow their respective adiabatic growth curves. Unlike this similar big step function decrease on the previous two days, this one is not associated with a relative maximum in the all-night N^2 profile and the bottom side of the inversion layer. Instead it occurs at an altitude where one (out of seven) of the 1-hour N^2 profiles has a dip reaching zero and the corresponding temperature profile has a very large lapse rate. This leads to a small dip in the all-night N^2 profile.

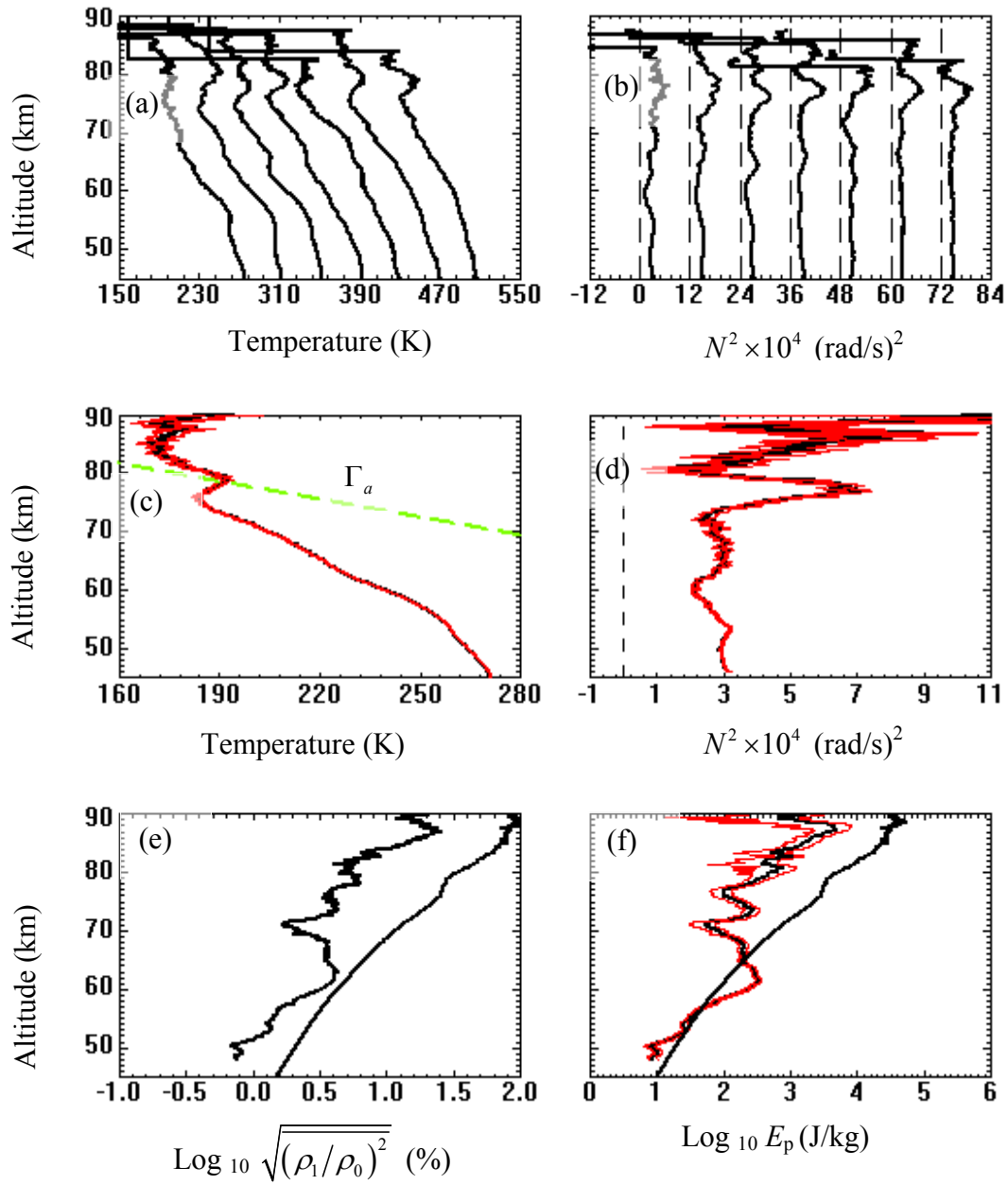


Figure 41. Behavior of several parameters on the night of July 24, 1996. (a) Individual 1-hour temperature profiles. Each profile is offset by 40 K. (b) Individual 1-hour N^2 profiles. Each profile is offset by 12 $(\text{rad/sec})^2$. (c) All-night temperature profile. (d) All-night N^2 profile. (e) rms relative density profile. (f) All-night E_p profile.

Other summer examples in Figures 42-44 show a similar, yet very different situation to what is shown in Figures 39-41. These are the negative inversions. N^2 values for all 1-hour profiles in Figures 42b, 43b and 44b are positive below about 72 km. However, between about 72 and 77 km N^2 values for many of the 1-hour profiles are negative, and the altitudes of these negative N^2 regions agree well with large lapse rates on sharp temperature drops just below large, higher-altitude temperature inversions (Figures 42a, 43a and 44a). As before, the negative or zero N^2 values occur in a region with a big lapse rate. However, unlike the previous examples this big lapse rate is associated with a big drop in temperature just below an inversion layer instead of with a big drop in temperature on the topside of an inversion layer. In contrast to a temperature inversion, we are calling this a negative inversion. This behavior shows up even more clearly in the all-night profiles of temperature and N^2 in Figures 42c, 43c, and 44c, and 42d, 43d, and 44d. But there is enough variability from hour to hour that N^2 does not quite reach zero in the all-night averages. It should be noted that this negative inversion appears on the all-night temperature profiles and on some of the 1-hour profiles approximately 5 km above a temperature fluctuation, which gives rise to an N^2 maximum. This is not what would usually be classified as an inversion layer, but it is definitely a temperature fluctuation. The combination of the strong summer lapse rate and a slight increase in lapse rate above this temperature fluctuation give rise to a lapse rate approaching the adiabatic lapse rate. These N^2 minima occur at approximately the same altitude as a small dip in the wave activity. A significant discrepancy between the adiabatic growth profiles and the observed profiles indicates that the waves are giving up energy to the surrounding atmosphere (Figures 42e-44e and Figures 42f-44f) over much

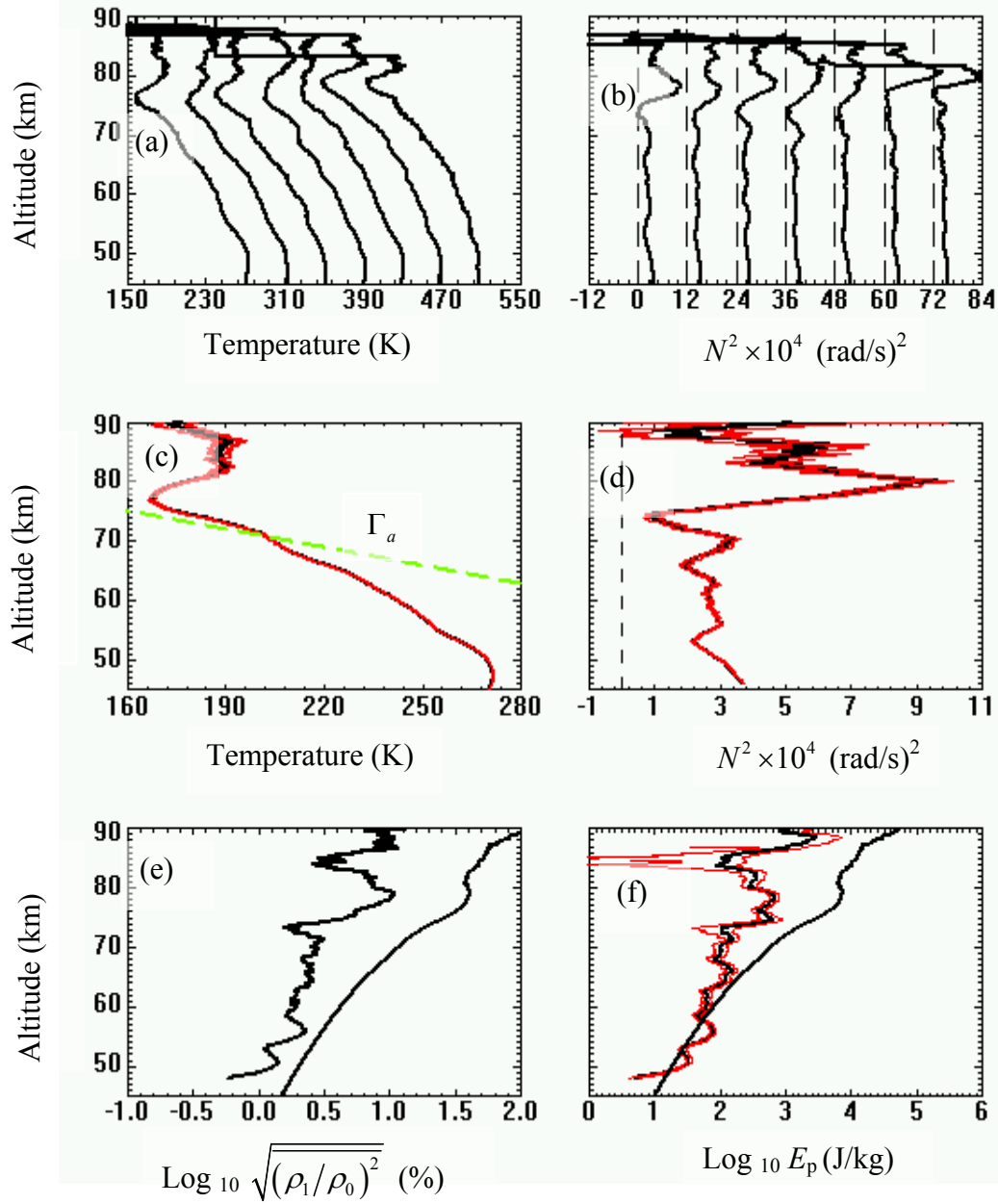


Figure 42. Behavior of several parameters on the night of July 16, 1995. (a) Individual 1-hour temperature profiles. Each profile is offset by 40 K. (b) Individual 1-hour N^2 profiles. Each profile is offset by 12 $(\text{rad/sec})^2$. (c) All-night temperature profile. (d) All-night N^2 profile. (e) rms relative density profile. (f) All-night E_p profile.

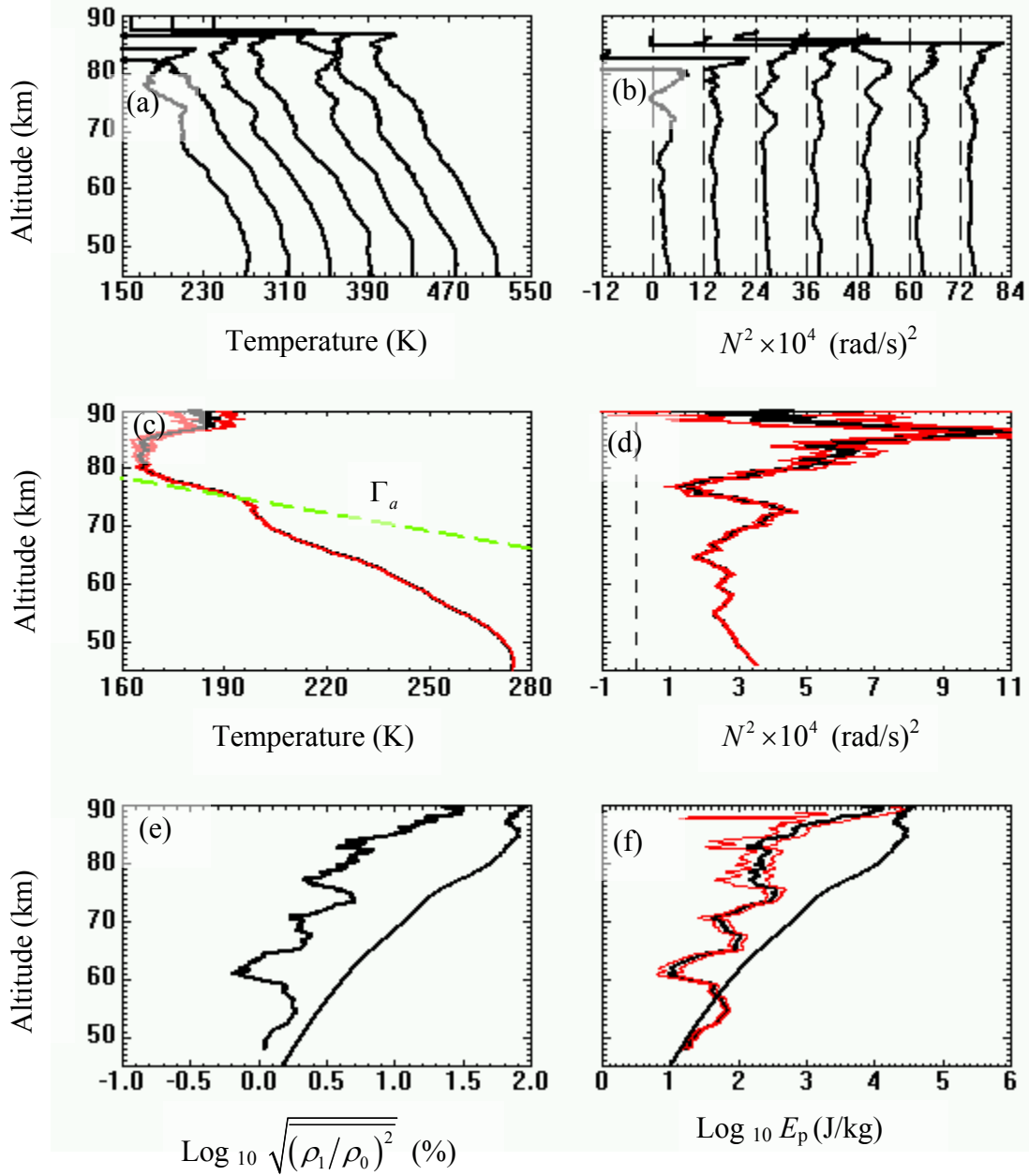


Figure 43. Behavior of several parameters on the night of June 22, 2000. (a) Individual 1-hour temperature profiles. Each profile is offset by 40 K. (b) Individual 1-hour N^2 profiles. Each profile is offset by 12 $(\text{rad/sec})^2$. (c) All-night temperature profile. (d) All-night N^2 profile. (e) rms relative density profile. (f) All-night E_p profile.

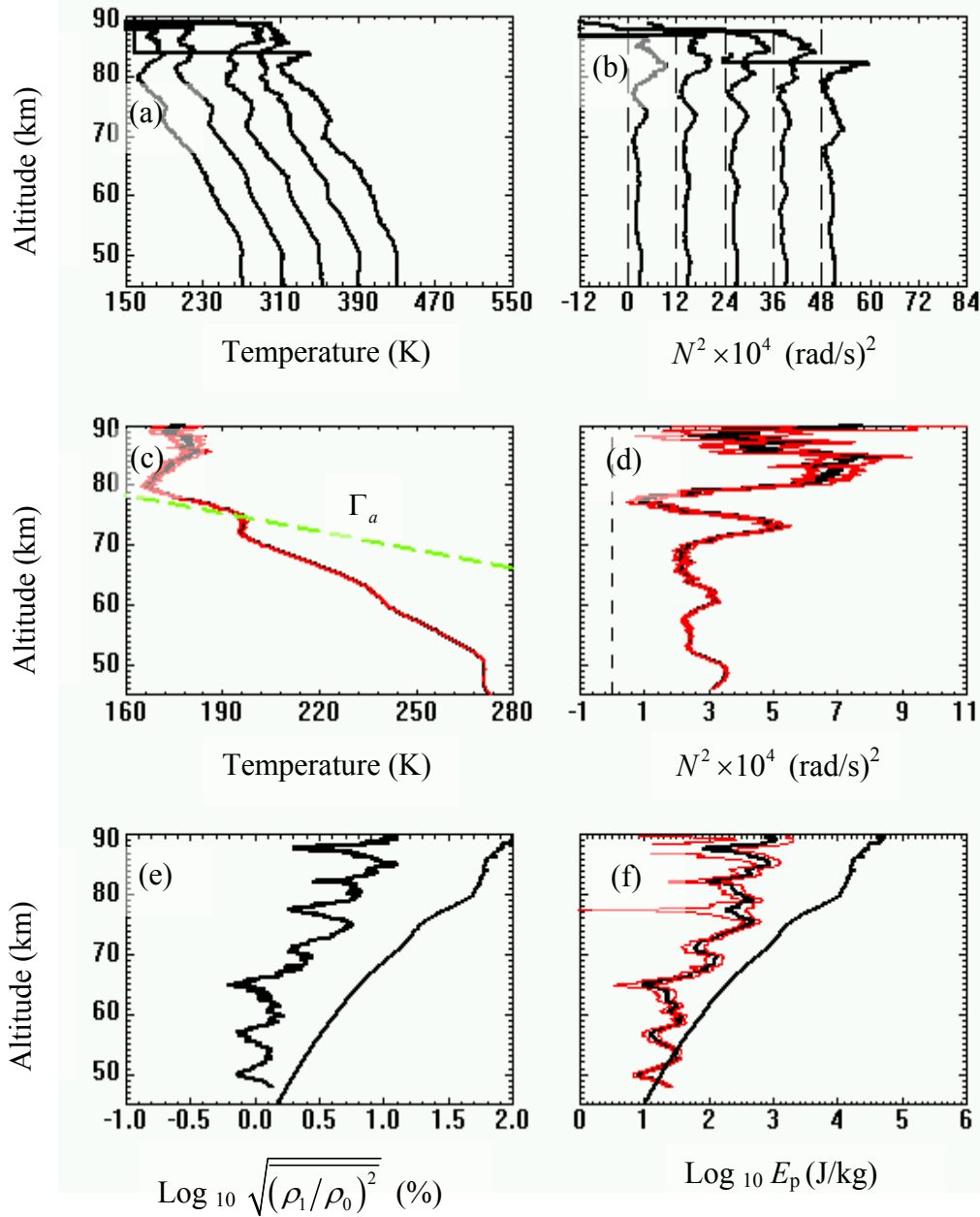


Figure 44. Behavior of several parameters on the night of July 08, 1995. (a) Individual 1-hour temperature profiles. Each profile is offset by 40 K. (b) Individual 1-hour N^2 profiles. Each profile is offset by 12 $(\text{rad/sec})^2$. (c) All-night temperature profile. (d) All-night N^2 profile. (e) rms relative density profile. (f) All-night E_p profile.

of the altitude region. Two of the three appear to have small step function decreases near 60 km, which have no particular relationship to changes in N^2 .

Similar curves are provided for an equinox day, April 7, 1995 in Figure 45. The N^2 minima (or negative N^2) for individual 1-hour profiles, as well as for the all-night profile are found to occur between 70 and 75 km. The altitudes for the 1-hour profiles in Figure 45b correspond on average to the height for the all-night averaged N^2 profile in Figure 45d and to where the temperature lapse rate is close to Γ_a in Figure 45c. They also correspond to brief dips in rms density perturbation in Figure 45e and $E_p(z)$ in Figure 45f at 71 km. Between 56 and 69 km, the adiabatic growth curves in Figures 45e and 45f are very similar to the observed profiles of density fluctuation and $E_p(z)$. This implies that the waves are growing without losing energy to the surrounding atmosphere in this small region. Going lower, another brief dip in rms density perturbation and potential energy occurs centered on 54.5 km. This also coincides with a small N^2 relative maximum. From the all-night temperature profile, Figure 45c, this occurs just above another very small temperature inversion or fluctuation. Instead, this night appears to have a series of such inversions. Perhaps they are the result of a small vertical wave. Then above 75 km the rms density perturbation and energy fall undergo a small step function decrease.

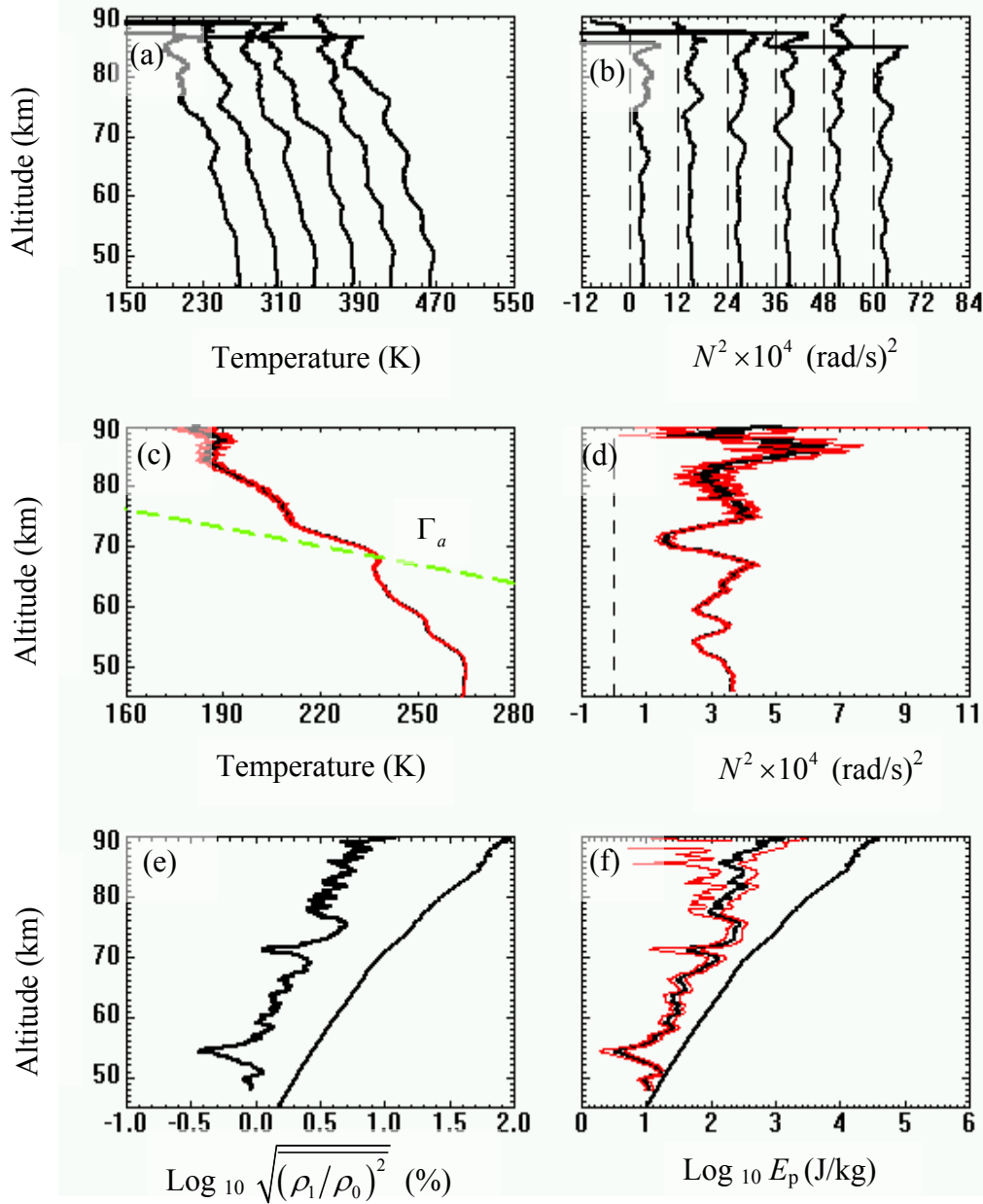


Figure 45. Behavior of several parameters on the night of April 07, 1995. (a) Individual 1-hour temperature profiles. Each profile is offset by 40 K. (b) Individual 1-hour N^2 profiles. Each profile is offset by 12 (rad/sec^2). (c) All-night temperature profile. (d) All-night N^2 profile. (e) rms relative density profile. (f) All-night E_p profile.

4. Discussion

When the lapse rate Γ is greater than the adiabatic lapse rate, Γ_a , i.e., the temperature gradient dT/dz is more negative than the adiabatic gradient, then N^2 becomes negative and several things are supposed to happen. AGWs are not supposed to propagate and the atmosphere is supposed to become convectively unstable. This would mean that gravity-wave fluctuations would cease at that altitude and only start growing again from much smaller amplitude above that region. In our observations this lapse rate condition occurs under two circumstances: on the topside of inversion layers and on what we are describing as the bottomside of negative inversion layers. The latter appear to occur in summer when there are a series of small fluctuations in the temperature profile. Eventually, there is an inversion layer. But, just below it, the lapse rate becomes particularly strong prior to becoming zero and then negative at the start of the inversion. One additional thing should happen as N^2 approaches zero. Because $E_p \propto 1/N^2$, there should be two effects on E_p . On the one hand, as N^2 becomes smaller, E_p should become bigger. On the other hand, as the waves disappear, E_p should become smaller. It is not clear which effect should dominate. However, what is clear is that E_p and rms relative density fluctuations should not vary in the same way.

These predictions can be easily compared to observation. The best profiles are the all-night profiles. While $\Gamma \geq \Gamma_a$ and $N^2 \leq 0$ occur on some of them, it is more common to have that situation for only a few hours. This should nonetheless lead to dips in N^2 followed by dips in the rms relative density fluctuations, and some sort of fluctuation in E_p . Part of the time there is no response to an N^2 dip, and part of the time

there are small dips, but not a step function, in both the rms relative density fluctuations and E_p . Thus the observations do not correspond to the predictions.

A likely explanation comes from examining altitude ranges. When $N^2 \leq 0$, this occurs over an altitude range that is less than 3 km. Whereas, we are most sensitive to vertical wavelengths greater than 6 km and the dominant vertical wavelengths we found from examining monochromatic gravity waves (Chapter 5) are 12–16 km. Thus it appears that the AGWs to which we are sensitive can propagate across a narrow region of $N^2 \leq 0$ with minimal effect. Perhaps we see no effect when the vertical wavelengths are long and a small effect when the vertical wavelengths are shorter.

The above discussion centers on dips in N^2 . However, there are also relative maxima in the N^2 profiles, which occur on the bottomside of inversion layers when Γ is negative. When this occurs we would predict no change in the rms relative density fluctuations and possibly a small dip in E_p because of $E_p \propto 1/N^2$. However, what is observed is that sometimes there is no dip in either of these variables, sometimes there is a small dip in both of them, and sometimes there is a step function decrease relative to the adiabatic growth rates. (The third effect is discussed in the next paragraph.) The fact that the rms relative density fluctuations have a dip suggests that something else is happening besides an increase in N^2 , something that would reduce the AGW fluctuations. It would have to be something that occurs over a limited altitude region and is independent of density or temperature.

Observationally, the other characteristic that appears often in the profiles is a gradual step function decrease in both the rms relative density fluctuations and E_p with

increasing altitude relative to the adiabatic growth rates. The observed decreases in E_p range from a factor of 3 to a factor of 20. This is much like what was observed in the seasonal averages in Chapter 6. Sometimes this occurred when nothing special appeared to be happening in the N^2 profile. Other times, N^2 was close to a relative maximum. Possibly this could occur because of dynamic instabilities. But they usually occur when N^2 is small and there is a significant velocity shear. While the Rayleigh data are not sensitive to the background winds, these occurrences are not when N^2 is particularly small. Accordingly, this interpretation seems unlikely. Another possible interpretation involves filtering by critical layers. This part of the mesosphere does have variations with altitude of the background winds and superimposed on them winds from tides and planetary waves. Furthermore, some of these tidal or planetary waves have been invoked as being involved in generating inversion layers. Usually a discussion of critical-layer filtering assumes that the AGWs give up all their energy and momentum to the background wind. But, as in our discussion of what happens for $N^2 \leq 0$, there may be a question of scale lengths. Possibly a critical layer could be thin enough compared to the vertical wavelength that the wave is only partially damped, something like an evanescent wave.

5. Conclusions

This is the first extensive examination of AGW behavior in the mesosphere of a number of individual days of which we are aware. Previously, in Chapter 6, we examined average behavior, finding significant fall off in gravity wave potential energy per unit mass with altitude relative to the adiabatic growth rate curves. The magnitude

and altitude of this fall off varied with season. In this paper we looked individually at the 150 nights used in the averages to search for explanations. We expanded the descriptions of what occurred but did not find simple explanations in terms of gravity wave theory.

- On most nights there were 2–3 hours when $N^2 \leq 0$ over an altitude region less than 3 km in width. Sometimes $N^2 \leq 0$ would extend to the whole night, but usually it would lead to a significant dip in the all-night averages.
- $N^2 \leq 0$ occurred on the topside of inversion layers and on the bottomside of negative inversion layers.
- Instead of the wave activity, as judged by rms relative density fluctuations and E_p , disappearing under these conditions, there would be at most small dips in these measures. It is suggested that this might happen because $N^2 \leq 0$ occurred in a thin region while the waves to which the lidar was sensitive and which it saw had much longer vertical wavelengths.
- Although not expected, unless because of winds to which the lidar was not sensitive, dips and step function decreases in rms relative density fluctuations and E_p were sometimes found when N^2 had a relative maximum on the bottomside of an inversion layer where $\Gamma < 0$.
- Step function decreases in rms relative density fluctuations and E_p relative to the adiabatic growth rates were found on many occasions, but not in relation to any significant features in the temperature or N^2 profiles. These decreases amounted to factors of 3–20. It is suggested that these might be related to critical layer filtering from thin regions compared to the AGW vertical wavelength where the

horizontal phase velocity matched the horizontal winds. The effect might then be like that of an evanescent wave that only lost part of its amplitude.

CHAPTER 8

SUMMARY AND FUTURE WORK

1. Summary and Conclusions

For this research we used the extensive observations acquired with the Rayleigh-scatter lidar at the Atmospheric Lidar Observatory (ALO) at the Center for Atmospheric and Space Sciences (CASS) at Utah State University. This lidar technique is the only ground-based technique that can probe the whole mesosphere from 45 to 90 km. The observations were of 900 nights from 1993 through 2004. Of these profiles, 150 extend to 90 km or above and they were the ones used in this study. The Rayleigh backscatter returns provide profiles of relative neutral density and absolute temperature. Most of the results presented here are new because, unlike previous observations, ALO Rayleigh lidar observations include more nights and a greater altitude range, especially adding the region between 60 or 70 km and 90 km of the mesosphere. With these extensive measurements we examined four aspects of AGWs.

1) The Brunt-Väisälä (buoyancy) angular frequency N (rad/s) is the maximum frequency (minimum period) of AGWs. The buoyancy frequency squared N^2 (rad/s)² is one of the most important stability parameters in the atmosphere. AGWs can only propagate as long as N^2 remains positive (i.e., the atmosphere is stable). When it becomes negative, the atmosphere becomes convectively unstable and they cannot propagate. Detail study of this basic parameter is essential for understanding the AGW phenomena in the atmosphere. This was the first part of this research. Using the nighttime average temperature profiles and their temperature gradients, the N^2 profiles were

calculated. A climatology of N^2 for a composite year was obtained by averaging all the nighttime N^2 profiles over a 31-day window spanning 11 years centered on each day. The minimum and maximum values of N^2 over the entire mesosphere vary between $2.2 \times 10^{-4} \text{ (rad/s)}^2$ and $9.0 \times 10^{-4} \text{ (rad/s)}^2$, respectively. The corresponding buoyancy periods vary between 7.0 minutes and 3.5 minutes. From these extensive observations involving considerable averaging, it is learned that the atmosphere above Logan, Utah, on average, is convectively stable. We found a clear seasonal variation in N^2 profiles with up to 30% larger values during winter than summer below 75 km and larger values during summer than winter above 75 km. This reversal agrees well with a downward phase progression in the annual and semi-annual variations of N^2 . The geophysical variability in N^2 grows rapidly with altitude with the same e-folding distances as for the geophysical variability in temperature, strongly suggesting that the N^2 variability arises from the growth of waves with altitude. Many of the main features in the N^2 climatology can be related to climatological temperature profiles, their gradients, and the growth of wave activity with altitude. This mid-latitude, mesospheric N^2 climatology, based on extensive mesospheric temperature measurements, is a significant improvement over previous climatologies. It is most applicable to situations involving the average behavior of the mid-latitude mesosphere.

2) Of the techniques capable of measuring gravity-wave parameters at middle-atmospheric heights, only the Rayleigh-lidar approach has provided successive profiles that cover the entire mesosphere above a single location over periods of several hours. Lidar studies of gravity wave activity often concentrate on observations of monochromatic structures, because they appear clearly in almost all lidar profiles. A

detailed examination of profiles of relative density perturbations shows the presence of monochromatic gravity wave motions in the mesosphere (45-90 km). These waves were found on almost every night examined. Sometimes they exist for only 2 to 3 hours, other times for the whole night, up to 10–12 hours. They often become less distinct, but more complex, above about 80 km. For instance, we see many waves with an upward phase velocity in the region above 80 km, but almost none in the region below. Thus, there appears to be a change in the AGW population at approximately 80 km. Vertical wavelengths and vertical phase velocities are the two observed parameters. Below 80 km, we found the AGWs with vertical wavelengths ranging from 6 to 19 km, with the most frequent values being between 12 and 16 km. We did not find significant seasonal variation in the vertical wavelength. The minimum and maximum values of vertical phase velocities observed are 0.2 to 1.0 m/s (0.72 km/hr to 3.5 km/hr). The most frequent phase velocities in winter are 0.5 m/s (1.8 km/hr) and in summer 0.6 m/s (2.2 km/hr). Thus there appears to be a significant difference between the summer and winter AGW populations. This difference may be related to filtering, sources, or both.

Using these observed parameters, buoyancy periods, and AGW dispersion relations, which are based on linear gravity wave theory, other gravity wave parameters were derived. The values of horizontal wavelengths range from ~160–3,100 km, with 550–950 km being the most prevalent. The horizontal phase velocities range from 24–53 m/s (85–190 km/hr), with 32–35 m/s (120–130 km/hr) the most prevalent. Most of these monochromatic gravity waves are generated between ~1500 km and ~ 4500 km from ALO, and often from a very extended region. The extent of the source region can be determined from the duration of a gravity wave event or from its altitude extent.

Assuming an 8-hour event and average vertical and horizontal speeds, the horizontal extent is a minimum of 1000 km and could be more than 3000 km. In either case the source region is huge and has to last a long time. This puts limits on what the source can be. We suggest a weather system.

3) We examined the atmospheric gravity wave activity in terms of the gravity wave potential energy per unit mass $E_p(z)$ carried by these waves into the mesosphere from below. We examined the temporal and altitude variation of $E_p(z)$ and found that $E_p(z)$ is highly variable from day to day, by almost a factor of 20 throughout the mesosphere. This implies major day-to-day differences in the sources, the filtering process, or both. A study of seasonal variability shows different behaviors at lower and higher altitudes. Below 70 km, there is semiannual variation with a maximum in winter and minima in the equinoxes, whereas at higher altitudes there is an annual variation with a maximum in winter and a minimum in summer.

As atmospheric gravity wave linear theory predicts, the amplitude of AGW perturbations grow with altitude exponentially with an e-folding distance of 2-scale heights, approximately 14 km, and the potential energy per unit mass grows exponentially with an e-folding distance of 1-scale height, approximately 7 km. We found that the amplitude of the density perturbations and the mean wave potential energy per unit mass both increase with altitude approximately at the adiabatic rates below 55 to 65 km and above 75 to 80 km. The AGWs give up considerable energy to the background atmosphere in the intervening region. This raises questions about finding the causes for this energy loss and finding the impact of this energy loss on the background atmosphere.

4) This study examines individual days to search for the causes of the large loss of AGW potential energy per unit mass to the background atmosphere. One possibility is convective instability. It occurs in those regions where the temperature lapse rate $\Gamma = -\partial T/\partial z$ is larger (the gradient more negative) than the dry adiabatic lapse rate ($\Gamma_a = 9.8 \text{ K/km}$), which also implies that $N^2 < 0$. We examined the all-night and individual 1-hour N^2 profiles along with the corresponding temperature profiles for the 150-night data set to find and investigate these occurrences. In the all-night profiles, we often found N^2 dips. The dips are found more often in individual 1-hour profiles. They are usually deeper and often negative for 2 to 3 hours. These dips usually occur on the topside of mesospheric inversion layers, but they also occur on the bottomside of what we are calling negative inversion layers.

It is expected that the wave activity as judged by rms relative density fluctuations and potential energy per unit mass E_p would disappear when a convective instability (i.e., $N^2 < 0$) occurs. Above that altitude, the wave activity might start to grow again. Instead what is observed is at most small dips in these wave parameters. It is suggested that this might happen because $N^2 \leq 0$ occurred in a thin region while the waves to which the lidar is sensitive and which it saw have much longer vertical wavelengths. On some occasions, particularly during summer (June and July), various N^2 profiles had relative maxima on the bottomside of the inversion layer where $\Gamma < 0$. Although not expected, unless because of winds to which the lidar was not sensitive, dips and step function decreases in rms relative density fluctuations and E_p relative to the adiabatic growth rates were sometimes found in these regions. However, such decreases were not

unique to these regions. They were found on many occasions, but not in relation to any significant features in the temperature or N^2 profiles. These decreases amounted to factors of 3–20. It is suggested that these might be related to critical layer filtering from thin regions compared to the AGW vertical wavelength where the horizontal phase velocity matched the horizontal winds. The effect might then be like that of an evanescent wave that only lost part of its amplitude while crossing a forbidden region.

In conclusion, there are various unique features of this research.

- This work on AGWs is a new area of research within the ALO group as we used extensive data set covering the entire mesosphere (45–90 km) and examined more AGW parameters that had been looked at previously.
- This research includes the region below 80 km that is not accessible by other ground-based techniques. It extended previous Rayleigh-lidar studies upward above 60–70 km and used a much more extensive data set.
- As apparent from our results, this region, covering the entire mesosphere, is very important for understanding atmospheric gravity wave activity, especially their growth and dissipation.
- An extensive study of the Brunt-Väisälä frequency (period), a very crucial parameter in gravity wave studies, was a logical starting point and has not been done before. Comparison with values derived from the NRL-MSISE00 model, which showed significant differences, indicate the importance of this study. These differences in the Brunt-Väisälä frequencies include those that arise because the lidar data include mesospheric inversion layers and a very significant semiannual variation, which are missing from the model.

- Because the ALO lidar data cover the whole mesosphere, it was possible to determine the vertical wavelength and vertical phase velocity of atmospheric gravity waves in this region. Combining these parameters with the gravity wave dispersion relation enabled us to determine the horizontal gravity wave parameters. Furthermore, because the background vertical winds are expected to be small compared to the vertical phase velocities, all the values for the derived AGW parameters are very close approximations to the intrinsic values.
- With this extensive database, we found a clear seasonal variation in vertical phase velocity with larger values in summer and smaller in winter, which has never been reported before. This observed difference suggests a significant difference between summer and winter gravity wave populations, which could arise because of differences in filtering, the sources, or both. The source region was found to be thousands of kilometers away and to extend over a thousand or so kilometers. This was a new and unexpected result.
- A question may arise as to whether or not these gravity wave results include tidal effects. By normalizing the densities to unity at 45 km, we attempted to minimize the contribution of tidal components and long-period gravity waves. In addition, the dominant period was found to be near 6 hours. Little is known experimentally or theoretically about tides with this period.
- These results show that wave potential energy per unit mass grow adiabatically and give up energy to the background atmosphere at various altitude regions. For instance below 55 to 65 km and above 75 to 80 km energy grow approximately at the adiabatic rates. In the intervening region, step function decreases in gravity

wave potential energy imply that the AGWs give up considerable energy to the background atmosphere in this region.

- The uniqueness of the ALO data set in terms of extended altitude range and extensive coverage in time limits the possibility of comparing our results to those obtained by others. Although some similar gravity wave work has been done in the past using Rayleigh lidar, it has been done in the upper stratosphere and lower mesosphere. In many cases they did not have enough observations to determine average behavior or find seasonal trends. Some similar work has been done using Na lidars, but they observe the region between 83 and 102 km, which begins at approximately where we have shown that the gravity wave behavior changes significantly. Furthermore, they do not have long term observations with which to determine seasonal trends.

These results show the importance of having good AGW observations throughout the mesosphere. Hopefully these studies can lead to future ones involving better height and time resolution, and studies that cover an even greater altitude range.

2. Future Work

Next, we could search for AGWs in other parts of the gravity wave spectrum. Based on 3-km altitude averages and 1-hour time averages in the present study, we can only detect gravity waves with vertical wavelengths more than 6 km and periods longer than 2 hours. While found 12 –16 km the most frequent vertical wavelengths, it has been suggested in the literature, using other types of observations, that there may be another peak in the gravity wave spectrum at shorter vertical wavelengths and, possibly, with shorter periods. We could reanalyze the ALO data with shorter altitude and time

averaging to look for this peak. If it exists we could examine this portion of the AGW spectrum for its characteristics and possibly for its sources. With shorter vertical wavelengths and periods, these gravity waves should relate to sources that are closer to the lidar, which might be able to identify.

Another study would be to examine how different parts of the AGW spectrum contribute to the wave field and lose their energy to the background atmosphere. For instance, what are the relative contributions of waves with 2–4 hour periods versus those with 8–10 hour periods. We have already started exploring the possibility of doing this. Examination of the density and temperature fluctuation profiles by using different integration times and vertical integrations is the approach to this. With the basic data having been obtained with 2-minute temporal and 37.5-m spatial resolution this is feasible.

Determining the background profile from the observed profiles is a very important step for calculating the perturbation profiles. There are many possible procedures that could be used for calculating the background density or temperature profiles. It might be significant to examine the effect of different background values, on the derived gravity wave parameters. For instance, our high-order fits and normalizing the densities to unity at 45 km might have minimized the ability to detect long wavelength gravity waves. We do not know. A starting point would be to reanalyze the data using temperature perturbations.

An easy extension of this work is to improve the statistics on monochromatic gravity waves by increasing the number of days from 150 to the whole 900-night data set. In the process, we might also find some unusual events on individual days.

While we do not believe tides are important to this analysis, it would be good to estimate their effect. One approach would be to use the lidar data to do so. Individual 1-hour profiles could be averaged for 11 to 31 nights over the 11 years to make composite nights from which we could derive the average tidal components. Those tidal components then could be removed from the data to perhaps obtain more accurate gravity wave components.

In addition to these possible major studies, other possibilities emerge from this work for smaller scale studies. One is that a few waves below 80 km were seen with upward phase velocities. An effort should be made to learn about the origin of these waves. Another is that considerable gravity wave potential energy was lost to the background atmosphere between 60 and 80 km. This leads to questions about the total energy given to the background atmosphere, how it compares to other energy sources, and what impact it has on the middle atmosphere.

We have already obtained considerable, very useful information from our mesospheric mid-latitude density and temperature observations. Even more could be learned with improved measurement capabilities. If we had simultaneous wind measurements throughout the middle atmosphere, we could directly examine dynamic instabilities and critical-layer filtering by the wind field, as well as examine the relationship between winds and temperature inversions. With such simultaneous observations of the wind, density and temperature fields, it would be easier to draw definite conclusions about gravity wave properties and their effects on the atmosphere.

More realistically, a much more sensitive Rayleigh lidar system combined with a resonance lidar system would play an important role in determining what happens to the

gravity waves near 80 km and what happens between 80 and 110 km. Such an enhanced Rayleigh lidar would also enable relative density and temperature measurements from 10 or 20 km to 110 km. This would help in identifying the cause of the factor of 20 changes in E_p from day to day. This would also help in obtaining measurements of AGWs all the way from the stratosphere through the mesopause, enabling the study of their propagation from the lower atmosphere to the middle atmosphere and into the low thermosphere.

REFERENCES

- Alexander, M. J., J. R. Holton, and D. R. Durran (1995), The gravity wave response above deep convection in a squall line simulation, *J. Atmos. Sci.*, 52, 2212-2226.
- Andrews, D. G., J. R. Holton, and C. B. Leovy (1987), *Middle Atmosphere Dynamics*, Academic Press, Orlando.
- Argall, P. S., and R. J. Sica (2007), A comparison of Rayleigh and sodium lidar temperature climatologies, *Ann. Geophys.*, 25, 27-35.
- Beissner, K. C. (1997), Studies of mid-latitude mesospheric temperature variability and its relationship to gravity waves, tides, and planetary waves, Ph.D. thesis, Utah State University, Logan, UT.
- Bevington, P. R., and D. K. Robinson (1969), *Data Reduction and Error Analysis for the Physical Sciences*, McGraw-Hill, New York.
- Brasseur, G., and S. Solomon (1984), *Aeronomy of the Middle Atmosphere*, Reidel, Dordrecht.
- Chanin, M. L. (1984), Review of lidar contributions to the description and understanding of the middle atmosphere, *J. Atmos. Terr. Phys.*, 46, 987-993.
- Chanin M. L., and A. Hauchecorne (1981), Lidar observation of gravity and tidal waves in the stratosphere and mesosphere, *J. Geophys. Res.*, 86, 9715-9721.
- Chanin, M. L., and A. Hauchecorne (1991), Lidar study of the structure and dynamics of the middle atmosphere, *Indian J. Radio and Space Phys.*, 20, 1-11.
- Charney, J. G., and P. G. Drazin (1961), Propagation of planetary-scale distribution from the lower into the upper atmosphere, *J. Geophys. Res.*, 66, 83-109.
- Collins, R. L., X. Tao, and C. S. Gardner (1996), Gravity wave activity in the upper mesosphere over Urbana, Illinois: Lidar observations and analysis of gravity wave propagation models, *J. Atmos. Terr. Phys.*, 58, 1905-1926.
- Eckermann, S. D., and R. A. Vincent (1989), Falling sphere observations of anisotropic gravity wave motions in the upper stratosphere over Australia, *Pure Appl. Geophys.*, 130, 509-532.
- Elterman, L. (1951), The measurement of stratospheric density distribution with the searchlight technique, *J. Geophys. Res.*, 56, 509-520.

- Fauliot, V., G. Thuillier, and F. Vial (1997), Mean vertical wind in the mesosphere-lower thermosphere region (80-120 km) deduced from the WINDII observations on board UARS, *Ann. Geophysicae*, *15*, 1221-1231.
- Fritts, D. C. (1984), Gravity wave saturation in the middle atmosphere: A review of theory and observations, *Rev. Geophys.*, *22*, 275-308.
- Fritts, D. C., and M. J. Alexander (2003), Gravity wave dynamics and effects in the middle atmosphere, *Rev. Geophys.*, *41*, 64, doi:10.1029/2001RG000106.
- Fritts, D. C., and G. D., Nastrom (1992), Sources of mesoscale variability of gravity waves. Part II: Frontal, convective, and Jet stream excitation, *J. Atmos. Sci.*, *49*, 111-127.
- Gao, X., J. W., Meriwether, V. B., Wickwar, T. D., Wilkerson, and S. Collins (1998), Rayleigh lidar measurements of the temporal frequency and vertical wavenumber spectra in the mesosphere over the Rocky Mountain region, *J. Geophys. Res.*, *103*, 6405-6416.
- Gardner, C. S. (1989), Sodium resonance fluorescence lidar applications in atmospheric science and astronomy, *Proc. IEEE*, *77*(3), 408-418.
- Gardner, C. S., and A. Z. Liu (2007), Seasonal variations of the vertical fluxes of heat and horizontal momentum in the mesopause region at Starfire optical range, New Mexico, *J. Geophys. Res.*, *112*, 17, D09113, doi:10.1029/2005JD006179.
- Gardner, C. S., M. S. Miller, and C. H. Liu (1989), Rayleigh lidar observations of gravity wave activity in the upper stratosphere at Urbana, Illinois, *J. Atmos. Sci.*, *46*, 1838-1854.
- Gardner, C. S., Y. Zhao, and A. Z. Liu (2002), Atmospheric stability and gravity wave dissipation in the mesopause region, *J. Atmos. Terr. Phys.*, *64*, 923-929.
- Gavrilov, N. M., and S. Fukao (2004), Numerical and the MU radar estimations of gravity wave enhancement and turbulent ozone fluxes near tropopause, *Ann. Geophys.*, *22*, 3889-3898.
- Geller, M. A. (1983), Dynamics of the middle atmosphere, *Space Science Reviews*, *34*, 359-375.
- Gille, S. T., A. Hauchecorne, and M. L. Chanin (1991), Semidiurnal and diurnal tidal effects in the middle atmosphere as seen by Rayleigh lidar, *J. Geophys. Res.*, *96*, 7579-7587.
- Hauchecorne, A., and M. L. Chanin (1980), Density and temperature profiles obtained by lidar between 35 and 70 km, *Geophys. Res. Lett.*, *7*, 565-568.

- Hauchecorne, A., and M. L. Chanin (1982), Mid-latitude ground-based lidar study of stratospheric warmings and planetary waves propagation, *J. Atmos. Terr. Phys.*, *44*, 577-583.
- Hauchecorne, A., and M. L. Chanin (1983), Mid-latitude observations of planetary waves in the middle atmosphere during the winter over 1981-1982, *J. Geophys. Res.*, *88*, 3843-3849.
- Hauchecorne, A., M. L. Chanin, and R. Wilson (1987), Mesospheric temperature inversion and gravity wave breaking, *Geophys. Res. Lett.*, *14*(9), 933-936.
- Hecht, J. (1992), *The Laser Guidebook*, McGraw-Hill, New York.
- Hedin, A. E. (1991), Extension of the MSIS thermospheric model into the middle and lower atmosphere, *J. Geophys. Res.*, *96*, 1159-1172.
- Herron, J. P. (2004), Mesospheric Temperature Climatology Above Utah State University, M.S. thesis, Utah State University, Logan.
- Herron, J. P. (2007), Rayleigh-scatter lidar observations at USU's atmospheric lidar observatory (Logan, UT)-Temperature climatology, temperature comparisons with MSIS, and noctilucent clouds, Ph.D. thesis, Utah State University, Logan, UT.
- Herron, J. P., and V. B. Wickwar (2009a), Mid-latitude mesospheric temperature climatology obtained with the Rayleigh-scatter lidar at USU's atmospheric lidar observatory (41.7° N, 111.8° W), Manuscript in preparation for *J. Geophys. Res.*
- Herron, J. P., and V. B. Wickwar (2009b), A comparison of mid-latitude mesospheric temperatures —the ALO lidar climatology and the NRL empirical model, Manuscript in preparation for *J. Geophys. Res.*
- Hines, C. O. (1960), Internal atmospheric gravity waves at ionospheric heights, *Canadian Journal of Physics*, *38*, 1441-1481.
- Hines, C. O. (1991), The saturation of gravity waves in the middle atmosphere. Part I: Critique of linear-instability theory, *J. Atmos. Sci.*, *48*, 1348-1359.
- Hines, C. O., and C. A. Reddy (1967), On the propagation of atmospheric gravity waves through regions of wind shear, *J. Geophys. Res.*, *72*, 1015-1034.
- Hirota, I. (1984), Climatology of gravity waves in the middle atmosphere, *J. Atmos. Terr. Phys.*, *46*, 767-773.

- Hirota, I., and T. Niki (1985), A statistical study of inertia-gravity waves in the middle atmosphere, *J. Meteorol. Soc. Japan*, *63*, 1055-1065.
- Hodges, R. R. (1967), Generation of turbulence in the upper atmosphere by internal gravity waves, *J. Geophys. Res.*, *72*, 3455.
- Holton, J. R. (1982), The role of gravity wave induced drag and diffusion in the momentum budget of the mesosphere, *J. Atmos. Sci.*, *39*, 791-799.
- Holton, J. R. (1983), The influence of gravity wave breaking on the general circulation of the middle atmosphere, *J. Atmos. Sci.*, *40*, 2497-2507.
- Holton, J. R. (1992), *An Introduction to Dynamic Meteorology*, Academic Press, San Diego.
- Holton, J. R., and M. J. Alexander (2000), The role of waves in the transport circulation of the middle atmosphere, *Geophysical Monograph 123*, 21-36, American Geophysical Union, Washington, D.C.
- Huang, K. M., S. D. Zhang, and F. Yi (2008), Propagation and reflection of gravity waves in a meridionally sheared wind flow, *J. Geophys. Res.*, *113*, D09106, doi:10.1029/2007JD008877.
- Johnson, E. A., R. C. Meyer, R. E. Hopkins and W. H. Mock (1939), The measurement of light scattered by the upper atmosphere from a search-light beam, *J.O.S.A.*, *29*, 512-517.
- Kent, G. S., and R. W. Wright (1970), A review of laser radar measurements of atmospheric properties, *J. Atmos. Terr. Phys.*, *32*, 917-943.
- Lane, T. P., R. D. Sharman (2006), Gravity wave breaking, secondary wave generation, and mixing above deep convection in a three-dimensional cloud model, *Geophys. Res. Lett.*, *33*, doi:10.1029/2006GL027988.
- Leblanc, T., I. S. McDermid, A. Hauchecorne, and P. Keckhut (1998), Evaluation of optimization of lidar temperature analysis algorithms using simulated data, *J. Geophys. Res.*, *103*, 6177-6187.
- Lindzen, R. S. (1968), Lower atmospheric energy sources for the upper atmosphere, *Meteorol. Monogr.*, *9*, 37-41.
- Lindzen, R. S. (1981), Turbulence and stress owing to gravity wave and tidal breakdown, *J. Geophys. Res.*, *86*, 9707-9714.

- Liu, A. Z., R. G. Roble, J. H. Hecht, M. F. Larsen, and C. S. Gardner (2004), Unstable layers in the mesopause region observed with Na lidar during the turbulent oxygen mixing experiment (TOMEX) campaign, *J. Geophys. Res.*, *109*, D02S02.
- Matsuno, T. (1982), A quasi one-dimensional model of the middle atmosphere circulation interacting with internal gravity waves, *J. Meteor. Soc. Japan*, *60*, 215-226.
- McDonald, A. J., L. Thomas, and D. P. Wareing (1998), Night-to-night changes in the characteristics of gravity waves at stratospheric and lower-mesospheric heights, *Ann. Geophysicae*, *16*, 229-237.
- McLandress, C. (1998), On the importance of gravity waves in the middle atmosphere and their parameterization in general circulation models, *J. Atmos. Sol. Terr. Phys.*, *60*, 1357-1383.
- Measures, R. M. (1992), *Laser Remote Sensing Fundamentals and Applications*, Kreiger, Malabar.
- Meriwether, J. W., P. D. Dao, R. T. McNutt, W. Klemetti, W. Moskowitz, and G. Davidson (1994), Rayleigh lidar observations of mesospheric temperature structure, *J. Geophys. Res.*, *99*, 16973-16987.
- Miller, M. S., C. S. Gardner and C. H. Liu (1987), Rayleigh lidar observations of gravity wave activity in the stratosphere and lower mesosphere. *EOSL Rep.* No. 87-008, University of Illinois, Urbana, IL, 62 pp.
- Mitchell, N. J., L. Thomas, and A. K. P. Marsh (1991), Lidar observations of long-period gravity waves in the stratosphere, *Ann. Geophysicae*, *9*, 588-596.
- Nastrom, G. D., and D. C. Fritts (1992), Sources of mesoscale variability of gravity waves. Part I: Topographic excitation, *J. Atmos. Sci.*, *49*, 101-110.
- Picone, J. M., A. E. Hedin, D. P. Drop, and A. C. Aikin (2002), NRLMSISE-00 empirical model of the atmosphere: Statistical comparisons and scientific issues, *J. Geophys. Res.*, *107*, A12, 1468, doi: 10.1029/2002JA009430.
- Rauthe, M., M. Gerding, J. Hoffner, and F.-J. Lübken (2006), Lidar temperature measurements of gravity waves over Kühlungsborn (54°N) from 1 to 105 km: A winter-summer comparison, *J. Geophys. Res.*, *111*, doi:10.1029/2006JD007354.
- Sechrist, Jr. C. F. (1981), Middle atmosphere program, *Handbook for MAP*, *1*, 44.
- She, C. Y., S. Chen, Z. Hu, J. Sherman, J. D. Vance, V. Vasoli, M. A. White, J. R. Yu, and D. A. Krueger (2000), Eight-year climatology of nocturnal temperature and sodium density in the mesopause region (80 to 105 km) over Fort Collins, CO (41°N, 105°W), *Geophys. Res. Lett.*, *27*, 3289-3292.

- She, C., and U. Von Zahn (1998), Concept of a two-level mesopause: Support through new lidar observations, *J. Geophys. Res.*, *103*, 5855-5863.
- Sherman, J. P., and C. Y. She (2006), Seasonal variation of mesopause region wind shears, convective and dynamic instabilities above Fort Collins, CO: A statistical study, *J. Atmos. Terr. Phys.*, *68*, 1061-1074.
- Shibata, T., T. Fukuda, and M. Maeda (1986), Density fluctuations in the middle atmosphere over Fukuoka observed by an XeF Rayleigh Lidar, *Geophys. Res. Lett.*, *13*, 1121-1124.
- Sica, R. J., and P. S. Argall (2007), Seasonal and nightly variations of gravity-wave energy density in the middle atmosphere measured by the Purple Crow lidar, *Ann. Geophys.*, *25*, 2139-2145.
- Sica, R. J., and M. D. Thorsely (1996), Measurements of superadiabatic lapse rates in the middle atmosphere. *Geophys. Res. Lett.*, *23*, 2797-2800.
- Synge, E. H. (1930), A method of investigating the higher atmosphere, *Phil. Mag.*, *9*, 1014-1020.
- Tsuda, T., Y. Murayama, H. Wiryosumarto, S. W. Harijono, and S. Kato (1994), Radiosonde observations of equatorial atmosphere dynamics over Indonesia, *J. Geophys. Res.*, *99*, 10507-10516.
- Tsuda, T., M. Nishida, C. Rocken, and R. Ware (2000), A global morphology of gravity wave activity in the stratosphere revealed by the GPS occultation data (GPS/MET), *J. Geophys. Res.*, *105*, 7257-7273.
- Vincent, R. A., and M. J. Alexander (2000), Gravity waves in the tropical lower stratosphere: An observational study of seasonal and interannual variability, *J. Geophys. Res.*, *105*, 17971-17982.
- Walterscheid, R. L., J. H. Hecht, R. A. Vincent, I. M. Reid, J. Woithe, and M. P. Hickey (1999), Analysis and interpretation of airglow and radar observations of quasi-monochromatic gravity waves in the upper mesosphere and lower thermosphere over Adelaide, Australia (35°S, 138°E), *J. Atmos. Terr. Phys.*, *61*, 461-478.
- Whiteway, J. A (1998), Enhanced and inhibited gravity wave spectra, *J. Atmos. Sci.*, *56*, 1344-1352.
- Whiteway, J.A., and A.I. Carswell (1994), Rayleigh lidar observations of thermal structure and gravity wave activity in the high Arctic during a stratospheric warming, *J. Atmos. Sci.*, *51*, 3122-3136.

- Whiteway, J. A., and A. I. Carswell (1995), Lidar observations of gravity wave activity in the upper stratosphere over Toronto, *J. Geophys. Res.*, *100* (D7), 14113-14124.
- Whiteway, J. A., A. I. Carswell, and W. E. Ward (1995), Mesospheric temperature inversions with overlying nearly adiabatic lapse rate: An indication of a well-mixed turbulent layer, *Geophys. Res. Lett.*, *22*(10), 1201-1204.
- Wickwar, V. B., T. D., Wilkerson, M., Hammond, and J. P., Herron (2001), Mesospheric temperature observations at the USU / CASS Atmospheric Lidar Observatory (ALO), Presented at Remote Sensing of the Atmosphere, Environment, and Space, edited by Singh, U. N., Itabe, T. and Sugimoto, N., *Proc. SPIE*, *4153*, 272-284.
- Wilson, R., A. Hauchecorne, and M. L. Chanin, (1990), Gravity wave spectra in the middle atmosphere as observed by Rayleigh lidar, *Geophys. Res. Lett.*, *17*, 1585-1588.
- Wilson, R., M. L. Chanin, and A. Hauchecorne, (1991a), Gravity waves in the middle atmosphere observed by Rayleigh lidar. 1. Case Studies, *J. Geophys. Res.*, *96*, 5153-5167.
- Wilson, R., M. L. Chanin, and A. Hauchecorne, (1991b), Gravity-waves in the middle atmosphere observed by Rayleigh lidar: 2. Climatology, *J. Geophys. Res.*, *96*, 5169-5183.
- Zhao, Y., A. Z. Liu, and C. S., Gardner (2003), Measurement of atmospheric stability in the mesopause region at Starfire optical range, New Mexico, *J. Atmos. Terr. Phys.*, *65*, 219-232.
- Zhou, X., J. R. Holton, and G. L. Mullendore (2002), Forcing of secondary waves by breaking of gravity waves in the mesosphere, *J. Geophys. Res.*, *107*, 4058.

APPENDICES

Appendix A

Derivation of Atmospheric Gravity Wave Dispersion Equation

The following derivation of the atmospheric gravity wave equations are based on the linear gravity wave theory first proposed by *Hines* [1960]. This theory treats the atmospheric gravity waves as small departures from a stably stratified background atmosphere varying only in the vertical direction. However, the starting point is the Navier-Stokes equation, which is the basis for all descriptions of the dynamics of the atmosphere describing the change in the flow speed \bar{u} of a small volume of fluid. Accelerations arising due to various forces give

$$\frac{d\bar{u}}{dt} = -\frac{1}{\rho}\nabla p + \bar{g} - 2\bar{\Omega} \times \bar{u} + \bar{f} + \bar{\xi} \quad (\text{A.1.1})$$

Holton [1992], where $-\frac{1}{\rho}\nabla p$ is the pressure gradient force, p is pressure, ρ is density, \bar{g} is the gravity force, which acts only in the vertical direction, $-2\bar{\Omega} \times \bar{u}$ is the coriolis force that plays a role for motions with a very large horizontal scale and which we neglect here because we consider smaller scales, $\bar{\Omega}$ is the Earth's angular velocity, \bar{f} and $\bar{\xi}$ are friction and drag forces, respectively, and both are neglected here because they are very small in most circumstances compared to the remaining terms.

The continuity, momentum and energy equations for a single component neutral gas then become

$$\frac{\partial \rho}{\partial t} + \nabla \cdot (\rho \bar{u}) = 0, \quad (\text{A.1.2})$$

$$\rho \left(\frac{\partial}{\partial t} + \bar{u} \cdot \nabla \right) \bar{u} + \nabla p - \rho \bar{g} = 0, \quad (\text{A.1.3})$$

$$\left(\frac{\partial}{\partial t} + \bar{u} \cdot \nabla \right) p + \gamma p (\nabla \cdot \bar{u}) = 0, \quad (\text{A.1.4})$$

where $\gamma = c_p/c_v$ is the ratio of specific heats at constant pressure c_p and constant volume c_v . Initially the atmosphere is assumed to have the properties,

Isothermal	$T_0 = \text{constant.}$	
Stationary	$u_0 = 0$	
Hydrostatic equilibrium	$\frac{\partial p}{\partial z} + n\langle m \rangle g = 0$	(A.1.5)
Mean molecular mass	$\langle m \rangle = \sum_i \frac{n_i m_i}{n}$, where i is index.	

Using these assumptions, equations (A.1.2), (A.1.3), and (A.1.4) become

$$\frac{\partial \rho_0}{\partial t} = 0, \quad (\text{A.1.6})$$

$$\nabla p_0 - \rho_0 g = 0, \quad (\text{A.1.7})$$

$$\frac{\partial p_0}{\partial t} = 0. \quad (\text{A.1.8})$$

From the above equations we see that the background atmosphere has constant density and pressure with time. Let's assume motion is only in the vertical direction, i.e., along the z direction, then

$$\nabla = \frac{\partial}{\partial z}, \quad (\text{A.1.9})$$

$$p_0 = n_0 k T_0, \quad (\text{A.1.10})$$

$$\rho_0 = n_0 m, \quad (\text{A.1.11})$$

$$g = -g, \quad (\text{A.1.12})$$

$$H_0 = \frac{kT_0}{mg}, \quad (\text{A.1.13})$$

where H_0 is the scale height for the background atmosphere.

From equations (A.1.5) and equations (A.1.6)-(A.1.13), we get

$$kT_0 \frac{dn_0}{dz} = -n_0 mg, \quad (\text{A.1.14})$$

which can be rewritten as follows and solved for n_0

$$\begin{aligned} \frac{1}{n_0} \frac{dn_0}{dz} &= -\frac{mg}{kT_0} = -\frac{1}{H_0}, \\ \int \frac{1}{n_0} dn_0 &= \int -\frac{1}{H_0} dz, \\ \ln(n_0) &= -\frac{z}{H_0}, \\ n_0 &= e^{-\frac{z}{H_0}}. \end{aligned} \quad (\text{A.1.15})$$

The density and pressure vary exponentially with altitude

$$p_0 = kT_0 e^{-\frac{z}{H_0}}, \quad (\text{A.1.16})$$

$$\rho_0 = m e^{-\frac{z}{H_0}}. \quad (\text{A.1.17})$$

Atmospheric perturbations are taken into account by adding a small value to the background values of velocity (u_0), density (ρ_0), temperature (T_0), and pressure (p_0)

$$\begin{aligned} \rho &= \rho_0 + \rho_1, \\ p &= p_0 + p_1, \\ \vec{u} &= \vec{u}_1 + \vec{u}_0, \end{aligned} \quad (\text{A.1.18})$$

where p_1, ρ_1 , and \bar{u}_1 are perturbed quantities of the wave, $\bar{u}_1 = u_{1x}\hat{x} + u_{1z}\hat{z}$, and $\bar{u}_0 = 0$.

Atmospheric gravity waves basically propagate in the horizontal direction, but they have a small vertical component. For simplicity, the propagation is assumed to be in the $x-z$ plane so that wave vector k has only x and z components. We also assume a horizontally stratified atmosphere and no background wind. Equations A.1.2-A.1.4 now become

$$\begin{aligned} \frac{\partial}{\partial t}(\rho_0 + \rho_1) + \nabla \cdot [(\rho_0 + \rho_1)\bar{u}_1] &= 0, \\ (\rho_0 + \rho_1) \left(\frac{\partial}{\partial t} + \bar{u}_1 \cdot \nabla \right) \bar{u}_1 + \nabla \cdot (p_0 + p_1) + (\rho_0 + \rho_1)\bar{g} &= 0, \quad (\text{A.1.19}) \\ \left(\frac{\partial}{\partial t} + \bar{u}_1 \cdot \nabla \right) (p_0 + p_1) + \gamma (p_0 + p_1) (\nabla \cdot \bar{u}_1) &= 0. \end{aligned}$$

Now we linearize the equations (A.1.19) as

$$\begin{aligned} \frac{\partial \rho_0}{\partial t} + \frac{\partial \rho_1}{\partial t} + \rho_0 \nabla \cdot \bar{u}_1 + \bar{u}_1 \nabla \cdot \rho_0 &= 0, \\ \rho_0 \frac{\partial \bar{u}_1}{\partial t} + \nabla \cdot \bar{p}_0 + \nabla \cdot \bar{p}_1 + \rho_0 \bar{g} + \rho_1 \bar{g} &= 0, \quad (\text{A.1.20}) \\ \frac{\partial p_0}{\partial t} + \frac{\partial p_1}{\partial t} + \bar{u}_1 \cdot \nabla p_0 + \gamma p_0 \nabla \cdot \bar{u}_1 &= 0. \end{aligned}$$

Apply the background properties,

$$\begin{aligned} \frac{\partial \rho_0}{\partial t} &= 0, \\ \nabla p_0 &= -\rho_0 g, \\ \frac{\partial p_0}{\partial t} &= 0, \\ \bar{u}_1 \cdot \nabla \rho_0 &= -\frac{\rho_0}{H_0} u_{1z}, \\ \bar{u}_1 \cdot \nabla p_0 &= -\frac{p_0}{H_0} u_{1z}, \end{aligned}$$

equations (A.1.20) now become

$$\begin{aligned}
 \frac{\partial \rho_1}{\partial t} + \rho_0 \nabla \cdot \bar{u}_1 - \frac{\rho_0}{H_0} u_{1z} &= 0, \\
 \rho_0 \frac{\partial u_1}{\partial t} - \rho_0 g + \nabla \cdot \bar{p}_1 + \rho_0 g - \rho_1 g &= 0, \\
 \frac{\partial p_1}{\partial t} - \frac{p_0}{H_0} u_{1z} + \gamma p_0 \nabla \cdot \bar{u}_1 &= 0.
 \end{aligned} \tag{A.1.21}$$

Equations (A.1.21) can be rewritten as

$$\begin{aligned}
 \frac{\partial}{\partial t} \frac{\rho_1}{\rho_0} + \nabla \cdot \bar{u}_1 - \frac{1}{H_0} u_{1z} &= 0, \\
 \frac{\partial u_1}{\partial t} + \frac{1}{\rho_0} \nabla \bar{p}_1 + \frac{\rho_1}{\rho_0} g &= 0, \\
 \frac{\partial}{\partial t} \frac{p_1}{p_0} - \frac{1}{H_0} u_{1z} + \gamma \nabla \cdot \bar{u}_1 &= 0.
 \end{aligned} \tag{A.1.22}$$

Taking the total derivative of the second term in equation (A.1.22)

$$\frac{1}{\rho_0} \nabla p_1 = \frac{1}{\rho_0} \left[\nabla p_1 \frac{p_0}{p_0} \right] = \frac{1}{\rho_0} \left[\nabla \left(\frac{p_1}{p_0} \right) (p_0) \right] = \frac{1}{\rho_0} \frac{p_1}{p_0} \nabla p_0 + \frac{1}{\rho_0} p_0 \nabla \frac{p_1}{p_0}, \tag{A.1.23}$$

we can rewrite the momentum equation in (A.1.22) as

$$\begin{aligned}
 \frac{\partial}{\partial t} \frac{\rho_1}{\rho_0} + \nabla \cdot \bar{u}_1 - \frac{1}{H_0} u_{1z} &= 0, \\
 \frac{\partial u_1}{\partial t} + \frac{1}{\rho_0} \frac{p_1}{p_0} \nabla p_0 + \frac{1}{\rho_0} p_0 \nabla \frac{p_1}{p_0} - \frac{\rho_1}{\rho_0} g &= 0, \\
 \frac{\partial}{\partial t} \frac{p_1}{p_0} - \frac{1}{H_0} u_{1z} + \gamma \nabla \cdot \bar{u}_1 &= 0.
 \end{aligned} \tag{A.1.24}$$

Now let's assume the following plane wave solution for equations (A.1.24)

$$\left(\frac{\rho_1}{\rho_0} \right), \left(\frac{p_1}{p_0} \right), u_1 \propto e^{i(k \cdot r - \omega t)}, \tag{A.1.25}$$

and take

$$\begin{aligned}\frac{\partial}{\partial t} &\rightarrow -i\omega \\ \nabla &\rightarrow ik_x + ik_z.\end{aligned}$$

Where we have wave propagation both in the horizontal and vertical directions, these give

$$\begin{aligned}-i\omega\left(\frac{\rho_1}{\rho_0}\right) + (ik_x + ik_z) \cdot (u_{1x} + u_{1z}) - \frac{1}{H_0} u_{1z} &= 0, \\ -i\omega(u_{1x} + u_{1z}) + \frac{1}{\rho_0} \frac{p_1}{p_0} \nabla p_0 + \frac{1}{\rho_0} p_0 (ik_x + ik_z) \cdot \frac{p_1}{p_0} + \frac{\rho_1}{\rho_0} g &= 0, \\ -i\omega \frac{p_1}{p_0} - \frac{1}{H_0} u_{1z} + \gamma (ik_x + ik_z) \cdot (u_{1x} + u_{1z}) &= 0.\end{aligned}\tag{A.1.26}$$

We can rewrite a term from equation (A.1.26) as

$$\frac{1}{\rho_0} \frac{p_1}{p_0} \nabla p_0 = -\frac{p_1}{p_0} \frac{c_0^2}{\gamma H_0},$$

where $c_0 = \sqrt{\gamma g H_0}$ is the sound speed in the neutral gas. With propagation in the $x-z$ plane, the momentum equation (A.1.26) becomes two equations, one for the u_{1x} component and one for the u_{1z} component. Therefore, equation (A.1.26) becomes four equations for four unknown perturbations $(\frac{\rho_1}{\rho_0}, \frac{p_1}{p_0}, u_{1x}, u_{1z})$,

$$\begin{aligned}-i\omega\left(\frac{\rho_1}{\rho_0}\right) + ik_x u_{1x} + ik_z u_{1z} - \frac{1}{H_0} u_{1z} &= 0, \\ -i\omega u_{1x} + \frac{1}{\rho_0} p_0 ik_x \left(\frac{p_1}{p_0}\right) &= 0, \\ -i\omega u_{1z} - \frac{p_1}{p_0} \frac{c_0^2}{\gamma H_0} + \frac{1}{\rho_0} p_0 ik_z \left(\frac{p_1}{p_0}\right) + \left(\frac{\rho_1}{\rho_0}\right) g &= 0, \\ -i\omega\left(\frac{p_1}{p_0}\right) - \frac{1}{H_0} u_{1z} + \gamma ik_z u_{1z} + \gamma ik_x u_{1x} &= 0.\end{aligned}\tag{A.1.27}$$

Substituting $\frac{p_0}{\rho_0} = \frac{c_0^2}{\gamma}$ into equations (A.1.27), we obtain

$$\begin{aligned}
 -i\omega \left(\frac{\rho_1}{\rho_0} \right) + ik_x u_{1x} + \left(ik_z - \frac{1}{H_0} \right) u_{1z} &= 0, \\
 -i\omega u_{1x} + \left(\frac{p_1}{p_0} \right) ik_x \frac{c_0^2}{\gamma} &= 0, \\
 -i\omega u_{1z} + \left(\frac{p_1}{p_0} \right) \left(ik_z \frac{c_0^2}{\gamma} - \frac{c_0^2}{\gamma H_0} \right) + \left(\frac{\rho_1}{\rho_0} \right) g &= 0, \\
 -i\omega \left(\frac{p_1}{p_0} \right) - \frac{1}{H_0} u_{1z} + \gamma ik_z u_{1z} + \gamma ik_x u_{1x} &= 0.
 \end{aligned} \tag{A.1.28}$$

The matrix form of the equation (A.1.28) is

$$\begin{bmatrix}
 -i\omega & 0 & ik_x & (ik_z - 1/H_0) \\
 0 & ik_x \frac{c_0^2}{\gamma} & -i\omega & 0 \\
 g & (ik_z - 1/H_0) \frac{c_0^2}{\gamma} & 0 & -i\omega \\
 0 & -i\omega & i\gamma k_x & (i\gamma k_z - 1/H_0)
 \end{bmatrix}
 \begin{bmatrix}
 \frac{\rho_1}{\rho_0} \\
 \frac{p_1}{p_0} \\
 u_{1x} \\
 u_{1z}
 \end{bmatrix} = 0. \tag{A.1.29}$$

The solution of the equation (A.1.29) is

$$\omega^4 - \omega^2 c_0^2 (k_x^2 + k_z^2) + (\gamma - 1) g^2 k_x^2 - i\gamma g \omega^2 k_x^2 = 0. \tag{A.1.30}$$

Atmospheric gravity waves have growth in the vertical direction along with propagation, so we allow k_z to have a real component k_{zr} and an imaginary component k_{zi} , i.e.,

$k_z = k_{zr} + ik_{zi}$. Then

$$\omega^4 - \omega^2 c_0^2 (k_x^2 + k_{zr}^2 + k_{zi}^2) + \gamma g k_{zi} \omega^2 + (\gamma - 1) g^2 k_x^2 - i\omega^2 k_{zr} (\gamma g + 2c_0^2 k_{zi}) = 0. \tag{A.1.31}$$

By using $c_0^2 = H_0 \gamma g$, from the imaginary part we get

$$k_{zi} = -\frac{\gamma g}{2c_0^2} = -\frac{1}{2H_0}. \quad (\text{A.1.32})$$

With both components of k_z , the velocity perturbation amplitude becomes

$$u_1 = e^{\frac{z}{2H_0}} e^{i(k_x x + k_z z - \omega t)}. \quad (\text{A.1.33})$$

Waves that propagate in this manner are called internal gravity waves. These waves grow in amplitude as the wave propagates higher in altitude. The x and z components of the waves are

$$u_{1x} = e^{\frac{z}{2H_0}} e^{i(k_x x - \omega t)}, \quad (\text{A.1.34})$$

$$u_{1z} = e^{\frac{z}{2H_0}} e^{i(k_z z - \omega t)}. \quad (\text{A.1.35})$$

As we see, equation (A.1.31) supports both acoustic (sound) and gravity waves. By letting the sound speed $c_0 \rightarrow \infty$ the dispersion equation (A.1.31) simplifies to

$$\omega^2 = \frac{N^2 (k_x^2)}{(k_x^2 + k_z^2) + \frac{1}{4H_0^2}}, \quad (\text{A.1.36})$$

$$k_z^2 = \frac{k_x^2 (N^2 - \omega^2)}{\omega^2} - \frac{1}{4H_0^2}, \quad (\text{A.1.37})$$

where, N is the Brunt-Väisälä frequency and its value squared is

$$N^2 = (\gamma - 1) \frac{g}{\gamma H_0}. \quad (\text{A.1.38})$$

This N^2 value in equation (A.1.38) is based on the assumption of an isothermal atmosphere. However, the N^2 values we derived in Chapter 4 and elsewhere in this

dissertation is based on the assumption of an adiabatic atmosphere, which adds an additional term to equation (A.1.38) associated with the variation of temperature with altitude to give the result equivalent to equation (4.1.2). We also suggest the reader see *Hines* [1974] on page 282 for more detail.

The above derivations are based on the assumption that there is no background wind in the atmosphere and hence no intrinsic quantities to be taken into account.

If we consider the effect of background wind \bar{u}_0 on wave propagation then the wave frequency would be affected by the wind and the frequency would be measured relative to the mean wind, which is called the intrinsic frequency $\hat{\omega}$, i.e., the frequency of a wave measured by an observer drifting with the fluid at speed \bar{u}_0 . The intrinsic frequency, i.e., the frequency that would be observed in a frame of reference moving with the background wind \bar{u}_0 is $\hat{\omega} = \omega - u_0 \bar{k}$, where $\bar{k} = (k_x, k_z)$ and $k_x = 2\pi/\lambda_x$ and $k_z = 2\pi/\lambda_z$.

With this consideration, equations (A.1.36) and (A.1.37) now become

$$\hat{\omega}^2 = \frac{N^2(k_x^2)}{(k_x^2 + k_z^2) + \frac{1}{4H_0^2}}, \quad (\text{A.1.39})$$

$$k_z^2 = \frac{k_x^2(N^2 - \hat{\omega}^2)}{\hat{\omega}^2} - \frac{1}{4H_0^2}. \quad (\text{A.1.40})$$

For gravity waves with midrange frequencies (i.e., $N \square \hat{\omega} \square f$, where $f = 9.5 \times 10^{-5}$ radian/s is the inertial frequency at ALO), for which $k_z^2 \square 1/4H_0^2$, the dispersion relation (A.1.40) further simplifies to

$$\hat{\omega} = N \frac{k_x}{k_z}, \quad (\text{A.1.41})$$

and the vertical wave number is related to the observed horizontal phase velocity, c_x , and the buoyancy frequency,

$$k_z = \frac{N}{c_x}, \quad (\text{A.1.42})$$

where

$$c_x = \hat{c}_x + u_0, \quad (\text{A.1.43})$$

and \hat{c}_x is the intrinsic horizontal phase velocity. By using equations (A.1.41) and (A.1.42), respectively, we can derive the equations for horizontal phase velocity and horizontal wavelength as

$$c_x - u_0 = \frac{N}{k_z} = \frac{\lambda_z}{\tau_b}. \quad (\text{A.1.44})$$

When we make the approximation, $c_x = \hat{c}_x$, i.e., neglecting the background wind,

$$c_x = \frac{N}{k_z} = \frac{\lambda_z}{\tau_b}, \quad (\text{A.1.45})$$

$$\lambda_x = \frac{\tau}{\tau_b} \lambda_z, \quad (\text{A.1.46})$$

where, $\tau = \lambda_z / c_z$ and τ_b are the observed wave and buoyancy periods, respectively.

The vertical wavelength λ_z and vertical phase velocity c_z are directly observed by examining the individual one-hour relative density perturbation profiles. The details of these observations are given in Chapter 5. Using the dispersion relations (A.1.36) and (A.1.37) for the atmospheric gravity waves we can also obtain the horizontal

distances X traveled by waves seen at altitude Z by the relation [*Walterscheid et al.*, 1999]

$$\frac{Z}{X} = \frac{v_g}{u_g} = -\frac{k_x}{k_z} \frac{k_z^2}{k_z^2 + \frac{1}{4H_0^2}}, \quad (\text{A.1.47})$$

where v_g and u_g are vertical and horizontal group velocities, respectively. (Note: $k_z < 0$ for waves with upward energy transfer, i.e., downward phase progression.) Furthermore, for upward propagating AGWs for which $k_z^2 \ll 1/4H_0^2$, equation (A.1.47) gives

$$X = \frac{\lambda_x}{\lambda_z} Z. \quad (\text{A.1.48})$$

Appendix B

IDL Programs

Program to calculate density fluctuation and potential energy

```

PRO Density fluctuation
Directory='D:\Rawdata\fil
PRINT, 'Please enter the data to analyze (example) 031218'
file="
READ, file
RESTORE, directory+file+'.sav'
NumberDens=(SIZE(Density))(1)
k=FLTARR(1201)
Es=FLTARR(1201)
zero=FLTARR(1201)
;N_SQ=FLTARR(1201)
Egrowth=FLTARR(1201)
E2=FLTARR(1201)
y=FLTARR(1201)
x=FLTARR(1201)
y2=FLTARR(1201)
w=fltarr(1201)
sigma=fltarr(1201)
DerivTh=FLTARR(1201)
yee=fltarr(1201)
gn=FLTARR(1201)
T=FLTARR(1202)
E11=FLTARR(1201)
E1=FLTARR(1201)
E3=FLTARR(1201)
E5=FLTARR(1201)
E6=FLTARR(1201)
yff=FLTARR(1201)
DeltaD=FLTARR(numberdens-1,1201)
DeltaD5=FLTARR(numberdens-1,1201)
w=FLTARR(1201)
newy=FLTARR(1201)
DeltaD00=FLTARR(NumberDens-1,1201)
DeltaDs00=FLTARR(1201)
E00=FLTARR(1201)
DeltaD1=FLTARR(Numberdens-1,1201)
DeltaD2=FLTARR(Numberdens-1,1201)
DeltaD66=FLTARR(Numberdens-1,1201)
DeltaDs66=FLTARR(1201)
DeltaDs6n=FLTARR(1201)
DeltaD3=FLTARR(NumberDens-1,1201)
DeltaD4=FLTARR(NumberDens-1,1201)
DeltaD6=FLTARR(NumberDens-1,1201)

```

```

DeltaD6pp=FLTARR(NumberDens-1,1201)
DeltaD0=FLTARR(NumberDens-1,1201)
DeltaDs=FLTARR(1201)
DeltaD6ps=FLTARR(1201)
DeltaDs1=FLTARR(1201)
E6d=FLTARR(1201)
DeltaDs2=FLTARR(1201)
DeltaDs3=FLTARR(1201)
Deltay=FLTARR(NumberDens-1,1201)
Deltays=FLTARR(1201)
DeltaDs4=FLTARR(1201)
DeltaDs5=FLTARR(1201)
DeltaDs6=FLTARR(1201)
DeltaDs0=FLTARR(1201)
E4=FLTARR(1201)
l=FLTARR(35)
m=FLTARR(1201)
y4=FLTARR(1201)
x=altprof(1160:2360)
Range1=FLTARR(1201)
y4=density[NumberDens-1,1160:2360]
y=ALOG(density[NumberDens-1,1160:2360])
y6=ALOG(density[NumberDens-1,1160:2360])
                                ;log of density profile of the last column
y1=ALOG(density[NumberDens-1,1160:2360])
Length = (SIZE(Data))(2)
Width  = (SIZE(Data))(1)
Twidth = (SIZE(RayleighTimes))(1)
Background = FLTARR(Width)
Background1 =FLTARR(Width,1001)
Background11 = FLTARR(Width)
CntError = FLTARR(TWidth,Length)
Signal = FLTARR(Width,Length)
PctError = FLTARR(TWidth,Length)
AvgSignal = FLTARR(TWidth,Length)
AvgRayleigh =FLTARR(TWidth,Length)
AvgBackground =FLTARR(Twidth)
Temp= FLTARR(Length)
sigdmns1=fltarr(Twidth,Length)
sigdmns2=fltarr(Twidth)
sigdmns3=fltarr(Twidth,Length)
sigdmns33=fltarr(Twidth,Length)
sigdmnsf1=fltarr(Twidth,Length)
sigdmnsf2=fltarr(Twidth,Length)
Range=FINDGEN(Length)*0.0375+0.0375/2.0

```

```

Range1=Range[1160:2360]
altres=0.0375
altprof=FindGen(Length)*0.0375+1.47+0.0375/2.0
avgbins = 81.0
add=0.0
Temp22 = 0.0
FOR i=0,Width-1 DO BEGIN
  Background(i) = TOTAL(DATA(i,BKLO:BKHI))/(BKHI-BKLO+1.0)
  Signal(i,*) = Data(i,*)-Background(i)
ENDFOR
FOR i=0,Twidth-1 DO BEGIN
  a = rayleightimes(i,0)
  b = rayleightimes(i,1)
  c = rayleightimes(i,2)
  temp(*) = 0.0
  temp22 = 0.0
  k = 0
  FOR l=a,b do begin
    if ((signal(l,1100) GE 60.0) AND (background(l) LT 20)) then begin
      temp(*) = temp(*)+data(l,*)
      temp22 = temp22+background(l)
      k = k+1.0
    endif
  ENDFOR
  Rayleightimes(i,2) = c
  AvgSignal(i,*) = Temp(*)/k
  AvgBackground(i) = temp22/k
  IF (i EQ (twidth-1)) Then begin
    AvgSignal(i,*) = AvgSignal(i,*)+add
    AvgBackground(i)= AvgBackground(i)+add
  ENDIF
  AvgSignal(i,1120:14004) =
SMOOTH(AvgSignal(i,1120:14004),Avgbins,/edge_truncate)
;cnterror is the variance
  Cnterror(i,*) = AvgSignal(i,*)/(Avgbins*k)+AvgBackground(i)/(k*(BKHI-
BKLO+1.0))
  AvgSignal(i,*) = AvgSignal(i,*)-AvgBackground(i)
  Pcterror(i,*) =(Cnterror[i,*)/(AvgSignal[i,]^2.0)
; sigdmns1[i,*) =((AvgSignal(i,*)/(Avgbins*k))/AvgSignal[i,]^2.0)
;; sigdmns2[i] =((AvgSignal(i,1160)/(Avgbins*k))/AvgSignal[i,1160]^2.0)
;; sigdmns3[i,*) =((1.0/AvgSignal[i,1160]^2.0)+(1.0/AvgSignal[i,]^2.0)-
((2.0/AvgSignal[i,1160])*(1.0/AvgSignal[i,]*)))*(AvgBackground(i)/(k*(BKHI-
BKLO+1.0)))
;
; sigdmnsf1[i,*) =(sigdmns1[i,*)+sigdmns2[i]+sigdmns3[i,*)
sigdmns1[i,*) =(Cnterror[i,*)/AvgSignal[i,]^2.0)

```

```

        sigdmns2[i]      =(Cnterror[i,1160]/AvgSignal[i,1160]^2.0)
        ;sigdmns2[i]      =(1.0/AvgSignal[i,1160])
        sigdmns33[i,*]
    =(1.0/AvgSignal[i,1160]^2.0)+(1.0/AvgSignal[i,*]^2.0))*(AvgBackground[i]/(k*(BKHI
    -BKLO+1.0)))^2.0
        sigdmns3[i,*]      =sigdmns33[i,*]-
    ((2.0/AvgSignal[i,1160])*(1.0/AvgSignal[i,*]))*(AvgBackground[i]/(k*(BKHI-
    BKLO+1.0)))^2.0
        sigdmnsf1[i,*]      =(sigdmns1[i,*]+sigdmns2[i]+sigdmns3[i,*])*(Density[i,*])^2.0
        sigdmnsf2[i,*]      =Pcterror[i,*]
;print,avgbackground[NumberDens-1]
    ENDFOR
    ;stop
    ;print,avgbackground[NumberDens-1]
    ;sigdmnsf=sigdmns1[NumberDens-1,1160:2360]+sigdmns2[NumberDens-
    1]+sigdmns3[NumberDens-1,1160:2360]
    ;cnerrd=sigdmnsf1[NumberDens-1,1160:2360]
    ;stopound
;sigdmns1=      (Cnterror[NumberDens-1,1160:2360]/AvgSignal[NumberDens-
    1,1160:2360]^2.0)
;sigdmns2=(Cnterror[NumberDens-1,1160]/AvgSignal[NumberDens-1,1160]^2.0)
;sigdmns3=((1.0/AvgSignal[NumberDens-1,1160]^2.0)+(1.0/AvgSignal[NumberDens-
    1,1160:2360]^2.0)-(2.0/AvgSignal[NumberDens-1,1160]*AvgSignal[NumberDens-
    1,1160:2360]))*(AvgBackground(NumberDens-1)/(1001.0))
;sigdmnsf=sigdmns1+sigdmns2+sigdmns3
    sigd=FLTARR(NumberDens-1,1201)
    sigds=FLTARR(1201)
    avgsigh=FLTARR(NumberDens-1,1201)
    avgsighs=FLTARR(1201)
    avgsig45=FLTARR(Numberdens-1)
    FOR i=0,NumberDens-2 DO BEGIN
        Avgsig45[i,*]=(AvgSignal[i,1160])
        Avgsigh[i,*]=(AvgSignal[i,1160:2360])^2.0
        sigd[i,*]=(sigdmnsf1[i,1160:2360])

    FOR j=0,1200 DO BEGIN
        Avgsig45s=TOTAL(Avgsig45[*],/NaN)/(NumberDens-2)
        Avgsighs[j]=TOTAL(Avgsigh[*],/NaN)/(NumberDens-2)
        sigds[j]=TOTAL(sigd[*],/NaN)/(NumberDens-2)
    ENDFOR
    ENDFOR

    AvgSighh=AvgSignal[NumberDens-1,1160:2360]
    AvgSighh45=AvgSignal[NumberDens-1,1160]
    ;dat=data[NumberDens-1,1160:2360]
    ;dat45=[Numberdens-1,1160]

```

```

; denegp1=((Range1^4.0)*((AvgSighs)))/(((Range1^4.0)*(AvgSighs)^2.0)
;denegp=Cnterror[NumberDens-1,1160:2360]
denegp=Cnterror[NumberDens-1,1160:2360]
denegp11=sigds
denegp451=((Range1[0]^4.0)*((AvgSig45s)))/(((Range1[0]^4.0)*(AvgSig45s)^2.0)
denegp45=Cnterror[NumberDens-1,1160]
denegp4511=sigds[0]
Dens451=((Range1[0]^2.0)*(AvgSig45s)
Dens45=((Range1[0]^2.0)*(AvgSighh45)
Densh1=((Range1[1]^2.0)*(AvgSighs)
Densh=((Range1[1]^2.0)*(AvgSighh)
aq=((Range1)^4.0)/(dens45)^2.0
aq1=((Range1)^4.0)/(dens451)^2.0
aqr=((aq)*(denegp))
aqr1=((aq1)*(denegp))
aqr45=((Range1[0]^4.0)*(denegp45)
aqr451=((Range1[0]^4.0)*(denegp45)
aqs=((AvgSighh^2.0)/(Dens45)^2.0)
aqs1=((AvgSighs)/(Dens451)^2.0)
;Cnerrd=((aqr)+((aq)*(aqs*aqr45))) ; variance of Normalized density at heighth.
yhr=AvgSignal[NumberDens-1,1160:2360]^2.0*range1[*]^4.0
y45r=AvgSignal[NumberDens-1,1160]^2.0*range1[0]^4.0
Cnerrd1=((aqr1)+((aq1)*(aqs1*aqr451))) ; variance of Normalized density at
height.
;Cnerrd1=((aqr)+((aq)*(aqs*aqr45)))
cnerrd=(sigdmnsf1[NumberDens-1,1160:2360]);*(Density[NumberDens-
1,1160:2360])^2.0;*(yhr/y45r)
;cnerrd=sigds/sqrt(NumberDens-1)
;cnerrd=((Pcterror[NumberDens-1,1160:2360])*(AvgSignal[NumberDens-
1,1160]^2.0))/(AvgSignal[NumberDens-1,1160:2360]^2.0*range1[*]^4.0)
at1=fltarr(1201)
at2=fltarr(1201)
aqrs=SQRT(Cnterror[NumberDens-1,1160:2360])
at1[0:1200]=(SMOOTH(Temperr[NumberDens-
1,1160:2360],81,/EDGE_TRUNCATE))^2.0at2[0:1200]=(SMOOTH(Temperr[NumberD
ens-1,1161:2361],81,/EDGE_TRUNCATE))^2.0
sigatt3=(at1+at2)/(altres*81)^2.0
sigmp=FLTARR(Twidth,1201)
sigmp1=FLTARR(width,1201)
Ranged=FLTARR(1201)
datass=FLTARR(Twidth,1201)
datass1=FLTARR(width,1201)
sigmpm=FLTARR(1201)
sigmpm1=FLTARR(1201)
norm=FLTARR(Twidth)
derivy=DERIV(y4,y)

```

```

    derivyf=DERIV(newy0,yf)
    dvd11=(cnterror[NumberDens-1,1160:2360]);/(AvgSignal[Numberdens-
1,1160:2094])
    DeltaDs666=fltarr(1201)
    DeltaD666=fltarr(Numberdens-1,1201)
    Deltad663=fltarr(Numberdens-1,1201)
    dvd=(pcterror[Numberdens-1,1160:2360])
    dvd1=FLTARR(Numberdens-1,1201)
    ;w1=SQRT(cnerrd1)/(SQRT(NumberDens-1))
    wwt=SQRT(cnerrd);/(SQRT(NumberDens-1))
    res=fltarr(1201)
    ffr=fltarr(4,1201)
;fit=POLYFITW(x,y,(1.0/cnerrd)/sqrt(3.2),3.0)
    fit2=POLY_FIT(x,yr,4);,MEASURE_ERRORS=wwt)
    fit=POLY_FIT(x,y,3,CHISQ=chi0,yfit=yfit1);,MEASURE_ERRORS=wwt)
    fit1=POLY_FIT(x,y,4,CHISQ=chi1,yfit=yuf);,MEASURE_ERRORS=wwt)
    fit4=POLY_FIT(x,y,6,CHISQ=chi1,yfit=yyyy);,MEASURE_ERRORS=wwt)
    fit66=POLY_FIT(x,y6,3,CHISQ=chi1,yfit=yyyy6)
    fit5=POLY_FIT(x,y,5,CHISQ=chi1,yfit=yyyy1);,MEASURE_ERRORS=wwt)
    fitt=POLY_FIT(x,Temperature[NumberDens-1,1160:2360],6,yfit=ft)
    newy=EXP(fit[0]+fit[1]*x+fit[2]*x^2.0+fit[3]*x^3.0)
    newy1=EXP(fit1[0]+fit1[1]*x+fit1[2]*x^2.0+fit1[3]*x^3.0+fit1[4]*x^4.0)
    newy2=EXP(fit2[0]+fit2[1]*x+fit2[2]*x^2.0+fit2[3]*x^3.0+fit2[4]*x^4.0)
    newy3=EXP(fit3[0]+fit3[1]*x+fit3[2]*x^2.0+fit3[3]*x^3.0)
    newy5=exp(yyyy)
    newy66=exp(yyyy6)
;newy5=yyyy+smooth(((y)-yyyy),81,/edge_truncate)
;newy5=EXP(newy5)
;newy5=EXP(yyyy+SMOOTH(ALOG(y4)-yyyy,160,/edge_truncate))
newy5=EXP(fit4[0]+fit4[1]*x+fit4[2]*x^2.0+fit4[3]*x^3.0+fit4[4]*x^4.0+fit4[5]*x^5.0
+fit4[6]*x^6.0)
;newy57=EXP(fit57[0]+fit57[1]*x+fit57[2]*x^2.0+fit57[3]*x^3.0)
    newy7=EXP(yyyy1)
;xnolz=0.0375*27
    cnerrd=cnerrd1/(newy5)^2.0
Dell=SMOOTH(ALOG(Density[0:NumberDens-2,1160:2360]),[1,81],/NaN)
for i=0,NumberDens-2 do begin
    fitn[i,*]=POLY_FIT(x,dell[i,*],6)
ENDFOR
newyfitn=FLTARR(NumberDens-1,1201)
FOR i=0,NumberDens-2 DO BEGIN
    newyfitn[i,*]=EXP(fitn[i,0]+fitn[i,1]*x+fitn[i,2]*x^2.0+fitn[i,3]*x^3.0+fitn[i,4]*x^4.0+f
itn[i,5]*x^5.0+fitn[i,6]*x^6.0)
ENDFOR
newyfitns=FLTARR(1201)
FOR j=0,1200 DO BEGIN

```

```

newyfitns[j]=(TOTAL(newyfitn[*],j)/NaN)/(NumberDens-1))
ENDFOR
Deltadfit6=FLTARR(NumberDens-1,1201)
Deltadfit61=FLTARR(NumberDens-1,1201)
Deltadfit6pp=FLTARR(NumberDens-1,1201)
Deltadfit6pp1=FLTARR(NumberDens-1,1201)
Deltadfit6s=FLTARR(1201)
Deltadfit6s1=FLTARR(1201)
FOR i=0,NumberDens-2 DO BEGIN
Deltadfit6pp[i,*]=((Density[i,1160:2360]-newyfitn[i,*])/(newyfitn[i,*]))
Deltadfit6[i,*]=((Density[i,1160:2360]-newyfitn[i,*])^2.0/(newyfitn[i,*]^2.0))
Deltadfit6pp1[i,*]=((Density[i,1160:2360]-newyfitns)/(newyfitns))
Deltadfit61[i,*]=((Density[i,1160:2360]-newyfitns)^2.0/(newyfitns)^2.0)
FOR j=0,1200 DO BEGIN
Deltadfit6s[j]=(TOTAL(Deltadfit6[*],j)/NaN)/(NumberDens-1))
Deltadfit6s1[j]=(TOTAL(Deltadfit61[*],j)/NaN)/(NumberDens-1))
ENDFOR
ENDFOR
WINDOW,26,xsize=300,ysize=250
plot,SMOOTH(((newy7-
newyfitns)/newyfitns)*100.0,15,/edge_truncate),x,yrange=[45,90],$
/xstyle,/ystyle,background=250,color=0,xrange=[-
4,4],thick=1.5,font=2,xticks=4,xminor=10,title='avgden-indvfit'
OPLOT,FLTARR(1200),x,linestyle=2,color=0
; image=TVRD(true=1)
; WRITE_PNG,'D:\indvslpert.png',image
WINDOW,18,xsize=300,ysize=250
plot,newyfitns,x,yrange=[45,90],/xstyle,/ystyle,background=250,color=0,thick=2,$
font=2,/xlog,xrange=[10^(-2.8),10^(0.2)],title='bkginddenfit'
kkh=FLTARR(2,Numberdens-1)
FOR i=0,(NumberDens-2) DO BEGIN
kkh[i,*]=LINFIT(AvgSignal[i,1160:2360],AvgSignal[NumberDens-1,1160:2360])
ENDFOR
densum=FLTARR(NumberDens-1,1201)
densums=FLTARR(1201)
;kkhh=transpose(kkh)
FOR i=0,NumberDens-2 DO BEGIN
densum[i,*]=kkh[1,i]*AvgSignal[i,1160:2360]
FOR j=0,1200 DO BEGIN
densums[j]=(TOTAL(densum[*],j)/NaN)/(NumberDens-1))
ENDFOR
ENDFOR
avgsgnl=POLY_FIT(x,ALOG(densums),6,yfit=y56)
fitsgnl=EXP(y56)
;WINDOW,30,xsize=300,ysize=200

```



```

;PLOT,x,AvgSignal[NumberDens-
1,1160:2360],xrange=[40,95],/xstyle,/ystyle,background=250,color=0,thick=4,font=2,$
;yrange=[-50,1400];,title='6thorderfit
;;OPLOT,x,densum[8,*],linestyle=0,color=3;,,thick=2
;OPLOT,x,AvgSignal[8,1160:2360],linestyle=0,color=3,thick=2
; image=TVRD(true=1)
; WRITE_PNG,'D:\photoncountwrl.png',image
;OPLOT,x,densum[8,*],linestyle=0,color=3;,,thick=2
;;OPLOT,x,AvgSignal[8,1160:2360],linestyle=0,color=3,thick=2
;STOP
WINDOW,31,xsize=300,ysize=250
PLOT,SMOOTH(((densums-
fitsgnl)/(fitsgnl))*100.0,15,/EDGE_TRUNCATE),x,yrange=[45,90],$
/xstyle,/ystyle,background=255,color=0,xrange=[-
4,4],font=2,thick=1.5,xticks=4,xminor=10
OPLOT,FLTARR(1201),x,linestyle=5,color=0
; image=TVRD(true=1)
; WRITE_PNG,'D:\indvdenfitavgwregress.png',image
;STOP
;perturb=Density[NumberDens-1,1160:2360]
;;perturb=(y1)
;nfft=FIX(ALOG(1201)/ALOG(2.))+1.0)
;nfft=2^nfft
;;IF(nfft LT 2048) THEN nfft=2048
;ffti=COMPLEXARR(nfft)
;nc1=FIX((nfft*37.5)/3000.0)
;nc2=nfft-nc1
;;if(nc1lt1)then goto,line727
;;FOR i=0,numberdens-2 DO BEGIN
;ffti(0:1200)=COMPLEX(perturb(0:1200))
;ffti=FFT(ffti,-1,/overwrite)
;ffti(nc1:nc2)=COMPLEX(0.0)
;ffti=FFT(ffti,+1,/overwrite)
;perturb(0:1200)=FLOAT(ffti(0:1200)); spatial lowpass filter
;;ENDFOR
;;stop
;perturb_ac=perturb
;;;FOR i=0,numberdens-2 DO BEGIN
;;prt_dc=TOTAL(perturb_ac(0:1200),/nan)/FLOAT(1201)
;;perturb_ac(0:1200)=perturb_ac(0:1200)-(prt_dc)
;;;ENDFOR
;stop
;Z1=EXP(Z)
;res1=EXP(Z)
;deltadnew=FLTARR(72,1201)
;deltadnews=FLTARR(1201)

```

```

Enew=FLTARR(1201)
step1=(NumberDens-139)
step=(numberdens-109)
;   for i=0,(step-1) Do begin
;;   Deltadnew[i,*]=((density[i,1160:2360]-newy5)/(newy5))^2.0
;;   for j=0,1200 do begin
;;   Deltadnews[j]=(TOTAL(DeltaDnew[*],j),/nan)/(step))
;;   endfor
;   endfor
;index33=fltarr(numberdens-1,1201)
;y51=fltarr(numberdens-1,1201)
;y50=density[0:numberDens-2,1160:2360]
;for i=0, numberdens-2 do begin
;if y50[i,*] lt 0.0 then REPLICATE_INPLACE,y50[i,*],0.0
;y51[i,*]=y50[i,1160:2360]
;endfor
;stop
    deltat=FLTARR(numberDens-1,1201)
    deltats=FLTARR(1201)
;   prtbs=smooth((alog(density[numberdens-1,1160:2360])-yyyy),162,/edge_truncate)
;yyyy1=(yyyy+prtbs)
;newy5=exp(yyyy1)
    DeltaDnew=FLTARR(Numberdens-1,1201)
    DeltaDnewpp=FLTARR(Numberdens-1,1201)
    DeltaDfit4pp=FLTARR(NumberDens-1,1201)
    DeltaDfitsplnpp=FLTARR(NumberDens-1,1201)
    DeltaDnews=FLTARR(1201)
    Deltadnightly=FLTARR(NumberDens-1,1201)
    FOR i=0,Numberdens-2 DO BEGIN
    DeltaDfitsplnpp[i,*]=((density[i,1160:2360]-newy6)/(newy6))-SQRT(cnerrdd)
    DeltaDnightly[i,*]=((density[i,1160:2360]-newy7)/(newy7))-SQRT(cnerrdd)
    DeltaDfit4pp[i,*]=((density[i,1160:2360]-newy1)/(newy1))-SQRT(cnerrdd)
    ENDFOR
    sigdmnsf2=FLTARR(NumberDens-1,1201)
    cnerrdd=FLTARR(1201)
    FOR i=0,Numberdens-2 DO BEGIN
    DeltaDnew[i,*]=((densum[i,*]-fitsgnl)/(fitsgnl))^2.0
    DeltaDnewpp[i,*]=(((SMOOTH(Densum[i,*],1,/edge_truncate)-fitsgnl)/(fitsgnl)))
    FOR j=0,1200 DO BEGIN
    DeltaDnews[j]=(TOTAL(DeltaDnew[*],j),/NaN)/(Numberdens-1))
    ENDFOR
    ENDFOR
    FOR i=0,Numberdens-2 DO BEGIN
    sigdmnsf2[i,*]=sigdmnsf1[i,1160:2360]
;   FOR j=0,1200 DO BEGIN
;   Cnerrdd[j]=(TOTAL(sigdmnsf2[*],j)/(y4)^2.0,/NaN)/(NumberDens-1))

```

```

;   ENDFOR
ENDFOR
FOR i=0,Numberdens-2 DO BEGIN
  DeltaD00[i,*]=((density[i,1160:2360]-y4)/(y4))^2.0;-cnerdd
  DeltaD0[i,*]=((density[i,1160:2360]-newy0)/(newy0))^2.0;-cnerdd
  DeltaD[i,*]=((density[i,1160:2360]-newy)/(newy))^2.0;-cnerdd
  DeltaD1[i,*]=((density[i,1160:2360]-newy1)/(newy1))^2.0;-cnerdd
  DeltaD2[i,*]=((density[i,1160:2360]-newy6)/newy6)^2
  DeltaD3[i,*]=((density[i,1160:2360]-newy7)/(newy7))^2.0;-cnerdd
  DeltaD4[i,*]=((density[i,1160:2360]-newy3)/(newy3))^2.0;-cnerdd
  DeltaD6[i,*]=((Density[i,1160:2360]-newy5)/newy5)^2.0;-(sigdmnsf1[i,1160:2360])
;DeltaD6[i,*]=ABS(DeltaD6[i,*]/(newy5)^2.0)
;   DeltaD6[i,*]=SMOOTH(((density[i,1160:2360]-newy5))^2.0,1,/edge_truncate)-
(sigdmnsf1[i,1160:2360])
;;   DeltaD6[i,*]=(DeltaD6[i,*]/(newy5)^2.0);-(sigdmnsf1[i,1160:2360]/(newy5)^2.0)
  DeltaD666[i,*]=(((Density[i,1160:2360])-newy5))^2.0;-cnerdd
  DeltaD6pp[i,*]=(((SMOOTH(Density[i,1160:2360],[1,1],/edge_truncate)-
newy5)/(newy5)));-SQRT(cnerdd))
;Deltat[i,*]=(Temperature[i,1160:2360]-Temperature[NumberDens-1,1160:2360])
;;   Deltat[i,*]=(Temperature[i,1160:2360]-ft)
;;   FOR i=0,Numberdens-2 DO BEGIN
;;   DeltaD6pp[i,*]=(((SMOOTH(Density[i,1160:2360],[1,5],/edge_truncate)-
newy66)/(newy66)))
;;   FOR j=0,1200 DO BEGIN
;;   DeltaD6ps[j]=(TOTAL(Deltad6pp[* ,j],/nan)/(Numberdens-1))
;;   ENDFOR
;;   ENDFOR
FOR j=0,1200 DO BEGIN
  DeltaDs00[j]=(TOTAL(DeltaD00[* ,j],/nan)/(Numberdens-1))
  DeltaDs0[j]=(TOTAL(DeltaD0[* ,j],/nan)/(Numberdens-1))
  DeltaDs[j]=(TOTAL(DeltaD[* ,j],/nan)/(Numberdens-1)) ; mean density fluctuation
;square for all columns.
  DeltaDs1[j]=(TOTAL(DeltaD1[* ,j],/nan)/(Numberdens-1))
  DeltaDs2[j]=(TOTAL(DeltaD2[* ,j],/nan)/(Numberdens-1))
  DeltaDs3[j]=(TOTAL(DeltaD3[* ,j],/nan)/(Numberdens-1))
  DeltaDs4[j]=(TOTAL(DeltaD4[* ,j],/nan)/(Numberdens-1))
;DeltaDs5[j]=(TOTAL(DeltaD5[* ,j],/nan)/(Numberdens-1))
  DeltaDs6[j]=(TOTAL(DeltaD6[* ,j],/nan)/(Numberdens-2));-cnerdd
  DeltaDs6n[j]=TOTAL(DeltaD6[* ,j],/nan)
  DeltaDs666[j]=(TOTAL(Deltad666[* ,j],/nan)/(Numberdens-1))
  DeltaD6ps[j]=(TOTAL(Deltad6pp[* ,j],/nan)/(Numberdens-1))
  Deltats[j]=(TOTAL(deltat[* ,j],/nan)/(NumberDens-1))
;cnerrdd[j]=(TOTAL(sigdmnsf2[* ,j]/(newy5)^2.0,/Nan)/(NumberDens-1))
  cnerrdd[j]=(TOTAL(sigdmnsf2[* ,j],/NaN)/(NumberDens-1))
ENDFOR
ENDFOR

```

```

tep1=FLTARR(NumberDens-1,1201)
tep11=FLTARR(1201)
Tep=Temperature[NumberDens-1,1160:2360]
FOR i=0,NumberDens-2 DO BEGIN
tep1[i,*]=(Temperr[i,*]/tep)^2.0
FOR j=0,1200 DO BEGIN
tep11[j]=(TOTAL(tep1[*],j)/NaN)/(NumberDens-1))
ENDFOR
ENDFOR
N_SQ=FLTARR(1201)
;gn=gh(1160:2360) ;new gravity values just up to the altitude
required.
Egrowth1=FLTARR(1201)
Deltadgrowth=FLTARR(1201)
N_SQ[*]=((gn/Temperature[NumberDens-1,1160:2360]))*(9.8+(DerivTh))/1000.0)
;N_SQ[*]=N_SQ
E00[*]=(0.5*((gn[*])^2/(N_SQ[*]))*((DeltaDs00[*])))
Es[*]=(0.5*((gn[*])^2/(N_SQ[*]))*((DeltaDs[*])))
E1[*]=(0.5*((gn[*])^2/(N_SQ[*]))*((DeltaDs1[*])))
E2[*]=(0.5*((gn[*])^2/(N_SQ[*]))*((DeltaDs2[*])))
E3[*]=(0.5*((gn[*])^2/(N_SQ[*]))*((DeltaDs3[*])))
E4[*]=(0.5*((gn[*])^2/(N_SQ[*]))*((DeltaDs4[*])))
E5[*]=(0.5*((gn[*])^2/(N_SQ[*]))*((DeltaDnews[*])))
E6[*]=(0.5*((gn[*])^2/(N_SQ[*]))*((DeltaDs6[*])))
E8[*]=(0.5*((gn[*])^2/(N_SQ[*]))*((Deltadfit6s)))
Enew[*]=(0.5*((gn[*])^2/(N_SQ[*]))*((DeltaDnews[*])))
;E8[*]=(0.5*((gn[*])^2/(N_SQ[*]))*((DeltaDs8[*])))
Egrowth[*]=100.0*EXP(((x[*]-
x[0])*28.9415*gn[*])/(8.314*(Temperature[NumberDens-1,1160:2360])))
;Egrowth1[*]=1.0*EXP(((x[*]-
x[0])*28.9415*gn[*])/(8.314*(Temperature[NumberDens-1,1160:2360])))
N=SQRT(N_SQ)
Deltadgrowth[*]=(1.0)*EXP(((x[*]-
x[0])*28.9415*gn[*])/(2.0*8.314*(Temperature[NumberDens-1,1160:2360])))
;Deltadgrowth=exp((x-x[0])/7.0)
Tb=((2.0*(DPI)/N)*(1.0/60.0))
dderv=FLTARR(NumberDens-1,1201)
Derivddd=FLTARR(Numberdens-1,1201)
deltad53=FLTARR(NumberDens-1,1201)
deltads53=FLTARR(1201)
Deltad663d=FLTARR(NumberDens-1,1201)
deltads66t=FLTARR(1201)
;Ddervs=FLTARR(1201)
Temcros=FLTARR(NumberDens-1,1201)
Temcrost=FLTARR(1201)
Dencros=FLTARR(NumberDens-1,1201)

```

```

Dencrost=FLTARR(1201)
ddevd=FLTARR(NumberDens-1,1201)
ddevds=FLTARR(1201)
sig22=SMOOTH(temperature[NumberDens- 1,1160:2360],81,/EDGE_TRUNCATE)
Derivthd=FLTARR(NumberDens-1,1201)
Nd=FLTARR(NumberDens-1,1201)
Nds=FLTARR(1201)
deltad668=FLTARR(numberdens-1,1201)
deltads668=FLTARR(1201)
;sig22=Temperature[NumberDens-1,1160:2360]
WINDOW,8,xsize=450,ysize=350
PLOT,(N_SQ[26:1200]*1e4),x[26:1200],yrange=[46,90],xrange=[0,12],/xstyle,/ystyle,$
background=255,color=0,thick=2.0,xticks=6,xminor=5,font=2
FOR i=0,NumberDens-2 DO BEGIN
DeltaD53[i,*]=((Density[i,1160:2360]-newy5)/(newy5))^2.0
DeltaD663[i,*]=(Density[i,1160:2360]);+(newy5)^2.0/(newy5)^2.0
Deltad668[i,*]=Density[i,1160:2360]/newy5
;DeltaD663d[i,*]=(Density[i,1160:2360]-newy5)
ddevd[i,*]=(DERIV(AvgSignal[i,1160:2360],E6))^2.0
dderv[i,*]=(DERIV(x[0:1200],SMOOTH(Temperature[i,1160:2360],41,/EDGE_TRU
NCATE)))- (DerivTh))^2.0
FOR j=0,1200 DO BEGIN
Temcros[j]=TOTAL(Temcros[* ,j],/NaN)/(NumberDens-1)
Dencros[j]=TOTAL(Dencros[* ,j],/NaN)
deltaDs53[j]=TOTAL(DeltaD53[* ,j],/NaN)/(NumberDens-1)
Deltads66[j]=TOTAL(Deltad663[* ,j],/NaN)/(NumberDens-1)
deltads668[j]=TOTAL(Deltad668[* ,i],/nan)/(NumberDens-1)
;Deltads66t[j]=TOTAL(Deltad663[* ,j],/NaN)
;Ddervs[j]=TOTAL(dderv[* ,j],/NaN)/(NumberDens-1)
ddevds[j]=TOTAL(ddevd[* ,j],/NaN)/(NumberDens-1)
;Nds[j]=TOTAL(Nd[* ,j],/NaN)
ENDFOR
ENDFOR
FOR i=0,NumberDens-2 DO BEGIN
ND[i,*]=(((gn/Temperature[i,1160:2360])*((dderv[i,*]+9.8)/1000.0))-N_SQ)^2.0
FOR j=0,1200 DO BEGIN
NDs[j]=TOTAL(ND[* ,j],/NaN)/(NumberDens-1)
ENDFOR
ENDFOR
da1=temperr(Numberdens-1,1080:2280)
da2=temperr(Numberdens-1,1160:2360)
;ad=((gn*gn)/(N_SQ))*((DeltaDs66)/(newy5)^2.0)
ad=((gn*gn)/(N_SQ))^2.0*(DeltaDs6);*(1.0/newy5)
;ac=((gn*gn)/(N_SQ))*(1.0/(newy5))
;add2=(SQRT(Cnerrd1)/(SQRT(NumberDens-1)))^2.0
;cnerrd=Pcterror[NumberDens-1,1160:2360]

```

```
;add1=(cnerrdd)/SQRT(NumberDens)
  add1=(cnerrd);/SQRT(NumberDens-1)
;add=((ad)-(ac))^2.0
add=(ad)
DePe=((add)*(add1)); Measurement Error in energy
STOP
END
; END OF PROGRAM
```

Appendix C
List of 150 Nights

List of 150 nights used for this analysis. The dates are in month/day/year format.

Date	Date	Date	Date
1/1/1995	4/8/2003	7/26/1996	10/14/1995
1/3/1995	4/9/2003	7/29/2002	10/14/1998
1/4/1995	4/10/2003	8/8/2001	10/14/1999
1/6/1997	4/11/2003	8/10/1994	10/15/1999
1/8/2003	4/12/2003	8/13/1995	10/18/1999
1/12/1995	4/26/2004	8/15/1994	10/19/1998
1/14/1997	4/27/2004	8/16/1995	10/19/1999
1/20/1995	5/2/2002	8/16/1996	10/20/1998
1/22/1995	5/9/2002	8/17/1995	10/20/2000
1/23/1995	5/20/2003	8/20/1995	10/24/1998
2/9/1997	5/21/2003	8/23/1994	10/29/1994
2/10/1997	5/23/2003	8/23/1996	10/30/1994
2/15/1994	5/24/2003	8/26/1995	10/31/1994
2/17/2001	6/6/2003	8/27/1995	11/3/1999
2/19/1995	6/6/2002	8/28/1995	11/6/1996
2/21/2004	6/7/1995	8/30/1994	11/14/1999
2/21/2002	6/11/1995	8/30/1995	11/15/1993
2/22/1995	6/12/1995	8/30/1996	11/15/1999
2/23/1995	6/22/2000	9/6/1995	11/16/1998
2/26/1995	6/23/1998	9/12/1994	11/20/1998
2/28/1995	6/24/1995	9/15/2000	11/26/1996
2/28/2003	6/25/1998	9/18/1994	12/9/1999
3/1/1995	6/27/2003	9/18/1995	12/17/1996
3/1/1997	6/27/1998	9/23/1994	12/18/1993
3/9/1994	6/29/2003	9/23/1998	12/20/1993
3/9/1997	7/3/1998	9/25/2000	12/20/1994
3/10/1997	7/5/2003	9/25/1994	12/21/1994
3/18/1995	7/7/1995	9/26/1994	12/28/1994
3/20/1995	7/8/1995	10/1/1998	12/30/1999
3/25/2003	7/8/1998	10/4/1999	12/31/1999
3/27/1995	7/10/2003	10/5/2000	
3/28/1995	7/14/1998	10/8/1995	
3/29/1995	7/15/1995	10/8/1998	
3/29/1997	7/16/1995	10/9/1999	
3/30/1995	7/17/1995	10/10/1999	
3/31/1997	7/17/2001	10/11/1996	
4/1/1995	7/23/1996	10/11/1998	
4/4/1995	7/23/2001	10/11/1999	
4/7/1995	7/24/1996	10/13/1998	
4/7/1997	7/25/1996	10/13/1999	

CURRICULUM VITAE

Durga N. Kafle
34 Aggie Village Apt. B
Logan, UT 84341
Work: 435-797-3350
Cell: 435-760-9722
Email: d.n.kafle@aggiemail.usu.edu

EDUCATION:

PhD (Physics), 2009, Utah State University, USA
MS (Physics), 2004, Northern Illinois University, USA
MSc (Physics), 1997, Tribhuvan University, Nepal
BS (Physics), 1994, Tribhuvan University, Nepal

PROFESSIONAL EXPERIENCE:

Graduate Teaching Assistant, 2005-2009, Utah State University, USA
Graduate Teaching Assistant, 2002-2004, Northern Illinois University, USA
Graduate Research Assistant, 2003-2004, Northern Illinois University, USA
Graduate Research Assistant, 2003-2004, Argonne National Laboratory (ANL), USA
Lecturer, 1997-2002, Tribhuva University, Kathmandu, Nepal
Lecturer, 1998-2002, Xavier Academy, Kathmandu, Nepal
Lecturer, 1998-2002, Department of Physics, Bhanubhakta College, Kathmandu, Nepal
Research Scholar, 1995-1997, Tribhuvan University, Kathmandu, Nepal

HONORS, AWARDS:

1. Gene Adams Endowed Scholarship 2006, outstanding academic performance
2. Howard L. Blood Endowed Scholarship 2008, outstanding academic performance
3. Named to the school of Graduate Studies Honor Roll (Dean's List) spring 2005
4. Elected to the USU Chapter of Sigma Pi Sigma, 2007
5. School of Graduate Studies Dissertation Fellowship 2009–2010 academic year
6. AGU Student Travel Grant, 2009
7. Student Travel Grant, USU, 2006, 2007, and 2009

PUBLICATIONS:

Kafle, D.N. (1997), A Study of Visibility in Kathmandu Valley, M.S. Thesis, 95 pp, Tribhuvan University, Kathmandu, Nepal.

- Kafle, D.N., and B.K. Sapkota (1998), Particulate Mass loading in Kathmandu Valley, *Tribhuvan University Journal*, *XXI*, 13-27.
- Kafle, D.N. (2004), Mössbauer Study of the Eu(14)MnSb(11) and Yb(14)MnSb(11) Zintl Compounds, M.S. Thesis, 76 pp, Northern Illinois University, DeKalb, Illinois.
- Hermann, R., F. Grandjean, D.N. Kafle, D.E. Brown, C. Johnson, S. Kauzlarich, and G. Long (2007), Antimony-121 Mössbauer Spectral Study of the Eu(14)MnSb(11) and Yb(14)MnSb(11) Zintl Compounds, *Inorg Chem.* 2007 Nov 7 ;17985872.
- Kafle, D.N., and V.B. Wickwar (2009), Climatology of Mesospheric Brunt-Väisälä Frequencies derived from Rayleigh-scatter Lidar above Logan, Utah, *J. Geophys. Res.*, (to be submitted).
- Kafle, D.N., and V.B. Wickwar (2009), Characteristics of Large-Scale Gravity Waves in the Mesosphere Observed by Rayleigh-lidar at Logan, Utah, *J.Atmos.Sci.*, (to be submitted).
- Kafle, D.N., and V.B. Wickwar (2009), Seasonal Variation of Large-Scale Mesospheric Gravity Wave Potential Energy Observed by Rayleigh-lidar at Logan, Utah, *J.Atmos.Sci.*, (to be submitted).
- Kafle D.N., V.B. Wickwar (2009), Decreases in gravity wave potential energy with altitude above Logan, Utah, *J. Geophys. Res.*, (to be submitted).